UNIVERSITY OF CALIFORNIA SAN DIEGO

Photoacoustic Monitoring of Anticoagulant Therapy and Other Imaging Applications

A dissertation submitted in partial satisfaction of the
requirements for the degree Doctor of Philosophy

in

Nanoengineering

by

Junxin Wang

Committee in charge:

Professor Jesse V. Jokerst, Chair
Professor Yi Chen
Professor David J. Hall
Professor Robert L. Sah
Professor Liangfang Zhang

2019

The Dissertation of Junxin Wang is approved, and it is acceptable in quality and form for publication on microfilm and electronically:

_____

_____

_____

_____

_____

Chair

University of California San Diego

2019

TABLE OF CONTENTS

LIST OF SUPPLEMENTARY MATERIALS

LIST OF FIGURES

ACKNOWLEDGEMENTS

This PhD journey was full of challenges, but I was very fortunate to have a lot of guidance and assistance from my mentors and colleagues.

First, I must acknowledge my research mentor Professor Jesse V. Jokerst. He took a chance on me when I was completely new in his field of research interest. He taught me from scratch. I recall the days when Professor Jokerst taught me tail vein injection and cardiac puncture at 5:30 am. His dedication and passion for science have inspired me to keep learning and challenging myself. In addition to the scientific coaching, Professor Jokerst encouraged me to commercialize research products and allowed me to intern at a biotechnology venture, which was critical for my career development. I am grateful for his scientific, moral, and financial support throughout my PhD study.

My committee members, Professor Liangfang Zhang, Professor David Hall, Professor Robert L. Sah, and Professor Yi Chen, gave me very helpful directions for my research.

My labmates have given me tremendous help. I want to thank Dr. AnanthaKrishnan Soundaram Jeevarathinam for his chemistry education and constant encouragement. I would never be able to publish that many papers without his help. Anamik Jhunjhunwala, Santiago Arconada Alvarez, and James Hartanto were bright researchers and helped me tremendously during many experiments. Dr. Fang Chen, Jeanne E. Lemaster, Ali Hariri, and Colman Moore are creative scientists who generously helped me in many projects.

Special thanks to Professor Andrew M. Sarangan and Professor Jingquan Lin. They recruited me in their research projects way before I know how to be a good researcher. The effort that Professor Sarangan spent on me was more than what he should. I also want to thank Professors Joseph Haus, Partha Banerjee, Zuobin Wang, and Mei Kong for their generous helps in my graduate school applications. I would not have been able to attend a PhD program without their assistance.

Most importantly, I want to thank my dearest parents. Their constant encouragement and insightful suggestions are solid foundations for me to achieve any success in the PhD research. The essential rules for life I learned from them always inspired me to seek novel solutions to address difficult problems.

Finally, I want to make professional acknowledgements to my collaborators:

Chapter 2, in full, is a reprint of the material as it appears in *Nano Letters*, 2016, 16 (10), pp 6265–6271. Junxin Wang, Fang Chen, Santiago J Arconada-Alvarez, James Hartanto, Li-Peng Yap, Ryan Park, Fang Wang, Ivetta Vorobyova, Grant Dagliyan, Peter S Conti, Jesse V Jokerst. The dissertation author was the primary investigator and author of this paper.

Chapter 3, in full, is a reprint of the material as it appears in *Bioconjugate Chemistry*, 2018, 29 (11), 3768–3775. Junxin Wang, Ananthakrishnan Soundaram Jeevarathinam, Kathryn Humphries, Anamik Jhunjhunwala, Fang Chen, Ali Hariri, Bill R Miller III, Jesse V Jokerst. The dissertation author was the primary investigator and author of this paper.

Chapter 4, in partial, is a reprint of the material as it appears in *Biosensors and Bioelectronics*, 2019, 126, pp 831-837. Ananthakrishnan Soundaram Jeevarathinam, Navin Pai, Kevin Huang, Ali Hariri, Junxin Wang, Yuting Bai, Lu Wang, Tiffany Hancock, Stanley Keys, William Penny, Jesse V Jokerst. The dissertation author was the co-author of this paper.

Chapter 5, in full, is a reprint of the material as it appears in *Langmuir*, 2018, 34 (1), pp 359–365. Junxin Wang, Ching-Yu Lin, Colman Moore, Anamik Jhunjhunwala, Jesse V Jokerst. The dissertation author was the primary investigator and author of this paper.

Chapter 6, in full is currently being prepared for submission for publication of the material. Junxin Wang, Su-wen Hsu, Natalia Gonzalez-Pech, Anamik Jhunjhunwala, Fang Chen, Ali Hariri, Vicki Grassian, Andrea Tao, Jesse V. Jokerst. The dissertation author was the primary investigator and author of this paper.

VITA

2012	Bachelor of Science in Optical Information Science and Technology, Changchun University of Science and Technology
2014	Master of Science in Laser and Optical Engineering, University of Dayton
2015-2019	Research Assistant, University of California San Diego
2019	Ph.D. in Nanoengineering, University of California San Diego

ABSTRACT OF THE DISSERTATION

Photoacoustic Monitoring of Anticoagulant Therapy and Other Imaging Applications

by

Junxin Wang

Doctor of Philosophy in Nanoengineering

University of California San Diego, 2019

Professor Jesse V. Jokerst, Chair

Photoacoustic imaging uses nanosecond laser pulses to excite materials and generate acoustic waves. This “light in, sound out” technique can extend the applications of traditional ultrasound by harnessing the optical properties of materials. These features can be used for the non-invasive monitoring of drugs, molecular interaction, and diseases. In this dissertation, I will present three case studies that use photoacoustic imaging in tandem with nanoparticle contrast agents. The first case leverages photoacoustic imaging for heparin and clotting time monitoring via phenothiazine dyes embedded in nanomaterials. The heparin concentration and clotting time could be determined by the photoacoustic intensity of methylene blue increased by heparin, and this signal enhancement was due to the aggregation between the two molecules. To translate this technique for clinical use, we developed a cellulose sensor loaded with Nile blue A for finger-prick

diagnostics. Human studies using 78 blood samples revealed that the photoacoustic intensity of the sensor was strongly correlated to the activated clotting time (Pearson's r=0.86), which was the gold standard for clotting time measurement. In addition to direct measurements of therapeutic, the second study used photoacoustic imaging to monitor the micellization of sodium dodecyl sulfate (SDS). The micellization can be determined because the photoacoustic intensity of methylene blue shows 492-fold enhancement upon addition of 3.47 mM SDS due to fluorescent quenching, which is caused by the aggregation between methylene blue and SDS. Higher concentrations above the SDS critical micelle concentration at 8.67 mM decreases the intensity signal by 54-fold because of the disassociation of the aggregates. The final case evaluated copper sulfide (CuS) nanodisk and nanoprism as the photoacoustic contrast agents for ovarian tumor detection. We found that the nanodisks have 1.8-fold higher accumulation than nanoprisms in the ovarian tumors indicating the importance of nanoparticle shape for tumor penetration. Versus baseline, the tumors treated with nanodisk revealed three-fold stronger photoacoustic intensity with a characteristic intensity peak at 920 nm. These three photoacoustic applications could improve healthcare because photoacoustic imaging is faster and more cost-effective than most of the imaging modalities in medicine.

Chapter 1 Introduction of Photoacoustic Imaging

1.1 History and Principle

Some of the basic principles underlying photoacoustic imaging was first reported by Alexander Graham Bell in 1881 as part of his work on telephone when he discovered that modulated sunlight could generate sound or a "photophonic phenomena".[1] However, a true technical breakthrough did not occur until the invention of laser in 1960s, which was required for generating high power photoacoustic signal.[2] The mechanism of photoacoustics is thermal expansion: After absorbing laser energy, the materials can generate expansion and contraction due to local temperature rise and heat dissipation. The vibration induces high frequency waves that can be detected with an ultrasound transducer (**Figure 1.1**).

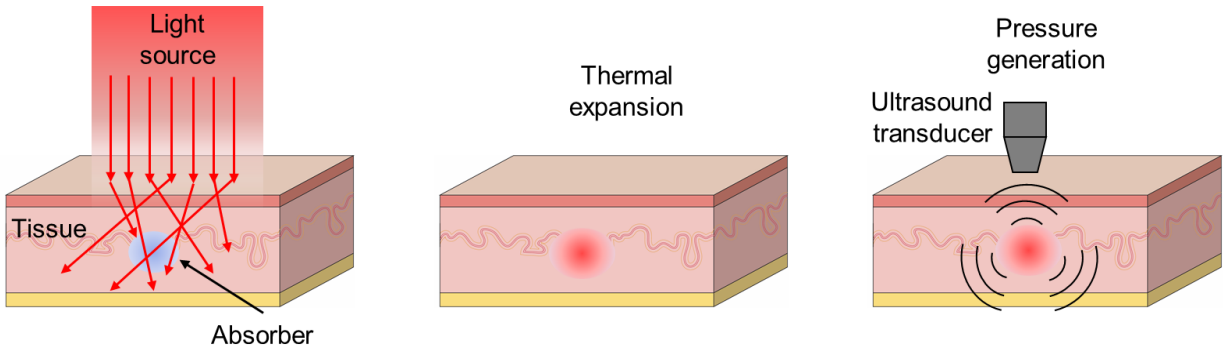

Figure 1. 1 Principle of thermal expansion. Light exposure (e.g. laser or LED) induces local temperature rise of the absorber. The expansion and contraction due to the increase and decrease of local temperature generates acoustic waves.

Photoacoustic imaging systems for biomedical applications often use a nanosecond laser because the small pulse duration enables thermal and stress confinement in biological tissues that enhance photoacoustic signal and simplifies image reconstruction.[3] The generated acoustic wave intensity (p_0) under laser excitation can be estimated as a function of laser fluence (F in J/cm^3), isobaric volume expansion coefficient (β in K^{-1}), absorption coefficient (μ_a in cm^{-1}), heat capacity (Cp in J/K kg), and the speed of sound (c in m/s) in the region; this can be described by the following equation[3, 4]:

$$p_0=(\beta c^2/C_p)\mu_a F \quad (1.1)$$

1.2 Photoacoustic Imaging Systems

After 60 years of development, a variety of photoacoustic imaging systems have been developed for diverse applications. The most common photoacoustic imaging systems are tomography, microscopy, and endoscopy. These imaging systems leverage the high spatial and temporal resolution from ultrasound as well as the high contrast of optics. For example, photoacoustic tomography[5, 6] can acquire a full body scan of a nude mouse with details of organs and vasculatures in 5 minutes (**Figure 1.2 A**).[7] Photoacoustic tomography can be used to stage breast cancer because breast cancers have a dysregulated vasculature with photoacoustic signal from hemoglobin.[8]

In addition to high contrast, photoacoustic imaging also offers low ultrasound scattering by tissue (3 orders of magnitude lower than optical scattering)[9] to achieve a lateral resolution of 220 nm, axial resolution of 15 μm, and a maximum imaging depth of 100 μm (**Figure 1.2 B**).[10] Photoacoustic microscopy can image red blood cells[11], cell nuclei[12], and retinal micro-vasculature[13]. Finally, photoacoustic imaging can employ an optical fiber as the light source and a miniaturized ultrasound sensor as the signal receiver for endoscopic applications. For example, photoacoustic transvaginal[14] and intravenous[15] imaging have been demonstrated to detect ovarian cancer[14] and identify lipid plaques in atheroma[16] (**Figure 1.2 C**), respectively.

Less common photoacoustic imaging systems include flow cytometry, Doppler flowmetry, and thermometry. Photoacoustic cytometry uses photoacoustic effect, rather than fluorescence, to sort and count the number of non-fluorescent biological materials such as circulating melanoma cells[17] and cells labeled with graphene[18] (**Figure 1.2 D**). Photoacoustic flowmetry relies on the frequency shift of the photoacoustic signal caused by moving subjects to measure their speed (**Figure 1.2 E**).[19] A potential clinical application of photoacoustic flowmetry is the monitoring of tissue metabolisms.[20] Finally, photoacoustic thermometry has been exploited to measure deep

tissue temperature with accuracy of ~0.6 C^0 because the photoacoustic and speed of sound is a function of temperature (**Figure 1.2 F**).[21]

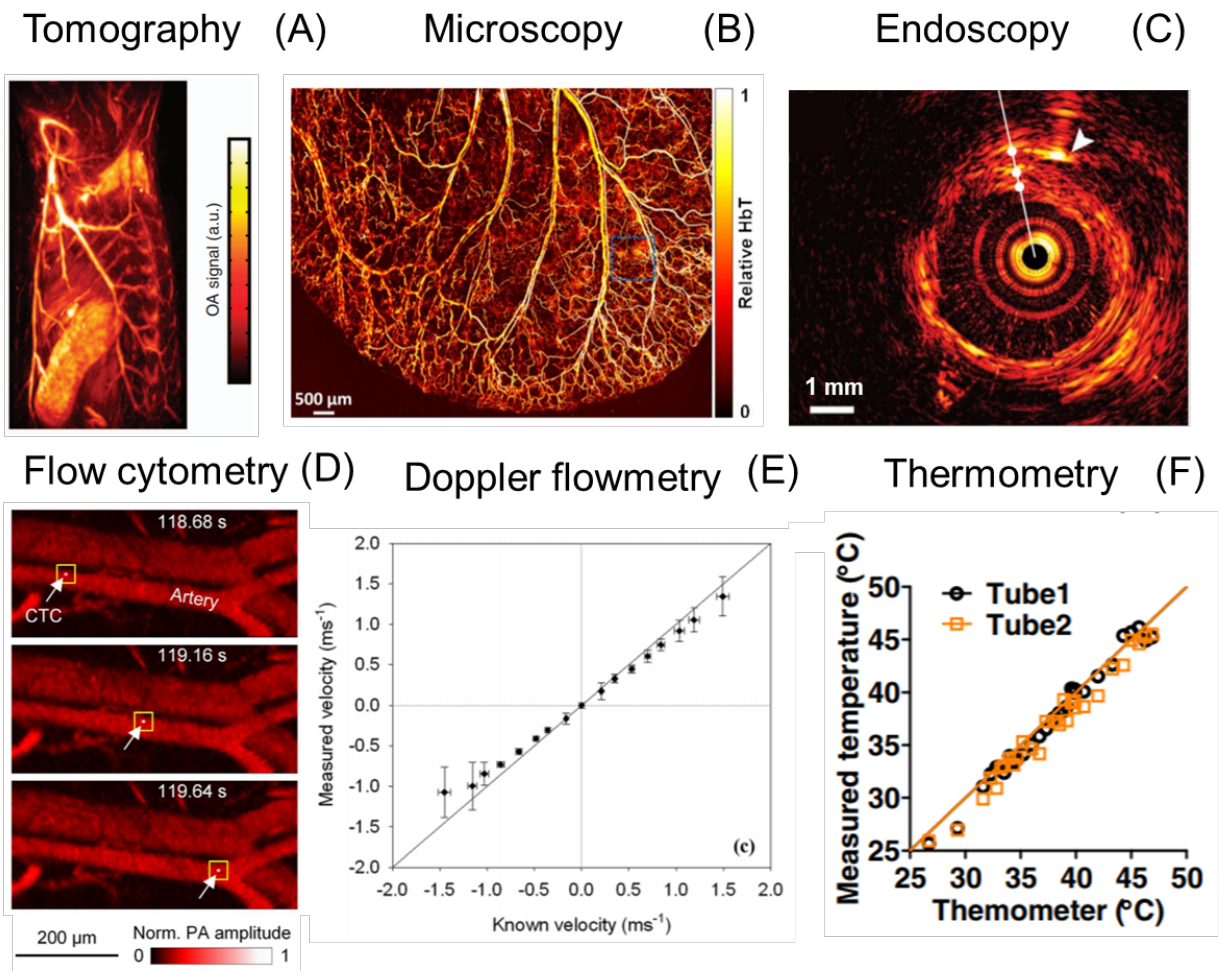

Figure 1. 2 Photoacoustic imaging system. Panel A is a tomographic photoacoustic image of a whole-body nude mouse. Reproduced courtesy of Springer Nature.[7] Panel B is a photoacoustic microscope image of mouse ear. Reprint with permission from OSA Publishing.[22] Scale bar is 500 μm. Panel C is an intravenous photoacoustic image of advanced human atherosclerosis at the excitation of 1210 nm (peak lipid absorption). The signal represent in red indicates the concentration of lipid. Reprint with permission from OSA Publishing.[23] Panel D shows the snapshots of a circulating tumor cell (CTC) at three different time points. Reproduced courtesy of Springer Nature.[24] Panel E shows that the velocity of a absorber measured by the photoacoustic Doppler flowmetry is close to the known values (difference < 3%). Reproduced with the permission of the Acoustical Society of America.[19] Panel F shows the strong linear correlation between the temperature of two samples measured by the photoacoustic thermometry and thermometer. Reprint with permission from OSA Publishing.[21]

1.3 Photoacoustic Contrast Agent

Photoacoustic imaging requires the absorbers to provide contrast that differentiates regions of interest from adjacent tissues based on their absorptions at different wavelengths. The

absorbers could be tissue chromophores, including hemoglobin, melanin, lipid, and elastin because of their high absorption at the first or second near-infrared window.[2] There are also exogeneous contrast agents that can be categorized as inorganic and organic contrast agents.

Common inorganic photoacoustic contrast agents are metallic nanoparticles and non-plasmonic carbon nanomaterials. Gold nanocrystals have been widely utilized exploited as a photoacoustic contrast agent because of its low toxicity[25], strong sensitivity with a detection limit of sub-nanomolar[26], and tunable localized surface plasmon resonance[27]. These tunable absorption bands ranging from 600 nm to 1200 nm are desirable for photoacoustic imaging because they can be used to selectively highlight different targets in the same regions of interest.[28] Other metallic nanomaterials such as transition-metal chalcogenides (e.g. tungsten disulfide[29] and copper sulfide[30]) have also been demonstrated as photoacoustic contrast agents. In addition to metallic materials, non-plasmonic carbon nanomaterials such as carbon nanotubes exhibit strong photoacoustic signal even though they lack absorption tunability.[30, 31] While these inorganic nanoparticles have stable and strong photoacoustic properties and biocompatibility, they also often have challenges being degraded and cleared from the body.[32]

In contrast, some organic contrast agents such as organic small molecules are biodegradable and strong photoacoustic absorbers. For example, methylene blue is a photoacoustic contrast agent for identifying lymph node in biopsy procedures.[33] It is also approved by the US Food and Drug Administration to treat methemoglobinemia[34] with a half-life of 5.25 hours in the human body[35]. Other photoacoustic small molecules include porphyrin, melanin, and perylenediimide.[32] These molecules have high absorption with fluorescent emissions that are often lower than fluorescent dyes. Therefore, the non-radiative heat increases the photoacoustic signal under laser excitation. While small molecules have strong photoacoustic signal in the first near infrared (NIR) window, there is also a growing interest in semiconducting polymer nanoparticles because they have superior absorptions at the second NIR window for deep tissue imaging.[36] For example, Yin *et al.* demonstrates a thiodiazoloquinoxaline-based semiconducting

polymer nanoparticles for stem cell imaging in brain under 1064 nm laser excitation. While the biodegradability of photoacoustic polymer nanoparticles remains as a concern, Lyu *et al.* revealed that introducing vinylene bond into the polymeric units could maintain the photoacoustic property and facilitate the fragmentation of polymers in biological environment with oxidative species.[37]

1.4 Summary

With the contrast agents, photoacoustics is a “color ultrasound”. It uses the spectral nature of optics to highlight the region of interest in ultrasound images. Additionally, photoacoustic imaging is more cost-effective than other imaging modalities such as computer tomography and has significant potential to complement conventional ultrasound.[8] These features motivated this work in photoacoustic imaging for novel diagnostic applications.

Here, I illustrate 3 novel photoacoustic contrast applications. The first application uses photoacoustic imaging to measure heparin concentration and clotting time in anticoagulant therapy with methylene blue and Nile Blue A. The second application exploits photoacoustic imaging to monitor the micellization of SDS. The last application employs copper sulfide (CuS) nanoparticles as the contrast agent for ovarian tumor imaging.

Chapter 2 A Nanoscale Tool for Photoacoustic-based Measurements of Clotting Time and Therapeutic Drug Monitoring of Heparin

Heparin anticoagulation therapy is an indispensable feature of clinical care yet has a narrow therapeutic window and is the second most common intensive care unit (ICU) medication error. The active partial thromboplastin time (aPTT) monitors heparin, but suffers from long turnaround times, a variable reference range, limited utility with low molecular weight heparin, and poor correlation to dose. Here, we describe a photoacoustic imaging technique to monitor heparin concentration using methylene blue as a simple and Federal Drug Administration-approved contrast agent. We found a strong correlation between heparin concentration and photoacoustic signal measured in phosphate buffered saline (PBS) and blood. Clinically relevant heparin concentrations were detected in blood in 32 seconds with a detection limit of 0.28 U/mL. We validated this imaging approach by correlation to the aPTT (Pearson's $r = 0.86$; $p<0.05$) as well as with protamine sulfate treatment. This technique also has good utility with low molecular weight heparin (enoxaparin) including a blood detection limit of 72 μg/mL. We then used these findings to create a nanoparticle-based hybrid material that can immobilize methylene blue for potential applications as a wearable/implantable heparin sensor to maintain drug levels in the therapeutic window. To the best of our knowledge, this is the first use of photoacoustics to image anticoagulation therapy with significant potential implications to the cardiovascular and surgical community.

2.1 Introduction

Heparin anticoagulation therapy is a cornerstone of surgical and cardiovascular medicine because of its short half-life, easy reversibility, and low cost.[38-40] It is used prophylactically in angiography (2 million cases/year),[41] coronary bypass (0.5 million cases/year),[42] cannulation,[43] and extracorporeal membrane oxygenation[44] as well as therapeutically for thromboses (300 thousand /year)[45] with over 500 million doses given annually worldwide.[46] This highly sulfated and negatively charged glycosaminoglycan increases the activity of anti-thrombin 1000-fold to inactivate the clotting factors thrombin and Factor Xa.[47]

However, heparin anticoagulation therapy is challenged by its variable molecular weight, activity, and biodistribution.[38] Heparin has a narrow therapeutic window and is the second most common ICU medication error.[48] These inherent challenges are compounded by iatrogenic errors such as incorrect heparin dosage, inaccurate infusion pump settings, and incomplete recordkeeping resulting in ~10,000 heparin medication errors per year.[49] Heparin therapy is especially challenging in pediatric patients because of their rapidly changing hemostasis system, guidelines based on adults, and challenges in collecting sufficient blood volumes.[40, 50] This results in thousands of children with hemorrhages or emboli annually.[51]

Because of these issues, heparin therapy must be carefully monitored with the activated partial thromboplastin time (aPTT) per nomogram and serves as a surrogate test for inactivation of numerous clotting factors including XIIa, Xia, and IXa[52]. However, this *in vitro* diagnostic blood test suffers from long turnaround times, a variable reference range, limited utility with low molecular weight heparin (LMWH), and broad intra- and inter-assay variance. More importantly, the aPTT is only a surrogate for heparin activity because it measures the conversion of fibrinogen to fibrin rather than antithrombin activity.[53] While anti-Xa analysis offers a more sophisticated metric of anticoagulation,[54] this test still has a long turnaround time and is limited to large research hospitals. Thromboelastography or the activated clotting time are established in the operating room, but are operator intensive, invasive, and time-consuming.[55] Furthermore, all of these tools

are limited by the low frequency with which blood can be sampled. While point-of-care testing can improve the frequency with which the aPTT is measured,[56] it still requires an operator to collect and prepare blood samples and is inaccurate at higher concentrations.[57] Thus, real-time and non-invasive tools to monitor heparin anticoagulation therapy could markedly improve the standard of care—one such approach to solving these limitations is imaging rather than *in vitro* diagnostics.

Tools to image anticoagulation must have good sensitivity, contrast, and temporal resolution—photoacoustic imaging is a novel technique that has these features. It uses a nanosecond laser pulse to generate thermal expansion and a pressure change for acoustic detection. It combines the high contrast of optical imaging with the speed of ultrasound. Photoacoustic imaging can use endogenous contrast such as hemoglobin and melanin[58, 59] as well as exogenous contrast[60, 61] including small molecules like methylene blue[62, 63] and nanoparticles.[64-67] While photoacoustic flow cytometry has measured emboli based on the absorption change and nanosensors have been reported for therapeutic drug monitoring of lithium[68], there is no approach to monitoring heparin therapy with acoustics. [17, 69]

Here, we describe a simple tool to quickly measure the concentration of heparin in both buffer and whole human blood using photoacoustic imaging. This work is inspired by colorimetric or optical methods[70-74] that measure heparin through a spectral shift or intensity change, but that failed when used in whole blood. In contrast, we found that the photoacoustic signal of the clinically-approved methylene blue dye increases dramatically upon binding to heparin (see Materials and Methods in Supplementary Material). Methylene blue (**Figure 2.1a**) is already used to visualize sentinel lymph nodes[75] and has broad absorption peaks between 500 and 700 nm (**Figure 2.1b**), but only nominal photoacoustic signal in the optical window typically used for imaging (680 - 900 nm; sensitivity of 7.1 μM at 680 nm, **Supplementary Figure 1.1a, d**). When electrostatically coupled to heparin (**Figure 2.1c**), however, the absorption (**Figure 2.1b**) and color of methylene blue changes (inset **Figure 2.1b**). Somewhat surprisingly, this heparin complexation also produces an intense (**Figure 2.1d**) increase in photoacoustic signal.

2.2 Measure Heparin Concentration Using Methylene Blue

We optimized the methylene blue concentration as a function of signal upon 6.4 U/mL heparin addition and found that 0.6 mM methylene blue produced the best contrast when added to heparin versus free methylene blue only in buffer (**Supplementary Figure 1.1b, e**)—this was used for all subsequent buffer-based experiments. Linear regression shows a strong correlation between photoacoustic signal and heparin concentration from 0 to 6.4 U/mL (exponential linear regression R^2>0.98) with a detection limit of 14.2 mU/mL (**Figure 2.1e**). Spectral photoacoustic imaging of these samples showed a maximal intensity absorbance at 680 nm with a characteristic peak near 710 nm (arrow in **Figure 2.1f**) and a 30-fold increase in photoacoustic signal with 6.4 U/mL heparin at 710 nm excitation. Heparin concentrations over 10 U/mL show decreased signal. Although further studies are needed to understand the mechanism underlying this decrease, possible reasons include aggregation of heparin or a phenomenon analogous to the "hook effect" seen in ELISA.[76] The relative standard deviation (RSD) of inter-assay (**Supplementary Figure 1.1c**) variation is <12%, and the signal is temporally stable (RSD<15%; **Supplementary Figure 1.1f**).

This signal was reversible via the known heparin antagonist protamine sulfate. Protamine reverses heparin overdose or deheparinizes patients after surgery at a ratio of 10 μg per 1 U heparin.[77] We found that the photoacoustic signal of the 5 U samples was completely neutralized with 50 μg of protamine sulfate in agreement with the reported dosing guidelines (**Figure 2.2a**); the absorbance spectra returned to baseline after protamine sulfate treatment (**Figure 2.1b**). The spectral fingerprint at 710 nm also disappears upon addition of protamine sulfate (**Figure 2.1f**). Photoacoustic signal linearly decreases as a function of protamine sulfate concentration (R^2>0.94; **Figure 2.2b**). As an initial test to validate the clinical compatibility of this assay, we studied the effect of antithrombin. There was no change in the photoacoustic signal when 40 μg of human antithrombin III was added to heparin and methylene blue (**Supplementary Figure 1.2a**).

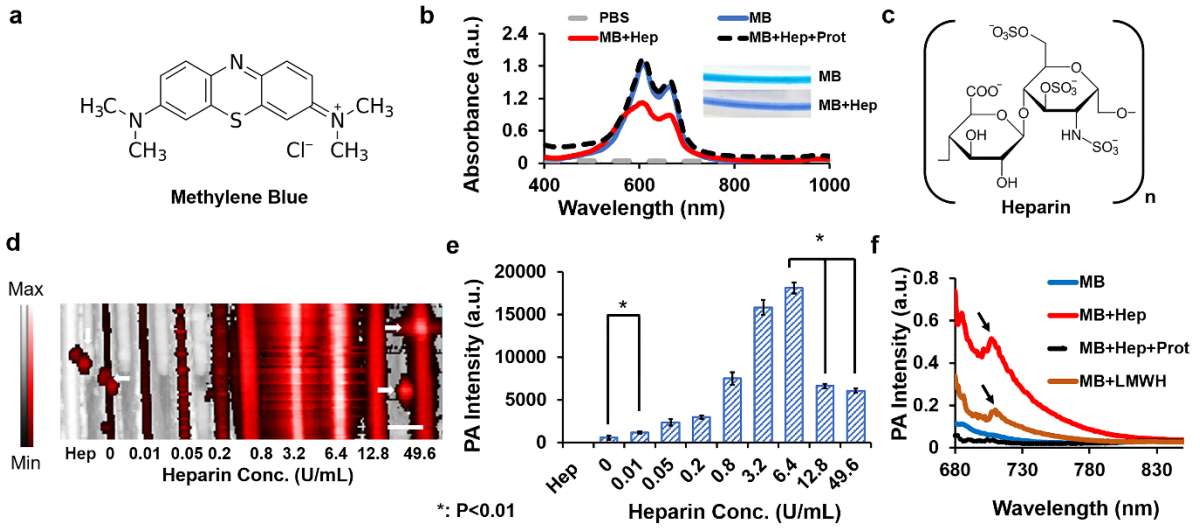

Figure 2. 1 Photoacoustic changes to methylene blue in the presence of heparin. (**a**) Chemical structure of methylene blue showing delocalized positive charge. (**b**) In the presence of 6.4 U/mL heparin, 0.6 mM methylene blue has a decrease in absorbance between 573 to 718 nm and a slight increase over 719 nm; these changes reverse upon addition of 8 mg/mL protamine. Inset in panel b represents the color change in methylene blue (MB) upon binding to heparin (MB+Hep). (**c**) Chemical structure of heparin with negative charge. Panel **d** shows imaging data of a phantom using 0.6 mM methylene blue and increasing concentrations of heparin. The image is a maximum intensity projection of photoacoustic data overlaid on ultrasound (B-mode) data. The black-to-white bar corresponds to ultrasound intensity, and the black-to-red bar corresponds to photoacoustic data. We noted a linear response between 0 and 6.4 U/mL of heparin. White arrows indicate dust particles producing extraneous signal. (**e**) Statistical analysis quantifies the data in (**d**) including a detection limit of 14.2 mU/mL and exponential linear regression (R^2>0.98) from 0-6.4 U/mL. **f**) Photoacoustic spectral data of the 6.4 U/mL sample shows a peak near 710 nm that is characteristic of the heparin and LMWH binding (arrows). This peak and the overall magnitude of the photoacoustic signal change decreases with protamine sulfate addition. Here, PA, MB, Hep, and Prot stand for photoacoustic, methylene blue, heparin, and protamine, respectively. The scale bar in (**d**) is 3 mm.

Similar data were collected with LMWH (**Figure 2.2c, d**). The photoacoustic intensity of methylene blue treated with 1.6 mg/mL LMWH (enoxaparin sodium) is 7-fold higher than the signal of methylene blue only with a detection limit of 1.4 μg/mL. The photoacoustic spectrum of LMWH also showed a peak at around 710 nm at concentrations over 5 U/mL (arrow in **Figure 2.1f**). This spectral feature could potentially discriminate the heparin- or LMWH-specific signal from the photoacoustic signal of hemoglobin, deoxyhemoglobin, or melanin.

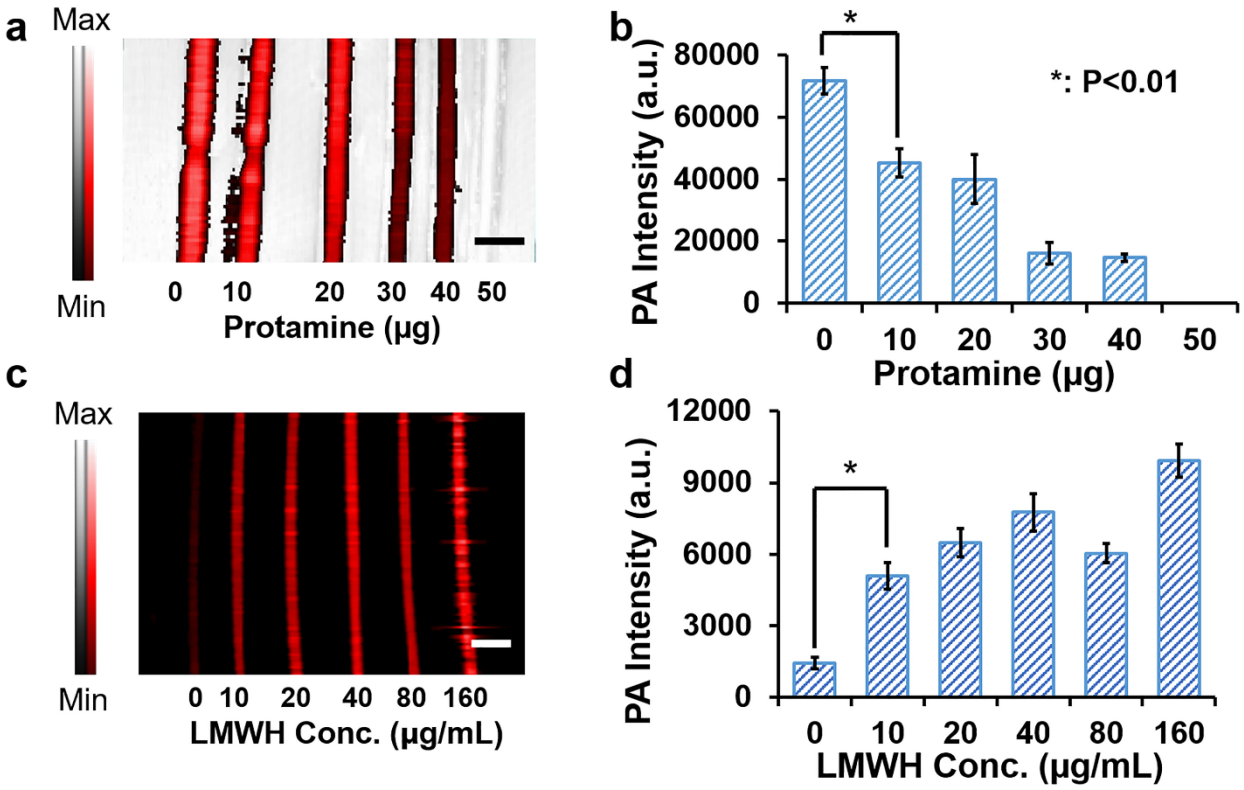

Figure 2. 2 Signal reversibility and use with LMWH. (a, b) Protamine sulfate caused a dose-dependent decrease in photoacoustic signal when added to a 5 U heparin solution. This relationship was linear at R^2>0.94, and complete neutralization occurred at 50 µg of protamine sulfate (known stoichiometry is 10 µg per 1 U heparin43). (c, d) Photoacoustic imaging can also be used to monitor LMWH with a detection limit of 1.4 µg/mL. Scale bars in (a) and (c) are 3 mm. Error bars represent the standard deviation.

The photoacoustic signal is generated by methylene blue/heparin complex. Methylene blue has a net positive charge via the sulfonium and nitrogen groups that can associate with heparin's negative charge. This causes a partial charge transfer to decrease the π electron energy on the dye and increase the transition energy to ΔE = 2.304 eV or a λ_{max} of ~550 nm[78]. The absorption from 719 – 850 nm increases 1-35% with 6.4 U/mL heparin (**Supplementary Figure 1.2b**). To measure any background signal from the heparin/protamine complex, we measured these species in a phantom. While an increased absorbance (due to scatter) was noted, no photoacoustic signal was seen (**Supplementary Figure 1.2c, d**) because there is no chromophore.

It seems unlikely that either the small increase in near IR absorbance or fluorescence quenching (**Supplementary Figure 1.2e**) is responsible for the large increase in photoacoustic signal. The heparin binding likely causes methylene blue to have faster heat transfer to the solvent. When the small molecule is more strongly associated with the heparin polymer than the solvent, more of its absorbed incident energy is released as photoacoustic thermal expansion than vibrational energy to water molecules. This is analogous to the reduced interfacial thermal resistance seen with silica-coated gold nanorods.[79] The signal reversibility via protamine helps confirm this hypothesis. Protamine has a higher positive charge than methylene blue, and it has greater affinity for heparin. This photoacoustic signal decreases as methylene blue becomes dissociated from heparin due to heparin/protamine binding.

2.3 Validation Using Blood Samples

We next validated this technique in blood. Blood contains hemoglobin and deoxyhemoglobin that can also produce photoacoustic signal,[58] and thus validating this approach in blood was an important next step. We used a slightly higher concentration of methylene blue in the blood experiments (0.8 mM) because the hemoglobin in whole blood can increase photoacoustic baseline signal. While there was a signal increase when methylene blue was added to blood (**Supplementary Figure 1.3a)**, the addition of heparin increased this signal even further. Blood samples (n=3) with 0.025, 0.05, 0.1, 0.2, and 0.4 U/mL heparin and 0.8 mM methylene blue provides 2, 4, 11, 19, and 24% higher signal than blood with 0.8 mM methylene blue only, respectively (**Figure 2.3a, b**). The RSDs of these samples were <8% with a logarithmic regression of R^2>0.97. The detection limit was 0.28 U/mL, and the signal was stable (<5% variation) for at least 15 minutes (**Supplementary Figure 1.3b**). This is much more stable than the value seen in buffer (**Supplementary Figure 1.1f**)—the lower signal stability in buffer may be due to more association/dissociation events due to fewer stabilizing proteins.

We also studied blood with higher heparin concentrations, and blood/methylene with 5 U/mL had 20-fold higher signal than blood with 0 U/mL heparin (**Supplementary Figure 1.3c**).

Importantly, the decreased signal intensity seen at high concentrations in buffer was not present in blood perhaps because the albumin and other serum proteins stabilize the methylene blue/heparin complex.

Although the aPTT has shown variable correlation to heparin dose in human trials,[80] we next used aPTT testing to confirm the clinical relevance of this assay—samples were studied with both the imaging technique and the aPTT. The aPTT values were typical of human therapy (30 – 300 s). When these values were plotted versus the aPTT (**Figure 2.3c**), regression analysis showed good correlation between clotting time and photoacoustic signal (Pearson's r = 0.86; $p<0.05$) suggesting that this imaging data is representative of actual clotting time.

To study the temporal features of photoacoustics, we measured the time between heparin or protamine injection and signal increase in a methylene blue/human blood sample placed in a customized flow chamber. The photoacoustic signal increased 3.6-fold 31 seconds after the injection of 0.1 mL of 50 U/mL heparin (working concentration of 3 U/mL) in to 1.7 mL of blood/methylene blue complex (methylene blue concentration of 0.8 mM) (**Figure 2.3d; Video S1**). It took 32 seconds for the signal to decrease back to baseline after injection of 0.1 mL of 0.5 mg/mL protamine (**Figure 2.3d**). The delay between drug injection and photoacoustic signal enhancement or reduction could be due to the slow drug diffusion in the blood. Nevertheless, photoacoustics shows strong advantage in time compared to the current gold standard method (aPTT). We note that the signal increase here is lower than observed in **Supplementary Figure 1.3c**. This is because the 2-mm thick plastic walls of the custom flow chamber.

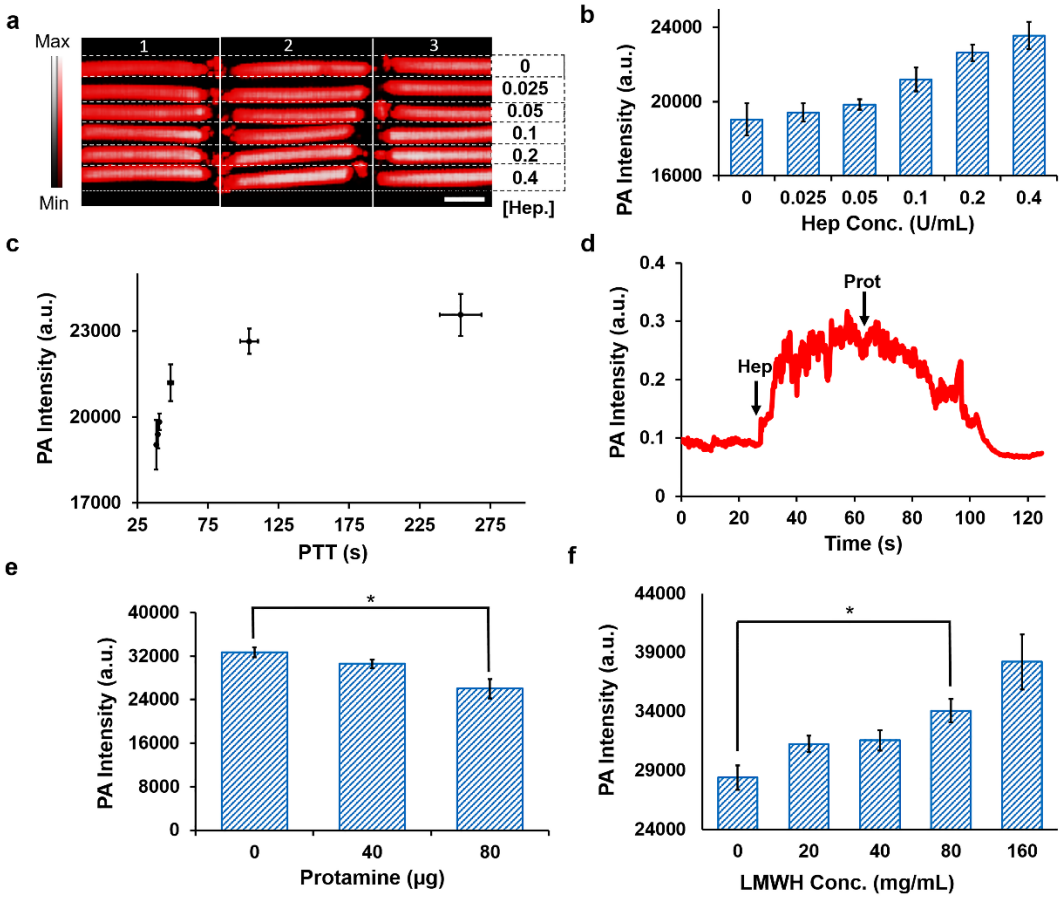

Figure 2. 3 Photoacoustic signal in whole human blood. (**a**) Photoacoustic image of plastic tubing containing human blood with 0.8 mM methylene blue and increasing concentrations of heparin with 0.8 mM methylene blue (n=3 replicates). Scale bar in (**a**) is 3 mm. Panel (**b**) quantitates the three replicates in (**a**), and the detection limit of heparin is 0.28 U/mL. Panel (**c**) plots the photoacoustic intensity versus aPTT. The Pearson's correlation coefficient (r) was 0.86; $p<0.05$). Panel (**d**) shows the photoacoustic signal changes of blood/methylene blue mixture as a function of time when heparin (at 27 seconds) and protamine (at 68 seconds) were added. Panel (**e**) shows that the heparin signal is reversible in whole blood with titration of protamine—the known heparin antagonist. **(f)** This approach also has utility with increasing concentrations of LMWH in methylene blue-doped human blood; the lowest concentration of LMWH can be detected in blood is 72 µg/mL. Error bars represent the standard error.

Protamine sulfate reversal was further quantified in blood samples. The signal was significantly ($p<0.01$) reduced when 80 µg of protamine was added to the heparinized blood **(Figure 2.3e)**. Spectral data (**Supplementary Figure 1.3d**) confirmed the reversal of methylene blue/heparin binding, although the spectra of the methylene blue/heparin complex was slightly different from the spectra measured in buffer (**Figure 2.1f**) due to the presence of erythrocytes. The characteristic peak at 710 nm only occurred at more than 50 U/mL heparin in blood. This could potentially be used to signal an overdose event.

We noted similar signal enhancements with LMWH (**Figure 2.3f**), and the imaging signal correlates to LMWH concentration (R^2>0.97; **Figure 2.3f**). The signal enhancement with 160 μg/mL LMWH and 0.8 mM methylene blue is 35% higher than methylene blue only with a limit of detection of 72 μg/ml. This is important because LMWH is currently monitored with the anti-Factor Xa ELISA testing[81]—the aPTT cannot monitor LMWH therapy[81, 82]. Thus, future work will be dedicating to improving the LMWH utility.

The correlation between the photoacoustic data and the aPTT—as well as the protamine sulfate-based deheparinization—confirms that the imaging signal offers functional information about blood clotting time. This approach is sensitive to clinically relevant heparin concentrations. We showed a sensitivity of 14.2 mU/mL in buffer and 0.28 U/mL in whole blood. These detection limits are lower than the concentrations used in thromboembolism (7-8 U/mL, 35,000-40,000 U/24 hours)[83], acute myocardial infarction (2.5 U/mL,12,500 U/12 hours)[84], coronary angioplasty (2 U/mL)[85], and cardiopulmonary bypass (5.6 U/mL)[86] as well as the lower doses used in treatment of extracorporeal membrane oxygenation 0.5 U/mL (50 U/kg)[87]. These concentrations all assumed a blood pool volume of 5 L.

2.4 Fabrication of Hydrogel Sensor for Heparin Sensing

Methylene blue is already FDA-approved with minimal effects on anticoagulation[88]. This approach could be developed for fingerprick samples and a bedside photoacoustic analyzer. However, to better harness the capabilities of imaging, we envision a wearable, heparin-sensitive catheter that not only delivers heparin, but also monitors clotting time. To encapsulate the dye on a usable substrate, we created a hybrid of agar gel and silica nanoparticles that could be coated on the surface of the catheter. Simply mixing methylene blue with agarose resulted in quick release of 40% of the dye (**Figure 2.4a)**. While methylene blue could be stably bound to Stöber silica nanoparticles (SSNP in **Figure 2.4b, c**), there was no photoacoustic response when heparin was added. The surface charge of these nanoparticle is -23 mV, which is too negative to allow association between the nanoparticle-bound dye and negatively charged heparin. Therefore,

careful nanoengineering was required to produce a material that was both stable and responsive to heparin.

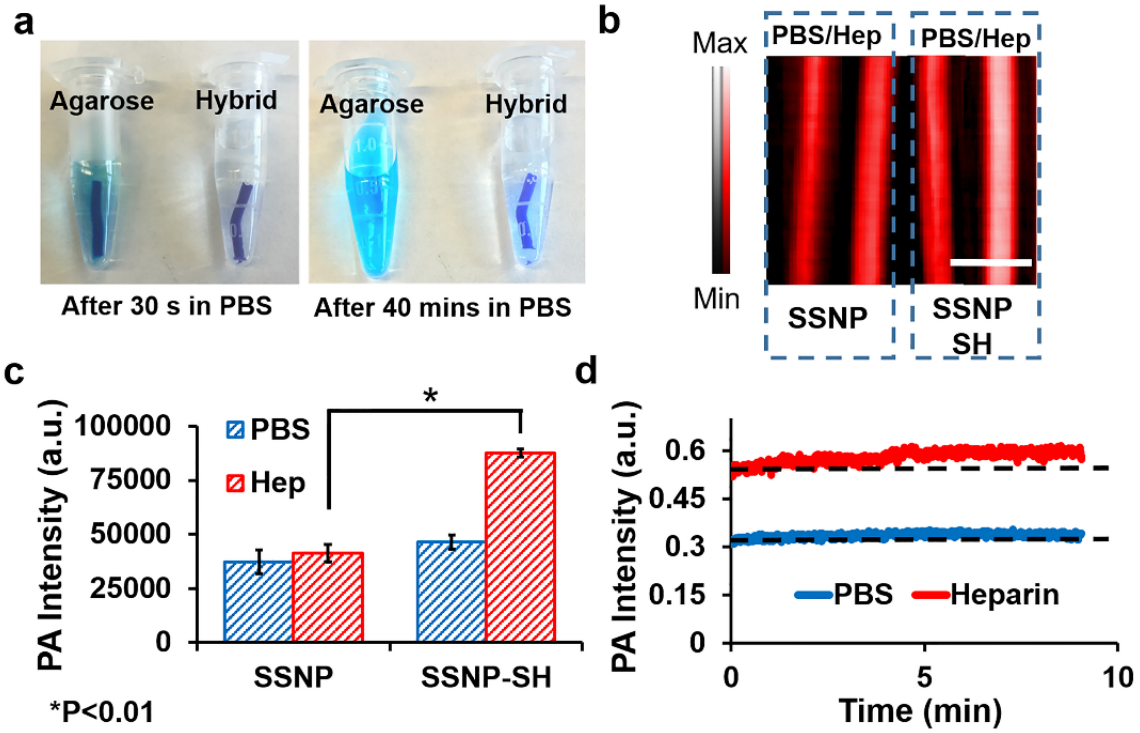

Figure 2. 4 Optimization of material for a heparin-responsive catheter. (a) Methylene blue in agarose was not stable with more than 40% methylene blue release in PBS after 40 minutes. The addition of nanoparticles for a hybrid material reduced this release to less than 10%. (b) Photoacoustic images of methylene blue loaded on as-made silica nanoparticles (SSNP; -23 mV) and methylene blue loaded on thiol-coated silica nanoparticles (SSNP-SH; -15 mV). Both were treated with PBS and heparin (Hep), but only the thiol-coated nanoparticles were responsive to heparin. The lower zeta potential facilitated the photoacoustic signal increase. (c) Methylene blue-loaded SSNP-SH treated with heparin offers significantly more signal than SSNP-SH treated with PBS or SSNP. (d) The nanoparticle/agar hybrid material was treated with PBS or 10 U/mL heparin and imaged at 680 nm for 9 minutes with no decrease in signal.

To tune the nanoparticles, we treated them with (3-mercaptopropyl)trimethoxysilane (MPTMS) to adjust the zeta potential to -15 mV (SSNP-SH in **Figure 2.4b, c**). We used this material with agar gel to create a coating on a catheter tube (**Figure 2.5a**). Absorption data showed that the hybrid material has a methylene blue concentration of 1.5 mM with low methylene blue release (<10%) after 40 minutes incubation in PBS (**Figure 2.4a**). More importantly, the methylene blue on these modified nanoparticles remain responsive to heparin with 51% more photoacoustic signal at 10 U/mL heparin than PBS (**Figure 2.5b**) for 1-hour incubation. The signal enhancement was stable after constant imaging at 680 nm for 9 minutes (RSD<4%) **(Figure 2.4d).**

This system was also reversible. When the 50 U/mL-treated device was reversed with protamine (8 mg/mL), the signal decreased by 42% versus no protamine treatment (**Figure 2.5b**). The higher signal of the heparin-treated hybrid versus PBS-treated hybrid is likely due to interactions between methylene blue and heparin, which increases the photoacoustic signal and decreases diffusion of this complex and free methylene blue into solution.

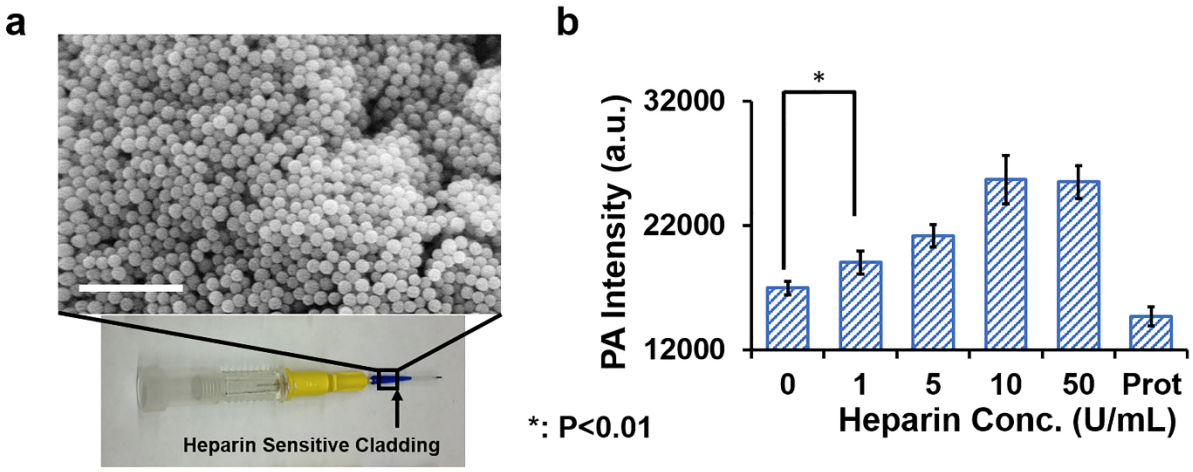

Figure 2. 5 Sensitivity of the hybrid material in detecting heparin. (a) The proposed device uses methylene-blue coated nanoparticles embedded in agar and coated on the exterior of a venous catheter. This would be used for in vivo anticoagulation monitoring. The inset is a scanning electron microscope image of the agarose/silica nanoparticle hybrid. (b) This design was used to measure increasing concentrations of heparin as well as a protamine control. Scale bar in (a) is 2 μm.

The strengths of this approach include the rapid turnaround time, excellent sensitivity, good correlation to the aPTT, and flexibility with both heparin and LMWH. While the aPTT is the gold standard for monitoring anticoagulation, it suffers from long turnaround times and limited utility with LMWH. In contrast, it only takes 0.2 second for photoacoustic imaging to acquire one data point (5 Hz imaging) and can be used with both unfractionated and LMWH, although more than one frame might be needed for accurate and stable signal. This approach could also leverage spectral or ratiometric imaging to decouple the heparin-specific signal from other sources of photoacoustic signal.

Limitations to this approach include different PA background due to hydration state, oxygenation, body fat content, and location of the catheter. However, we will monitor the change

in signal versus baseline as a function of heparin therapy to control for these variations. This approach also does not discriminate between the anticoagulant and non-anticoagulant glycosaminoglycan sequences on heparin or LMWH—similar to all other existing tools to monitor heparin. In addition, the current generation of the nanoparticle hybrid has a slower response (~ 1 hr) than free methylene blue in blood (~ 30 sec) because of the porous nature of the agar/nanoparticle hybrid material and the longer time needed for the heparin to diffuse into the gel network as well as the time kinetics of methylene blue release from the nanoparticle to associate with the heparin. Future work is refining this device for faster responses.

Most importantly, we do show that the photoacoustic signal correlates to activity—and this is the key metric of interest to clinicians. We also show no activation by endogenous glycosaminoglycans (**Supplementary Figure 1.3a**). Although there are a wide variety of species present in blood, we can still detect clinically relevant heparin concentrations above this background (**Supplementary Figure 1.3a**).

Future work will include the use of photoacoustic signal processing and other phenothiazinium derivatives to increase the sensitivity and specificity. Blood processing, phlebotomy protocols, surgery type,[89] and donor health can all affect the signal contrast between the probe and probe/heparin and will be optimized. Ongoing work will continue to refine this hybrid catheter for use with animal models of anticoagulation therapy. When implanted, this would allow heparin therapy to be monitored without a blood sample.

2.5 Conclusion

In this paper, we report for the first time that methylene blue has a significant and dose-dependent increase in photoacoustic signal in the presence of both heparin and LMWH. This signal was validated in both buffer and whole blood with good correlation to the gold standard aPTT; the signal was reversible with protamine sulfate deheparinization. Photoacoustic imaging is a real time technique, and methylene blue is an FDA-approved dye. Thus, this method is promising for real-time monitoring of anticoagulation therapy to quickly titrate the patient into the

therapeutic window. This has potentially profound implications because acoustics-based wearable sensors would have low costs, good transmission through tissue without scatter/diffusion, no ionizing radiation, and high temporal and spatial resolution in contrast to many optical or electrical sensors.

Chapter 2, in full, is a reprint of the material as it appears in *Nano Letters*, 2016, 16 (10), pp 6265–6271. Junxin Wang, Fang Chen, Santiago J Arconada-Alvarez, James Hartanto, Li-Peng Yap, Ryan Park, Fang Wang, Ivetta Vorobyova, Grant Dagliyan, Peter S Conti, Jesse V Jokerst. The dissertation author was the primary investigator and author of this paper.

Chapter 3 A Mechanistic Investigation of Methylene Blue and Heparin Interactions and Their Photoacoustic Enhancement

We recently reported a real-time method to measure heparin in human whole blood based on the photoacoustic change of methylene blue (MB). Intriguingly, the MB behaved unlike other "turn on" photoacoustic probes—the absorbance decreased as the photoacoustic signal increased. The underlying mechanism was not clear and motivated this study. We studied the binding mechanism of MB and heparin in water and phosphate buffer saline (PBS) with both experimental and computational methods. We found that the photoacoustic enhancement of the MB-heparin mixture was a result of MB-heparin aggregation due to charge neutralization and resulting sequestration of MB in these aggregates. The sequestration of MB in the MB-heparin aggregates led to decreased absorbance—there was simply less free dye in solution to absorb light. The highest photoacoustic signal and aggregation occurred when the number of negatively charged sulfate groups on heparin was approximately equal to the number of positively charged MB molecule. The MB-heparin aggregates dissociated when the sulfated group of heparins was more than the MB molecules because of the electrostatic repulsion between negatively charged sulfate groups on heparin. PBS facilitated MB dimer formation regardless of heparin concentration and re-precipitated free MB in aggregates due to ionic strength and ionic shielding. Further molecular dynamics experiments found that binding of heparin occurred at the sulfates and glucosamines in heparin. Phosphate buffer ions could interact with the heparin via sodium ions to impair the MB-heparin binding. Finally, our model found 3.7-fold more MB dimerization upon addition of heparin in MB solution confirming that heparin facilitates MB aggregation. We conclude that addition of heparin in MB *decreases* the absorbance of the sample because of MB-heparin aggregation and fewer MB molecules in solution; however, the aggregation also *increases* the PA

intensity because the MB molecules in the MB-heparin aggregate have reduced degrees of freedom and poor heat transfer to solvent.

3.1 Introduction

Methylene blue (MB) is a phenothiazinium dye with diverse biomedical applications. It is a photosensitizer used in photodynamic therapy and as a contrast agent in photoacoustic (PA) imaging.[33, 90-95] Moreover, MB is US Food & Drug Administration-approved for managing methemoglobinemia[96] and is effective to against malaria[97].

MB has also been used in monitoring heparin.[98-100] Heparin is a highly sulfated anionic glycosaminoglycan that activates antithrombin, which silences the clotting factors thrombin and Factor Xa.[101] Intriguingly, mixing heparin and MB decreases the MB absorption[102] and increases the resonant Rayleigh scattering[17] of MB; thus, MB can monitor heparin. MB can also measure heparin electrochemically because heparin reduces the peak current of MB in cyclic voltammetry.[98] More recently, we reported a real-time PA method to monitor heparin in blood using MB—the PA intensity of MB significantly increased upon the addition of heparin.[100] In PA imaging, signal is proportional to absorption[103-105]; however, we were surprised to find that the absorbance of MB decreased with increasing heparin dose yet the PA signal increased—this is in contrast to most other "turn on" PA probes whereby increased absorption facilitates increased PA signal. That observation motivates this work.

Mechanistic studies of the MB/heparin interaction are rare and mainly limited to spectroscopic studies in water. Previous research found that 610 nm and 660 nm are characteristic peaks of the MB dimer and monomer, respectively.[106] Upon addition of heparin, the absorbance of MB shifted from 660 to 610 and eventually to 570 nm, which indicated the formation of MB dimers and MB self-aggregates (i.e. H-type aggregates).[107, 108] This shift is caused by the coupling between MB molecules that splits an excited singlet state of MB into two excitonic states. The absorption from ground state and the upper excitonic state blue-shifts the absorbance spectrum.[109, 110] However, these studies lacked deeper mechanistic detail and only investigated the interaction in water, which disregards the key role of pH and ionic strength—our interest lies

in measuring heparin with PA in whole blood and motivates this mechanistic study of the interaction between heparin and MB in more biologically relevant solvents.

Here, we describe MB-heparin interactions in water and phosphate buffer saline (PBS) including the identification of MB-heparin aggregation. We found that formation of MB-heparin aggregate was responsible for the absorbance reduction and PA enhancement of MB upon addition of heparin. PBS could impair the MB-heparin binding by shielding the MB and heparin. We also include simulation results that further detail the heparin binding residues and identify the intramolecular interactions that stabilized the MB-heparin aggregation.

We used nuclear magnetic resonance (NMR), dynamic light scattering (DLS), and optical absorbance spectroscopy to study the binding between heparin and MB as well as the change in the PA signal. We then characterized the impact of PBS and solvent ionic strength on the binding and finally performed molecular simulations to support the experimental observations.

3.2 MB-heparin Aggregation Induces PA Enhancement

The PA enhancement of MB in the presence of heparin reverses when heparin is above a certain concentration[100]. Therefore, we hypothesized that MB electrostatically binds to heparin, and the binding kinetics varied as a function of heparin concentration. Heparin is a highly sulfated and negatively charged polysaccharide, and thus we estimated the number of sulfate groups on heparin for MB binding to characterize the effect of heparin concentration as follows: Heparin has an antithrombin binding pentasaccharide site as minor repeat units and two trisulfated disaccharide units as major repeat units in its backbone[111] (**Supplementary Figure 2.1**). The molecular weight of commercial heparin varies, but the number of sulfate in heparin can be estimated via the number of the major trisulfated disaccharide repeat units. Each major repeat unit has 3 sulfate groups for 3 MB molecules to bind with, and the molecular weight of each repeat unit is 591.4 g/mol, which was used to estimate the number of sulfate group of heparin per unit weight. To study the effect of heparin concentration on PA signal, we prepared 0.90 mg/mL MB and varied the amount of heparin in the MB solution from 0.09 to 0.85 mg/mL. Thus, the ratio of MB to the sulfate groups on heparin was 1:0.2- 1:1.8.

We studied these samples with NMR. The chemical shift and relaxation time of MB are sensitive to the micro-environment and distance between MB molecules. Therefore, the NMR spectra of aqueous solutions containing different ratios of heparin to MB were studied to characterize the binding of MB to heparin. First, the MB concentration was optimized to 0.9 mg/mL to achieve sufficient signal to noise ratio in ^{1}H NMR. MB is a positively charged dye and has three types of aromatic protons at the phenothiazinium central ring and two identical protons at the dimethyl amino groups corresponding to 7.40, 7.11, 6.87 ppm, and 3.14 ppm in the NMR spectrum

(**Figure 3.1A** inset).[112, 113] Proton 1 changed the most upon addition of heparin. The NMR signal at 7.40 ppm decreased by 75.7% with a downshift of 0.1 ppm when the heparin:MB ratio increased from 0.2 to 1.0 (**Figure 3.1A**). The decrease in NMR intensity suggested precipitation of the MB-heparin aggregates because the protons of MB sequestered in the aggregates should have reduced NMR signal due to concentration quenching.[113]

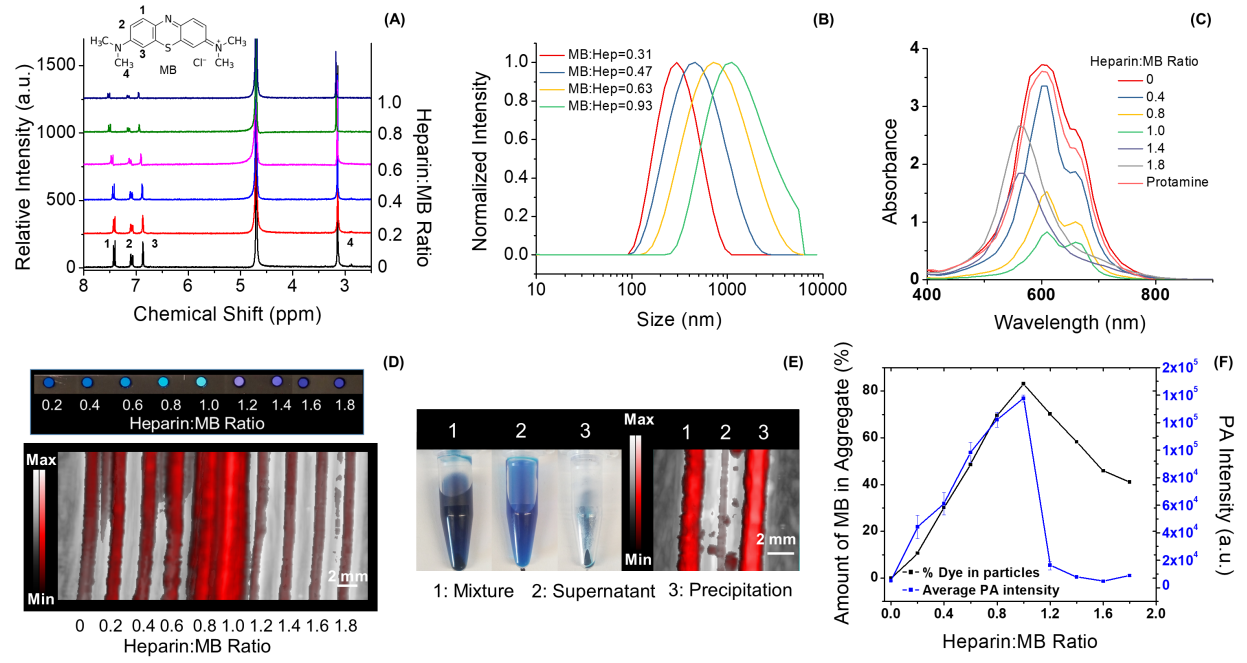

Figure 3. 1 MB aggregation upon addition of heparin. Panel A plots the NMR spectra of MB at the heparin:MB ratios of 0 to 1.0. Peaks 1, 2, 3, and 4 in the spectrum correspond to the protons shown on the structure of MB (inset). The NMR intensity of both proton 1 and proton 4 (**Supplementary Figure 2.2**) decreased the most (i.e. 76%) when the heparin:MB ratio approaches to 1.0, suggesting precipitation of MB-heparin aggregates. Panel B shows the DLS result of MB-heparin aggregates as a function of MB concentration. The size of the aggregates was increased from 335 nm to 1632 nm when the MB:heparin ratio was increased from 0.31 to 0.93. The absorbance spectra of the samples in panel A are shown in panel C. The absorbance intensity at 610 nm decreased 4.5-fold when heparin:MB ratio equals to 1.0. A higher heparin:MB ratio at 1.2-1.8 blueshifts the absorbance peak to 570 nm suggesting formation of MB self-aggregates (i.e. H-type aggregates). A control experiment using protamine (i.e. antagonist of heparin) reverses the spectral change. Panel D shows the color and PA image of the samples of panel C. In the sample with heparin:MB at 1.0, the MB-heparin aggregates were collected by centrifugation—these aggregates cause most of the PA signal in the mixture (panel E). Panel F quantifies the PA intensity of the samples in panel D and the amount of MB in the MB-heparin aggregates. The similar trend indicates that the MB-heparin aggregation increases PA intensity. The error bars in panel F represent the standard deviation of 8 regions-of-interest in the sample.

DLS analysis revealed that the size of MB-heparin aggregate increased as a function of MB concentration. At a constant heparin concentration (0.00625 mg/mL), increasing the

MB:heparin ratio from 0.31 to 0.93 increased the size of the MB-heparin aggregate by 4.9-fold (**Figure 3.1B**). However, increasing the heparin:MB ratio from 0.08 to 0.64 had only 1.5-fold increase on the aggregate size (**Supplementary Figure 2.3**). The more significant increase governed by the MB concentration than heparin concentration suggests that the MB-heparin aggregation and precipitation results from charge neutralization between MB and heparin and interactions between MB molecules such dimerization that could facilitate aggregation of different MB-bound heparins.

The absorbance of samples with 0.9 mg/mL MB with heparin to MB ratio from 0.2 to 1.8 were found to correlate with the amount of MB in the MB-heparin aggregates. Despite a constant MB concentration across all mixtures, the absorbance of MB at 660 and 610 nm decreased 4.0-fold and 4.5-fold when heparin:MB was equal to 1.0:1.0 (**Figure 3.1C**), respectively. Concurrently, 85% of the MB was sequestered in the MB-heparin aggregates at heparin to MB ratio of 1.0 (**Figure 3.1D**). This indicated that the decrease of absorbance at the 610 and 660 nm was a result of MB-heparin aggregation that decreased the amount of free MB dimer and monomers and therefore the absorbance in the solution.

Higher heparin concentrations beyond a 1:1 ratio of heparin to MB led to MB *self*-aggregates rather than MB-heparin aggregates as indicated by the absorbance peak at 570 nm[108]. Meanwhile, the amount of MB in the MB-heparin aggregates decreased by 2.0-fold (**Figure 3.1F**). The initial color change of MB as a function of heparin as well as the reversal when the heparin concentration seen at heparin:MB over 1.0 also indicates the aggregation and dispersion of MB-heparin (**Figure 3.1D**). This is analogous to the precipitation of other dyes such as rhodamine 6G in aqueous sodium dodecyl sulfate.[114] The dispersion of MB-heparin aggregate was likely due to the electrostatic repulsion between the heparin chains. Therefore, MB neutralized heparin and formed MB-heparin aggregates when the heparin:MB ratio was between 0 to 1.0. Higher doses of heparin dispersed the MB-heparin aggregates likely because of the electrostatic repulsion between negative heparin chains.

The PA enhancement of the MB-heparin mixture was also a function of heparin to MB ratio. The PA intensity of the MB at heparin:MB ratio of 1.0 measured at 680 nm was 26.7-fold higher than MB alone, but it decreased 15.6-fold when the heparin:MB ratio was 1.8 (**Figure 3.1D and 3.1F**). This was very similar to the trend seen for the amount of MB in the MB-heparin aggregates (**Figure 3.1F**). We also found that the MB-heparin aggregates contributed most of the PA intensity of the MB-heparin mixtures. We separated the aggregates and soluble fractions and found that the PA intensity of the precipitate was 43.1-fold higher than the supernatant suggesting that the PA enhancement was a result of MB-heparin aggregation (**Figure 3.1E**). Therefore, formation of MB-heparin aggregates contributes to the photoacoustic increase. The enhanced PA intensity caused by the MB-heparin aggregation was likely a result of the reduced degrees of freedom of the MB (its molecular motions are restricted relative free MB). This led to poor heat transfer from the aggregate to the solvent and increased the thermal gradient between the aggregate and solution.[115]

3.3 Impact of PBS

Next, we prepared the MB-heparin samples in PBS using heparin:MB ratio of 0.8 and 1.8 to study the impact of PBS on MB-heparin aggregation and MB self-aggregation. At a heparin:MB ratio of 0.8 and MB concentration at 0.15 mM, PBS had minimal influence on absorption wavelength but increased the absorbance by 24 and 9% at 610 and 660 nm, respectively, compared to the MB-heparin sample in water (**Figure 3.2A** Hep:MB=0.8 in water) (**Figure 3.2A** Hep:MB=0.8 1X PBS). This led to a 22% PA increase at 680 nm excitation (**Figure 3.2B** 0.8 H_2O and 0.8 PBS). PBS had an even more pronounced impact at heparin:MB of 1.8 (MB still at 0.15 mM): PBS redshifted the absorbance of the sample from 570 to 610 nm (**Figure 3.2A** Heparin:MB=1.8 1X PBS) indicating disassociation of MB self-aggregates to MB dimer. The PBS also increased the PA intensity of the sample by 2.8-fold (**Figure 3.2B** 1.8 PBS). We suspected that this spectral shift and PA enhancement was due to the ionic strength rather than the pH of the PBS.

To test this, we performed a control experiment using 137 mM NaCl because PBS contains 137 mM NaCl and is much more concentrated than other buffer ions (i.e. 13.7 times higher than phosphate buffer and 50.7 times higher than potassium chloride). Adding 137 mM NaCl reversed the absorbance of MB-heparin mixture in water from 570 to 610 nm (**Figure 3.2A** Hep:MB=1.8 137 mM NaCl) with a spectral profile very similar to the effect of adding 1X PBS. To further verify that the ionic strength is responsible for the spectral shift, we increased the MB concentration to 2.4 mM and maintained the heparin:MB ratio at 1.0—it should take more PBS and NaCl to shift the absorbance from 570 to 610 nm. Indeed, we had to double the PBS or NaCl concentration to completely shift the absorbance of the sample from 570 nm to 610 nm (**Figure 3.2C**). This result suggests that the ions in PBS can disassociate the MB self-aggregate via ionic shielding leading to an absorbance redshift.

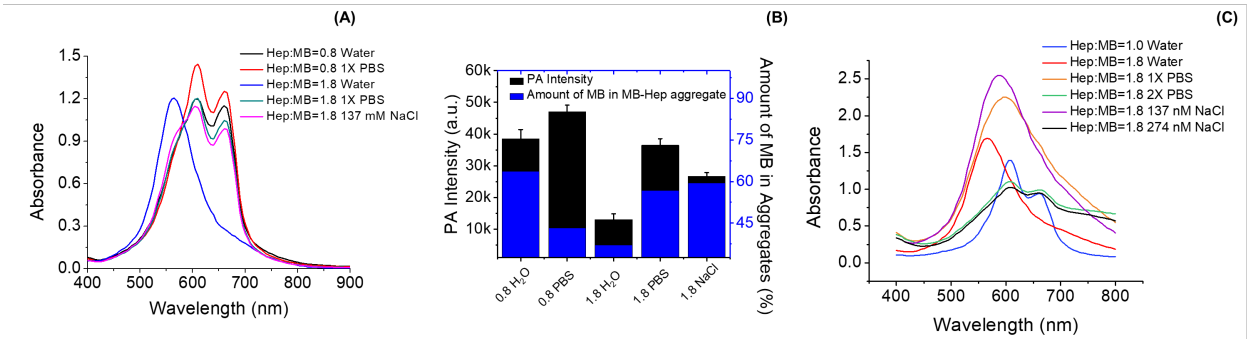

Figure 3. 2 Impact of PBS in the MB-heparin binding. Panel A compares the spectral change of MB-heparin complex in water and PBS. The MB-heparin sample with heparin:MB at 0.8 in PBS (red) had 24% and 9% higher absorbance at 610 and 660 nm than the sample prepared in water (black). At heparin to MB ratio of 1.8, the addition of 1X PBS in MB-heparin (green) redshifted the absorbance of the sample prepared in water (blue) from 570 to 610 nm. Adding 137 mM NaCl had a similar spectral profile (purple). Panel B shows the PA intensity (black) and the amount of MB in the MB-heparin aggregates (blue) of the samples in Panel A. At heparin:MB of 0.8, PBS (0.8 PBS) increased the PA signal of the sample in water (0.8 H_2O) by 22%. At heparin:MB of 1.8, adding PBS (1.8 PBS) and 137 mM NaCl (1.8 NaCl) in the sample prepared in water (1.8 H_2O) resulted in 2.8 and 2.0-fold increase in PA intensity as well as 1.5 and 1.6-fold in the amount of MB in MB-heparin aggregate. Panel C is the absorbance of 2.4 mM MB with heparin:MB ratio at 1.0 (blue) and 1.8 (red). Adding 1X PBS (orange) or 137 mM NaCl (purple) only redshifted the absorbance to 590 nm and 600 nm. Doubling the PBS (green) or NaCl concentration (black) in the sample could shift the absorbance to 610 nm, like the absorbance of sample with Heparin:MB ratio at 1.0. This indicates that the ionic strength governs the disassociation of MB self-aggregates to MB dimer.

We further tested the influence of ionic strength on PA intensity of MB-heparin mixture with a heparin:MB ratio of 1.8 using 137 mM NaCl. The addition of 137 mM NaCl in the MB-

heparin sample had a 2.0-fold higher PA signal than the sample in water (**Figure 3.2B** 1.8 NaCl) and increased the number of aggregates. Compared to the MB-heparin sample with heparin:MB at 0.8, the sample with heparin:MB ratio at 1.8 has more heparin that uses more NaCl as counter ions—this minimizes the shielding effect and leads to more heparin-MB aggregates.

3.4 Molecular Modeling of MB-heparin Binding

Finally, we used molecular modeling to study the binding details of MB and heparin (repeat unit used in the simulation shown in **Figure 3.3A**) as well as the role of heparin in MB self-aggregation. To study the impact of PBS in the MB-heparin binding, simulations were first performed using 0.154 M NaCl without phosphate ions to balance the charge of MB and heparin. The binding process of MB and heparin were dynamic in both 0.154 M NaCl and PBS with rapid association and dissociation of the MB with heparin (**Video S2** and **Video S3** for NaCl and PBS, respectively). We found that the PBS ions shielded MB and the heparin because phosphates associated with heparin via multiple Na^+(**Supplementary Figure 2.4**).

We also compared the number of MB dimers formed between the system with MB alone and the system with MB and heparin. Dimer formation was defined as a distance of less than 4.8 Å between the centers of mass between two MB molecules. Dimer formation for three trials of the system containing 14 MB molecules with and without heparin present were analyzed. The addition of heparin increased MB dimer formation by 3.7-fold compared to MB alone ($p<0.03$, **Figure 3.3B**). As all other variables, including the placement of MB within the solvation box, were kept constant. These results suggested that the presence of heparin increases the frequency of MB dimer formation and facilitates MB-heparin aggregation.

We also studied the mechanism by which MB dimer formation depends on heparin. This analysis aimed to determine if π-π interactions were a plausible explanation for dimer formation. We defined a MB-MB binding event as a distance less than 9.5 Å between the center of mass of MB molecules because this distance is the length of MB from terminal C to terminal C and accounts for all angles of MB binding other than a perpendicular binding event (no perpendicular

events were noted in any of the simulations). The frequency of binding events at 9.5 Å were compared to the frequency of binding events at 4.0 Å, which is the widely accepted upper limit of π-π interactions[116] (**Figure 3.3C**). This comparison revealed that of the dimers that were formed without heparin, only 17.6% had an orientation and distance indicative of a π-π interaction (**Figure 3.3D**). With heparin, 31.3% of the dimers had an orientation and distance suggestive of π-π interactions. These differences were statistically significant ($p<0.01$), and this result indicates that heparin enhances MB π-π stacking to facilitate MB precipitation into the MB-heparin aggregate.

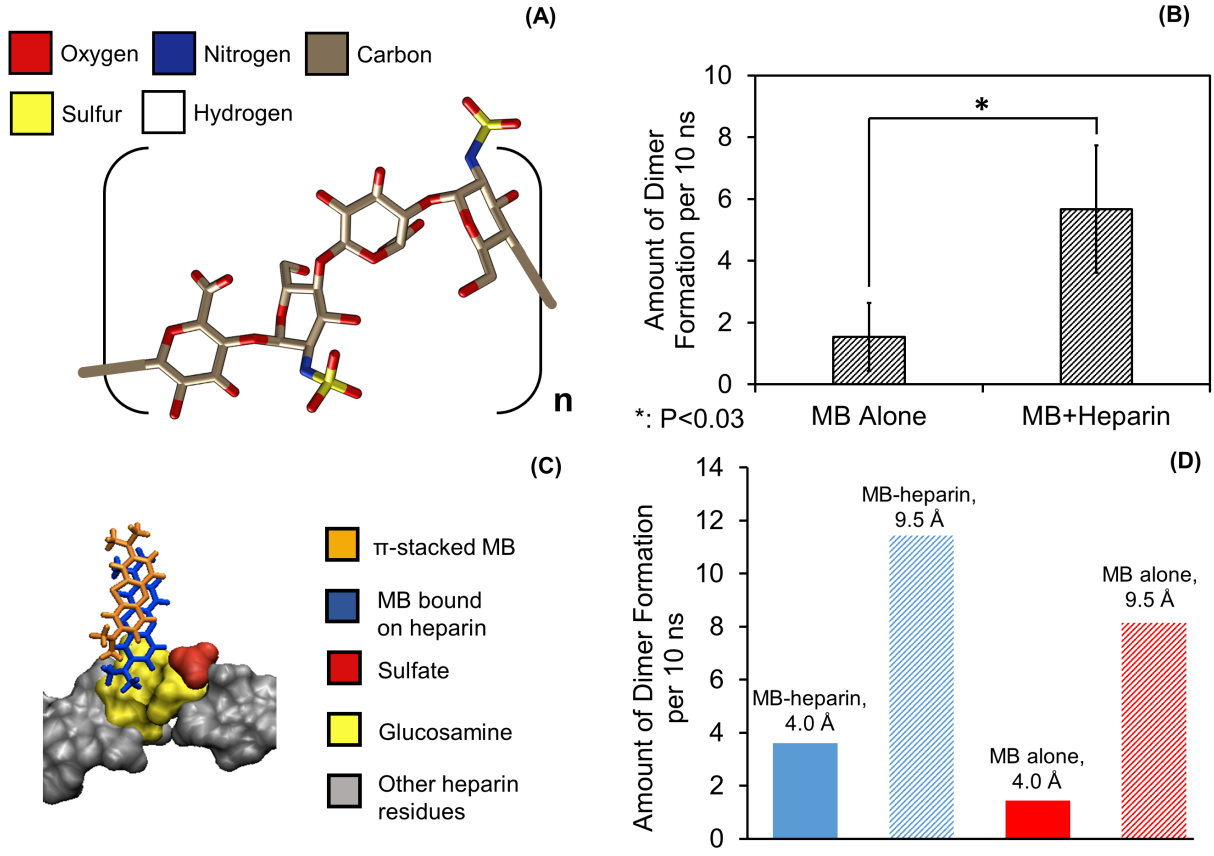

Figure 3. 3 Simulated binding kinetics of MB and heparin. Panel A shows one of the 6 repeating units of heparin simulated in solvent NaCl and PBS systems. Panel B shows that the MB system with heparin had on average 5.67±2.06 dimer formations per 10 ns, which is significantly more MB dimer formation than the system without heparin (1.53±1.10 dimer formations per 10 ns ($p<0.03$)). Panel C shows the π-π stacked MB dimer bound on the sulfate and glucosamine. The fraction of MB dimers formed by π-π stacking among the total number of MB dimers is shown in panel D. In the pure MB system, the π-π stacked MB dimer is 17.6% of the total dimers. The percentage increased to 31.3% upon addition of heparin. Error bars in B represent three replicate simulations runs.

To understand the heparin binding sites, we evaluated each monosaccharide unit in the simulated heparin structure for its energetic contribution to a MB binding event using Molecular Mechanics-Poisson Boltzmann Surface Area (MMPBSA) decomposition analysis[117]. **Figure 3.4A** showed that the spontaneity of a binding event was mostly due to the glucosamine (GlcN) and sulfate groups; thus, these residues were likely stable MB binding sites. The sulfate groups were distributed throughout the structure and underlie the anionic nature of heparin, and they strongly contributed to the overall energetics of a MB binding event. The interaction between MB and binding residues in heparin are electrostatic (**Figure 3.4B**), and this electrostatic interaction neutralizes the charge of both the heparin residue and MB upon binding.

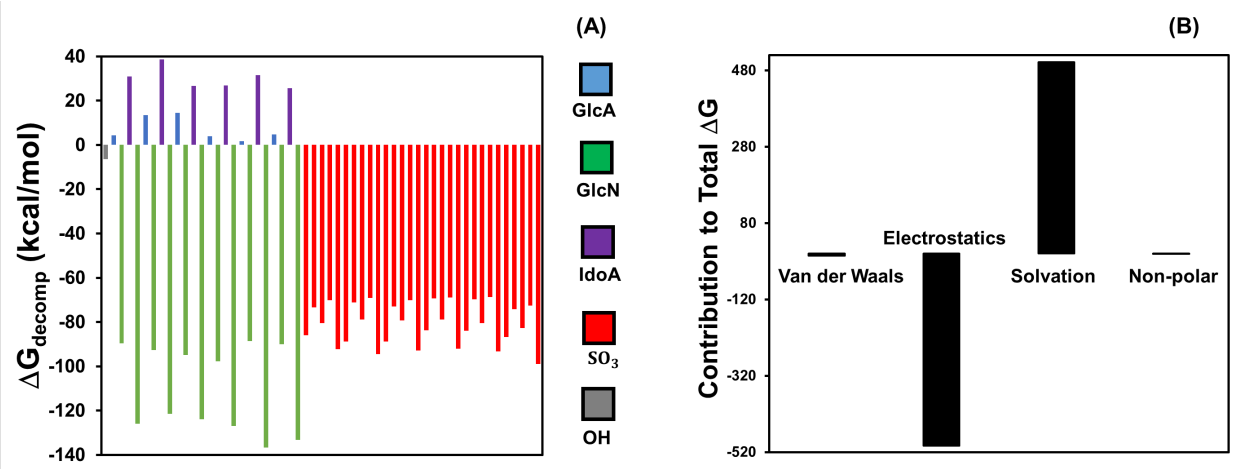

Figure 3. 4 Decomposition analysis of the binding energy. The energy decomposition results of heparin residues in the system of 7 MB molecules with 1 heparin are plotted in panel A. Here, positive values indicate a destabilizing effect, and negative values represent stabilizing residues with respect to a binding event. The glucosamine and sulfate residues were the largest contributors to the spontaneity of the MB binding event. The GlcA, GlcN, IdoA, SO_3, and OH represent glucuronic acid, glucosamine, idouronic acid, sulfate, and the hydroxide terminals that are not associated with other residues, respectively. The X axis represents different residues on the heparin. These monosaccharides are presented in the order that they appear in the polysaccharide; the sulfates are presented as a group although they are scattered throughout the structure. Panel B further details the energetic contributions of Van der Waals forces, electrostatic interactions, the solvation free energy upon binding of the ligand to the receptor, and the non-polar contribution of the surface, respectively. Electrostatic interactions were the greatest stabilizing force to the energetics of binding, while solvation effects were found to be the most destabilizing force.

3.5 Conclusion

In summary, we studied the binding of MB and heparin in experiments and simulations. In water, MB aggregates with heparin via charge neutralization, resulting in MB sequestration in

these aggregates. Therefore, the MB-heparin aggregation reduces the absorbance of the sample because there are fewer MB molecules in solution; however, this aggregation also *increases* the PA intensity because the MB molecules in the MB-heparin aggregate have reduced degrees of freedom and poor heat transfer to solvent. Higher heparin concentrations disperse the MB-heparin aggregate because of the electrostatic repulsion between heparin chains—this forms MB-self aggregates. PBS can disassociate the MB self-aggregates into dimers because of the ionic shielding of chloride ions. Decomposition analysis indicated that the stable binding sites were the sulfate groups and the glucosamine groups of the heparin. The addition of heparin to MB increases the frequency of MB dimer formation. A significant portion of dimers had an orientation suggestive of π-π stacking. These trends confirmed our experimental observation that MB neutralized by heparin tended to aggregate via π-π stacking.

Chapter 3, in full, is a reprint of the material as it appears in *Bioconjugate Chemistry*, 2018, 29 (11), 3768–3775. Junxin Wang, Ananthakrishnan Soundaram Jeevarathinam, Kathryn Humphries, Anamik Jhunjhunwala, Fang Chen, Ali Hariri, Bill R Miller III, Jesse V Jokerst. The dissertation author was the primary investigator and author of this paper.

Chapter 4 A cellulose-based Photoacoustic Sensor to Measure Heparin Concentration and Activity in Human Blood Samples

In this work, we describe a cellulose-based photoacoustic sensor for heparin. The sensors have a turnaround time of 6 minutes for whole blood samples and 3 minutes for plasma samples regardless of heparin concentration. These sensors have a limit of detection of 0.28 U/ml heparin in human plasma and 0.29 U/ml in whole blood with a linear response (Pearson's r = 0.99) from 0 – 2 U/ml heparin in plasma and blood samples. The relative standard deviation was <12.5% in plasma and < 17.5% in whole blood. This approach was validated with heparin-spiked whole human blood and had a linear correlation with the activated partial thromboplastin time (aPTT) (r = 0.99). We then studied 16 sets of clinical samples—these had a linear correlation with the activated clotting time (ACT) (Pearson's r = 0.86, P<0.0001). The photoacoustic signal was also validated against the cumulative heparin dose (Pearson's r = 0.80, P<0.0001). In addition, we fabricated cellulose films by electrospinning cellulose acetate and subsequently hydrolysis. The film treated with Nile blue A had 59% higher photoacoustic intensity in the presence of 5 U/mL heparin than PBS. It also has strong correlation to the heparin concentration (R^2>0.97). This approach could have applications in bed-side heparin assays for continuous heparin monitoring.

4.1 Introduction

We recently reported a photoacoustic technique for heparin sensing in whole human blood using methylene blue.[100] Photoacoustic imaging is a hybrid optical/acoustic technique that uses the pressure waves generated from thermal expansion after optical absorption. It combines the good temporal and spatial resolution of ultrasound with the contrast of optical imaging.[118-124] We now extend this basic discovery to a more usable sensor based on cellulose. Indeed, paper-based point-of-care diagnostic tools are very attractive because of their rugged nature and low cost.[125] The devices are cost effective and easily fabricated into different modalities with microchannels and adjoining zones.[125] Paper-based substrates are compatible with a wide variety of analytical techniques. The low cost of paper-based sensors makes it easy to do replicate testing.[126]

Here, we describe a polyethylene glycol (PEG)-impregnated, Nile blue A-infused, paper-based photoacoustic sensor for directly assaying heparin. This sensor uses fingerprick-sized samples of blood at the point-of-care. The paper-based sensors are physically stable during the analysis and offer a robust platform for bedside heparin assays in whole human blood. Our initial work in photoacoustic-based heparin sensing added methylene blue and heparin to the whole blood of healthy human donors.[127] This work then described a heparin-sensitive intravenous catheter and tested it with different heparin concentrations in buffer. We now expand this work to include a point-of-care paper-based sensing approach and validated it with 16 human subjects (with ~ 4 different heparin concentrations per patient). Additionally, we customized the fabrication protocol of the cellulose sensor such that it can become a coating on the infuse-catheter. These sensors may have utility as a point-of-care technique—especially when combined with low-cost single element transducers and LED excitation sources[128],[94].

Heparin is a polysulfated glycosaminoglycan (**Figure 4.1A**) with a net negative charge that can interact with cationic dyes such as Nile blue A (**Figure 4.1B**) leading to a spectral change (**Figure 4.1C** and **Supplementary Figure 3.2**). We created a cellulose-based photoacoustic heparin sensor by loading Nile blue A onto polyethylene glycol (PEG) modified Whatman filter paper substrates (**Supplementary Figure 3.3**). The sensors showed just 13.4% leaching in PBS media over a period of 3 h. The PEG and dye content of these sensors were first optimized (**Supplementary Figure 3.2**). We then evaluated the intra- and inter-assay reproducibility and limit of detection in buffer, plasma, and whole blood. Finally, we compared this method to the aPTT and ACT in whole blood samples from healthy donors and in clinical samples.

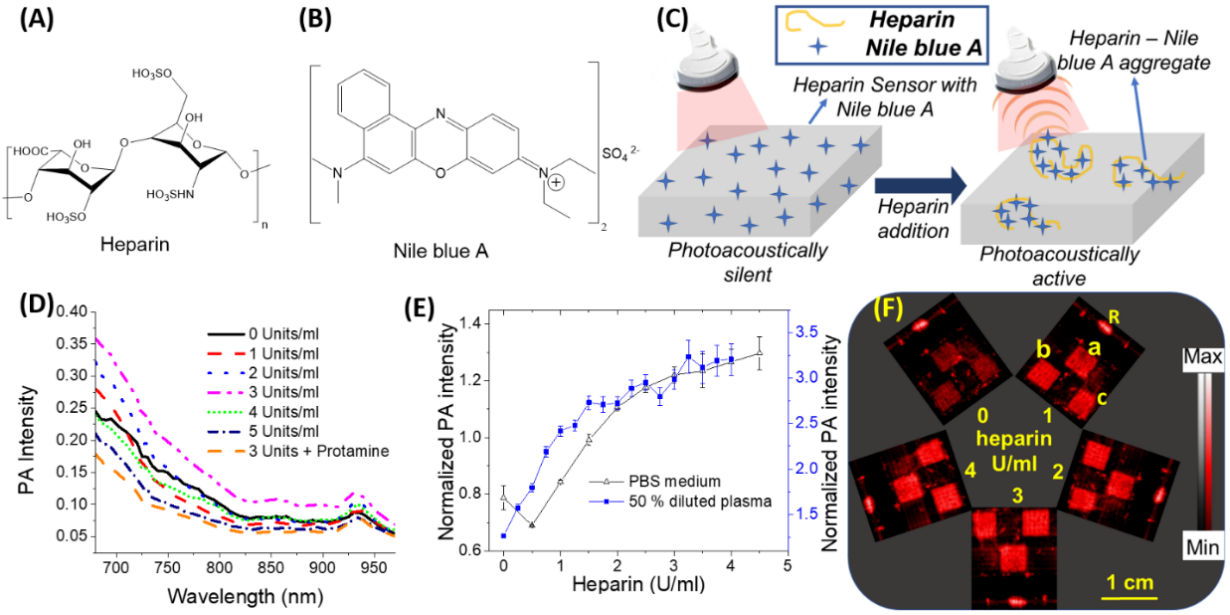

Figure 4. 1 Spectral and photoacoustic study of Nile blue A and cellulose based sensor in PBS and 50% diluted human plasma. (A) Chemical structure of heparin. (B) Chemical structure of Nile blue A. (C) A schematic illustration of sensing mechanism of the sensors. Cationic dyes like Nile blue A form aggregates with heparin. The heparin-Nile blue A aggregates are much more photoacoustically active compared to non-aggregated Nile blue A molecules leading to an increased photoacoustic signal. (D) Photoacoustic spectrum of Nile blue A in aqueous solutions with different amounts of heparin. The maximum photoacoustic signal for Nile blue A was observed at 680 nm and hence 680 nm excitation was used throughout this study. (E) A plot of the ratio of average photoacoustic intensity of three sensors treated with increasing heparin concentrations normalized to the reference line (that does not change with heparin concentration) as a function of heparin concentration in PBS and 50% diluted plasma. (F) Photoacoustic image of three sensors (0.5 x 0.5 cm area) simultaneously treated with different heparin doses in 50% diluted pooled human plasma. The sensors labeled as a, b, and c are replicates with identical composition, and R is the reference line whose intensity remained constant regardless of heparin. The relative standard deviation for the diluted plasma assay is < 6.1%; the detection limit was 0.02 U/ml heparin in 50% diluted pooled human plasma. Error bars indicate the standard error of the three measurements.

4.2 Characterization of Cellulose-based Heparin Sensor in Phosphate Buffer Saline and Diluted Human Plasma

The cellulose-based heparin sensors can respond to heparin via the formation of heparin-Nile blue A aggregates due to electrostatic interaction. The heparin-dye aggregates have a higher photoacoustic activity due to decreased fluorescence, reduced degrees of freedom, and poor heat transfer to the solvent.[129] This change in photoacoustic signal is directly proportional to the amount of heparin in the medium. First, we studied the photoacoustic response of Nile blue A in aqueous solution (**Figure 4.1D** and **Supplementary Figure 3.2**). Next, we studied the photoacoustic signal changes in the cellulose-based heparin sensors due to heparin in PBS (**Figure** 4.**1E**). The LoD in PBS is 1.2 U/ml. There was a surprising small decrease in signal at 0.5 U/mL heparin. When the cellulose sensors were immersed in PBS medium at room temperature for a minimum of minimum of 10 minutes before the study, the decrease was not observed (**Supplementary Figure 3.4**). The initial decrease is likely due to the initial hydration of the substrate with Nile blue A that is insoluble in PBS medium. The wettability of the paper-based sensors has been shown to have a strong correlation to response time.[130]

This experiment was repeated with 50% human plasma—raw photoacoustic images are presented in **Figure 4.1E**. The initial decrease in photoacoustic intensity at 0.5 U/ml heparin was not observed (**Figure 4.1F**). The slope in 50% plasma is 53% higher than PBS. The linear correlation of photoacoustic response of sensors was observed between 0 and 2.0 U/ml heparin ($r > 0.97$) in both PBS and diluted plasma. The limit of detection in 50% plasma was 0.02 U/ml, which is well below the therapeutic heparin levels for different clinical procedures such as thromboembolism (7-8 U/ml), acute myocardial infraction (2.5 U/ml), coronary angioplasty (2.0 U/ml), cardiopulmonary bypass (5.6 U/ml), and extracorporeal membrane oxygenation (0.5 U/ml).[100] Thus, the utility of this sensor is optimized in the therapeutic range of clinical heparin concentrations. The baseline photoacoustic signal of sensors with the same dimensions differed by 1.5%. The intraassay relative standard deviation in 50% diluted plasma was <6.1%.

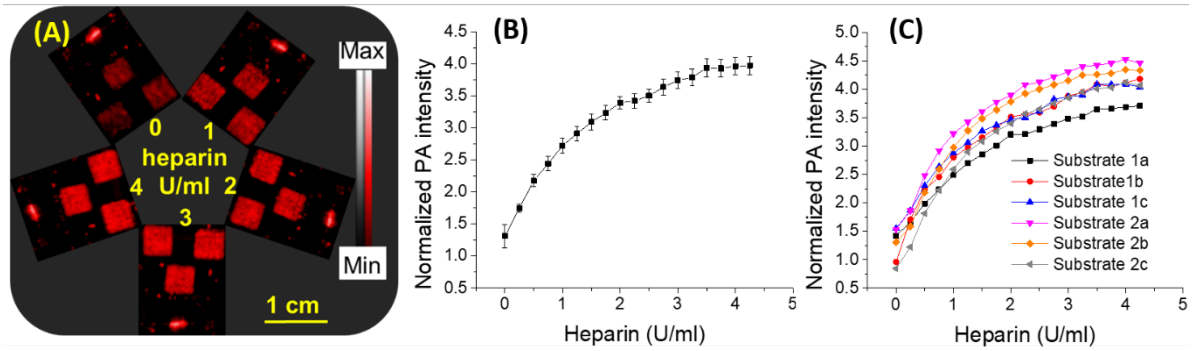

Figure 4. 2 Photoacoustic response of heparin sensor in undiluted human plasma. (A) Photoacoustic image of three square-shaped sensors and reference graphite mark. The same set of sensors were subjected to different doses of heparin and imaged after each dose adjustment. (B) Plot of average normalized photoacoustic intensity of three sensors found in panel (A) versus heparin dose in human plasma. (C) Comparison of heparin response curves collected from two separate sets of experiments where 1a, 1b, and 1c represent results from independent experiment trial 1; 2a, 2b, and 2c are a second independent trial (a, b, and c are the different sensors; see **Supplementary Figure 3**). The results show that photoacoustic response of these sensor to heparin dose is very reproducible. Both the intraassay relative standard deviation and inter-assay relative standard deviation were <8.5%. The detection limit is 0.28 U/ml heparin in pooled human plasma. (0-2.0 U/ml). Error bars indicate the standard error corresponding to three measurements.

4.3 Sensing Efficacy in Normal Pooled Human Plasma and Whole Human Blood

Next, we tested the sensor from 0 – 4 U/mL heparin with whole plasma (**Figure 4.2A**). **Figure 4.2A** shows the sensors repeatedly imaged after each addition. The limit of detection in undiluted plasma is 0.28 U/ml with a relative standard deviation <8.2% (**Figure 4.2B**). This trend in photoacoustic response of sensors and signal contrast with low error was also reproducible between independent experiments (**Figure 4.2C**). Thus, the heparin sensors exhibit a high intra- and inter-assay reproducibility in plasma with a maximum inter-assay relative standard deviation of 8.4%.

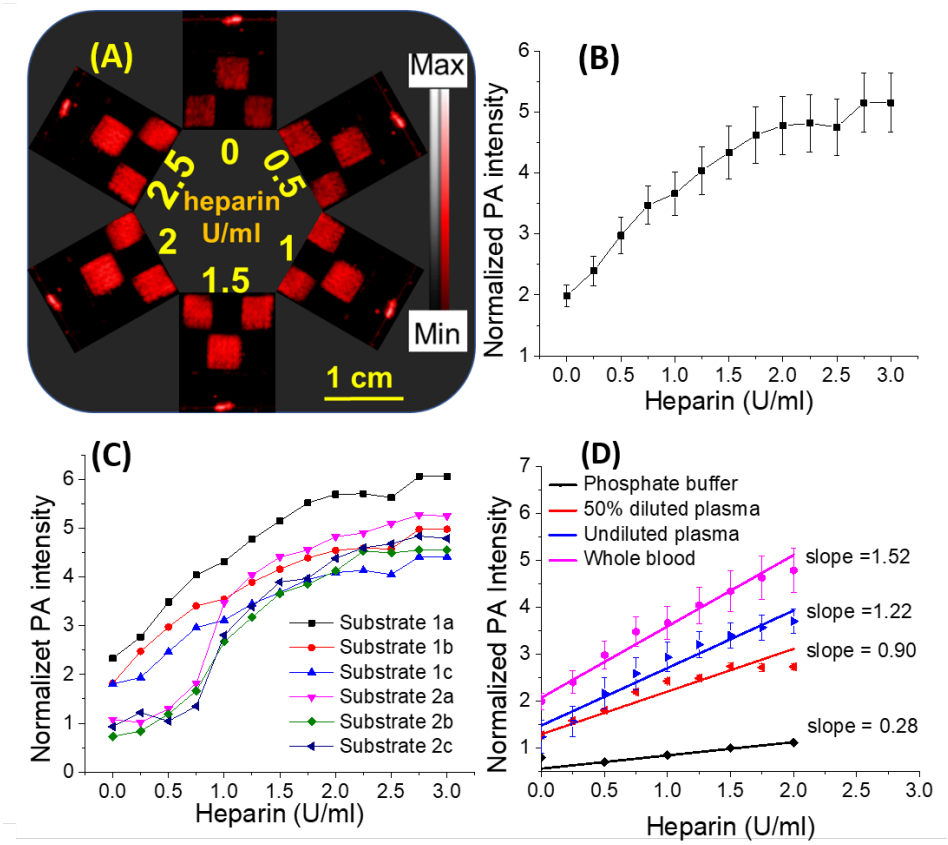

Figure 4. 3 Sensitivity of cellulose-based heparin sensor to different heparin doses in whole human blood. The photoacoustic response of sensors was measured after immersing the sensor into whole human blood. Blood samples were collected from a single healthy donor and spiked with heparin. The sensors were dipped in this blood for one minute before being rinsed and imaged. (A) Representative photoacoustic images of the sensors (squares)—the photoacoustic response of the sensors increased with increasing amounts of heparin. The image represents the same set of sensors after sequential treatment with increasing amounts of heparin in whole blood. (B) Plot of normalized signal versus heparin in whole blood. The intra-assay reproducibility of these measurements is less than 17.5%. (C) Plot of normalized photoacoustic data for all sensors. This data shows the inter-assay reproducibility of photoacoustic response in blood—differences were less than 17.4%. Panel (D) shows the photoacoustic response of sensors to different sample matrices. The slope (sensitivity) was highest in whole blood followed by plasma and PBS. Error bars indicate the standard error of the three measurements.

Finally, we used whole blood (**Figure 4.3**), which can be a challenge due to an increased number of interferences.[101, 131] Electrochemical techniques for direct heparin assaying in blood have been demonstrated but suffer from problems in reproducibility and irreversible binding.[132] **Figure 4.3A** contains raw imaging data from 0-2.5 U/mL (note that not all of the raw images are shown; **Figure 4.3B** has more data points). The assay was linear from 0 to 2.0 U/mL (Pearson's r = 0.98) (**Figure 4.3B**). Values above 2.0 U/mL had a plateau effect likely due to saturation of

surface-bound Nile blue A dye; fortunately, the linear dynamic range corresponds nicely to the clinically relevant range of 0.5 to 2.0 U/mL.

The limit of detection in whole human blood was 0.28 U/ml. The relative standard deviations in this range were < 17.5% (**Figure 4.3C**). Error sources include background photoacoustic signal from hemoglobin and deoxyhemoglobin due to incomplete rinsing in between different heparin concentrations (note that same sensors were repeatedly imaged after treatment with higher heparin concentration).[133] Finally, we compared the slope of the photoacoustic response in these various sample matrices—the slope (sensitivity) was highest in whole blood followed by plasma and PBS (**Figure 4.3D**). The baseline signal of cellulose sensors was highest for whole blood followed by plasma, 50% diluted plasma, and PBS. We attribute the higher photoacoustic background in blood to the presence of red blood cells. The higher background in plasma and diluted plasma might be due to the affinity of the cationic dyes to plasma constituents.[134, 135] The response was 1.2-fold higher in whole blood samples than plasma; pure plasma was 1.4-fold higher than the response in diluted plasma. The sensitivity in whole blood was ~5-fold higher than in PBS. We attribute this change to interaction of heparin with plasma proteins [136], which increases the affinity of the heparin-protein complex to Nile blue A and stabilizes the heparin/dye complex.[137]

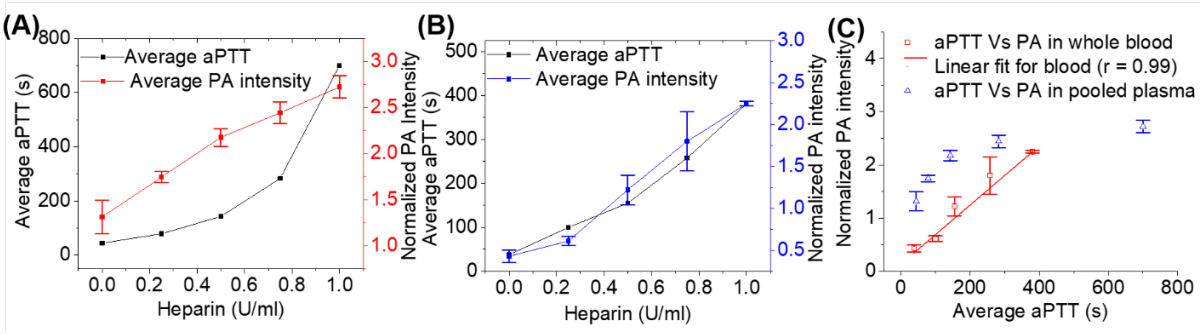

Figure 4. 4 Correlation of aPTT and photoacoustic response of cellulose-based heparin sensor in plasma and whole blood. Panel (A) is the average normalized photoacoustic intensity of sensors from 0 to 1 U/ml heparin in plasma; the corresponding aPTT values were plotted against heparin concentrations in pooled plasma. The photoacoustic response was linear between 0 to 1.0 U/ml while aPTT values clearly deviated from linearity. Panel (B) shows the same experiment using whole human blood collected from a healthy donor. Panel (C) presents the linear correlation between the photoacoustic response of the sensor and aPTT values in pooled human plasma (Pearson's r = 0.86) and in whole human blood samples (Pearson's = 0.99).

4.4 Correlation of Photoacoustic Response of Sensors with aPTT

Finally, we compared the photoacoustic signal to aPTT values (**Figure 4.4A**). **Figure 4.4** compares the photoacoustic response to the aPTT of pooled human plasma (**Figure 4.4A**) and plasma from freshly collected whole human blood (**Figure 4.4B**). The aPTT values in commercial pooled human plasma (black data; **Figure 4.4A**) were less linear (Pearson's r = 0.89) as a function of heparin concentration than the response of the photoacoustic sensor to heparin concentration (red data; **Figure 4.4A**) (Pearson's r = 0.99). A plot of photoacoustic response versus aPTT values for the commercial pooled plasma showed a lower linear correlation (r= 0.86) compared to fresh human blood (Pearson's r =0.99) (Fig **4.4C**). This is likely because the whole blood sample was fresh, but the plasma had been previously frozen—freezing can dysregulate clotting factors.[138] Regardless, these results suggest that the photoacoustic signal can monitor heparin activity analogously to the aPTT.

4.5 Heparin Sensing in Banked Clinical Plasma Specimens

Finally, we analyzed banked (at -80 °C storage) plasma samples collected from 16 patients undergoing ablation in the electrophysiology lab (3 to 10 samples per patient; 78 total samples; Table S3.1). We plotted the first four samples for each subject because that is the region where the heparin dose is changing the most rapidly and where anticoagulant activity must be most carefully monitored (n=60 samples). Supplementary Figure 5A plots the photoacoustic response versus the ACT values with a Pearson's r = 0.76 (P<0.0001).

We binned the photoacoustic response as a function of cumulative heparin dose and ACT (**Figure 4.5A**)—the ACT values measured over all sample sets were compiled into 20-s bins. We then averaged the photoacoustic intensity within each of these bins and plotted against the averaged ACT values (**Figure 4.5A**). The average photoacoustic intensity had a linear correlation against average ACT (Pearson's r = 0.86); 62.5% of the measured photoacoustic intensity values were within the 95% CI band (**Figure 4.5A**). The change in photoacoustic intensity with respect to the ACT values are significant (P < 0.0001). This binning was used to reduce inherent errors

associated with the measurements. Variations in ACT include different baseline ACT values, choice of activator, presence of drugs such as aprotinin, and the instrument used.[139] Error sources associated with photoacoustic data include the variation in the size of the sensors and variation in dye distribution across the sensor area.

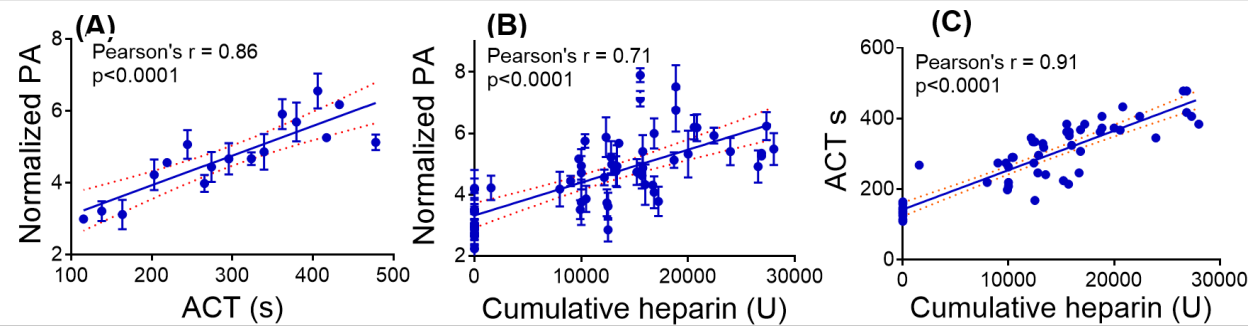

Figure 4. 5 Photoacoustic response of sensors to clinical specimens collected from 16 patients undergoing cardiac procedures requiring heparin. Panel (A) shows the photoacoustic response of sensors versus ACT. Here, the photoacoustic data were binned into 20-second ACT intervals from 109 to 478 s. Panel (B) presents the photoacoustic response as a function of cumulative heparin dose, and panel (C) shows linear correlation between ACT and cumulative heparin dose. The data corresponding to (B) and (C) were not binned. The correlation was linear for all three analyses (Pearson's r > 0.7). The dotted lines represent the 95% confidence interval (CI) band. The P value < 0.0001 indicates that the changes in photoacoustic intensity and ACT values are significantly correlated. Error bars in panels (A) and (B) indicate standard error.

Next, we correlated the photoacoustic response to ACT and cumulative heparin dose. This correlation was linear and significant for both ACT and cumulative heparin dose (**Figure 4.5A** and **B**; P < 0.0001; Pearson's r > 0.7). The aPTT values were all over 500 s and had little utility with these samples.[140] However, this study demonstrated a close correlation between the photoacoustic signal of the heparin sensor and the ACT (r = 0.86; P < 0.0001) suggesting that this approach is not only measuring heparin concentration but also acts as a surrogate for anticoagulant activity.

This approach can quickly measure heparin in small samples (~ 50 µL). Other recently reported dye-based heparin assays are more selective but have not yet been studied in complex biological samples.[141, 142] Colorimetric assays for heparin are either limited to plasma or buffer or have not yet been demonstrated in whole blood.[131, 143, 144] The aPTT is limited by its range of detection, variation in reagents, and instrumentation.[140, 145] The Factor-Xa test is a chromogenic

assay that measures the activity of heparin against activated factor X. However, the anti-Xa test underestimates heparin content in the presence of antithrombin deficiency, post-thrombolysis, hyperbilirubinemia, end stage renal disease, and pregnancy.[146] The ACT is currently used in the operating room as a heparin monitor but has some insensitivities to coagulation abnormalities and platelet deficiencies—having a direct heparin assay could offer insight into the patient's anticoagulation status.[147] The detection limit achieved here (0.28 U/ml in whole human blood samples) is consistent with clinically relevant doses[148] including those needed for thromboembolism (7-8 U/mL)[83], acute myocardial infarction (2.5 U/mL)[84], coronary angioplasty (2 U/mL)[85], and extracorporeal membrane oxygenation (0.5 U/mL)[87].

4.6 Fabrication of Cellulose Film Using Electrospinning

Next, we used electrospinning to fabricate cellulose fiber films, which is easier to be applied on catheters than filter papers. Direct electrospinning of cellulose provides desirable porous structure, but it requires complicated set up. Alternatively, we electrospun cellulose acetate, which was later hydrolyzed to cellulose. The cellulose acetate electrospun on the glass plate or infusion catheter was 2.3 μm thick. (**Figure 4.6A**). Subsequently, the cellulose fiber was fixed with a thin layer of cellulose film using doctor's blade method and then loaded with Nile blue A for heparin sensing. The photoacoustic intensity of the cellulose film treated with the PBS containing 5 U/mL heparin was 59% higher than the baseline (**Figure 4.6B**). Statistical analysis of 3 replicates showed a strong linearity (R^2=0.97) between the photoacoustic enhancement and heparin concentration (**Figure 4.6C**).

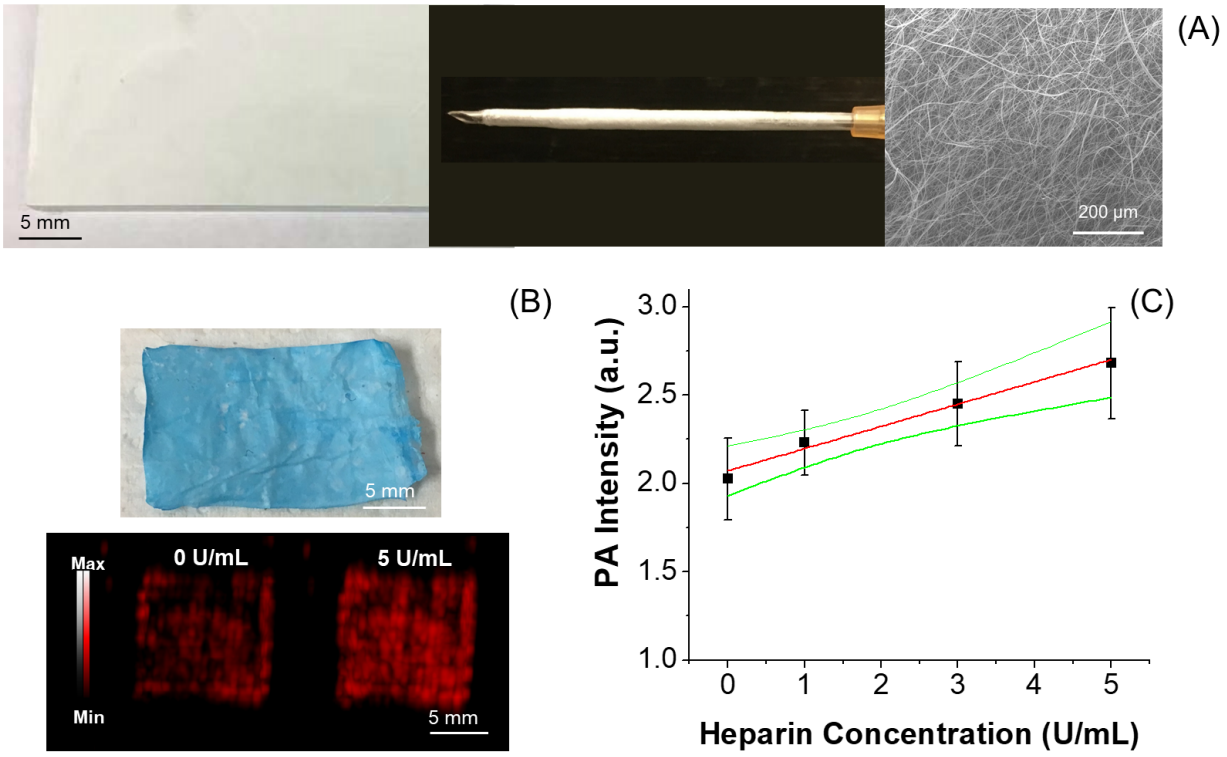

Figure 4. 6 Fabrication of cellulose fiber sensor using electrospinning. Panel A shows the photo of the cellulose acetate fiber electrospun on a fluorine doped tin oxide (FTO) coated glass plate and the surface of the infusion catheter and SEM image of cellulose acetate fiber. Panel B shows the photo of the cellulose fiber embedded within the cellulose film and the photoacoustic enhancement of the film in the presence of 5 U/mL. In panel C, statistical analysis of 3 replicate films shows strong correlation ($R^2 \geq 0.97$) between the photoacoustic intensity and heparin concentration of 3 cellulose sensors. Error bars in panel C represent the standard deviation of 3 replicates.

4.4 Conclusion.

This study described the preparation of a cellulose-based heparin sensor and photoacoustic imaging to measure heparin in blood samples. The correlation with cumulative heparin levels, turnaround time, and sample requirements are comparable to the ACT. Further, the photoacoustic response of heparin sensors in different sample matrix are closely correlated with aPTT and ACT suggesting that this method is monitoring heparin activity—not just concentration. The paper-based heparin sensors are very affordable and can be used as a disposable sensor. Our next steps will optimize this technique into a bedside and/or point-of-care heparin assay. The limitations of the work originate from the fact that it is a direct heparin assay and the anticoagulant activity is a result of heparin-antithrombin complex. However, this study

demonstrated a close correlation to activity-based assay (ACT and aPTT). Future work will translate this technology into an implantable catheter device for real-time *in vivo* monitoring of heparin concentrations.

Chapter 4, in partial, is a reprint of the material as it appears in *Biosensors and Bioelectronics*, 2019, 126, pp 831-837. Ananthakrishnan Soundaram Jeevarathinam, Navin Pai, Kevin Huang, Ali Hariri, Junxin Wang, Yuting Bai, Lu Wang, Tiffany Hancock, Stanley Keys, William Penny, Jesse V Jokerst. The dissertation author was the co-author of this paper.

Chapter 5 Switchable Photoacoustic Intensity of Methylene Blue via Sodium Dodecyl Sulfate Micellization

The interaction between methylene blue (MB) and sodium dodecyl sulfate (SDS) has been widely studied spectroscopically, but details about their interactions remain unclear. Here, we combined photoacoustic (PA) imaging with nanoparticle tracking analysis (NTA) and spectroscopy to further elucidate this interaction. PA imaging of 0.05 mM MB showed a 492-fold increase in intensity upon the addition of 3.47 mM SDS. Higher concentrations above SDS's critical micelle concentration (CMC) at 8.67 mM decreased the PA intensity by 54 times. Relative quantum yield measurements indicated that PA intensity increased as a result of fluorescence quenching. Meanwhile, NTA indicated an increased number of nonmicellar MB/SDS clusters at SDS concentrations below the CMC varying in size from 80 to 400 nm as well as a decreased number above the CMC. This trend suggested that MB/SDS clusters are responsible for the PA intensity enhancement. Comparison of PA intensities and spectral shifts with MB/hexadecyltrimethylammonium bromide, MB/sodium octyl sulfate, and MB/sodium chloride demonstrated that MB was bound to the sulfate moiety of SDS before and after micellization. Our observations suggest that MB forms aggregates with SDS at premicellar concentrations, and the MB aggregates disassociate as monomers that are bound to the sulfate moiety of SDS at micellar concentrations. These findings further clarify the process by which MB and SDS interact and demonstrate the potential for developing MB-/SDS-based contrast agents.

5.1 Introduction

Interactions between sodium dodecyl sulfate (SDS) and cationic dyes—especially MB—have drawn much attention because they present unique spectral profiles with peak shifts between SDS at premicellar and micellar concentrations[149-151]. MB monomers exhibit a characteristic absorbance peak near 660 nm, but the addition of SDS at pre-micellar concentrations (< 8 mM) disrupts Beer's law and blue shifts the peak to 610 nm[152]. This hypsochromic shift is attributed to the formation of H-type dimers resulting from neutralization by SDS and π-π stacking between MB monomers[153]. Exciton theory suggests that the coupling between MB monomers splits the single excited state into two exciton states, and the energy absorption between the ground state and upper exciton state causes a hypsochromic shift in the absorbance spectrum[154-156].

In addition to spectral data, Carroll *et al*. and Morgounova *et al.* detected increased scattering signal[150] and decreased triplet transient absorption at 660 nm[110] of MB in SDS at premicellar concentrations, respectively. This suggested the presence of MB-SDS clusters. However, the exact nature of the MB-SDS interaction remains unclear including the binding site between SDS and MB. Numerous intermolecular forces besides the electrostatic force affect this interaction, and MB might bind to the hydrophobic tail of SDS due to hydrophobic attraction[110]. Previous research has suggested that when the SDS concentration exceeds the critical micelle concentration (CMC), MB dimers disassociate into monomers as indicated by the increase of the primary monomer absorbance peak at 660 nm[110, 150, 153]. However, the nature of this supposition has not been investigated or verified beyond absorption spectroscopy, and the mechanism of the dimer to monomer transition at the CMC is unknown.

This communication clarifies the unique dynamic behaviors between MB and SDS by studying the PA intensity, aggregate concentration, and spectral profiles of MB upon addition of increasing SDS, hexadecyltrimethylammonium bromide (CTAB), sodium octyl sulfate (SOS), and sodium chloride (NaCl).

Results and Discussion

The chemical structures of the molecules used here are shown in **Figure 5.1A**. We measured the switchable PA intensity of MB upon addition of SDS, and the PA intensity was strongly correlated to the hypsochromic shift in its absorbance spectrum and the number of MB-SDS aggregates in solution. The binding site of the MB monomers at premicellar concentration was then determined by control experiments using CTAB and SOS. The addition of NaCl at high concentration (i.e. 0.8 mM) in MB and SDS at micellar concentrations then confirmed the binding between the MB monomer and the SDS. Finally, we present a scheme of the MB/SDS complex at premicellar and micellar concentrations.

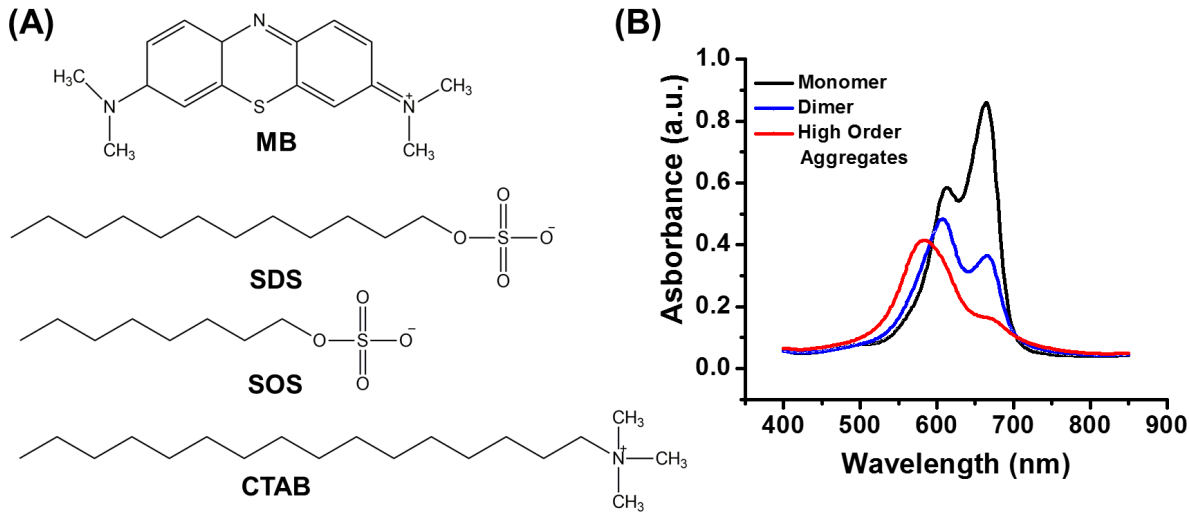

Figure 5. 1 Chemical structures of chemicals used in the experiment and absorbance spectra of MB at different orders of aggregate. Panel A shows the chemical structure of MB, SDS, SOS, and CTAB. Panel B shows the spectral profile of MB monomer (black), MB dimer (blue), and MB high order aggregates (red) prepared by adding increasing concentrations of sodium sulfate. The absorbance peak of MB monomer, dimer, and higher order aggregates occurs at 660, 610, and 580 nm, respectively.

5.2 SDS Concentration Dependent Photoacoustic Intensity

For reference spectra, we locked the MB into three different conformations with sodium sulfate: monomer, dimer, and aggregate[157] (**Figure 5.1B**). We then studied the MB PA intensity as a function of SDS concentration below the CMC (~8 mM[158]). There was an increase in signal and then a rapid reverse at and above the SDS CMC. Here, the MB concentration was held at

0.05 mM to optimize its baseline PA intensity and maintain it in a majority of monomeric form (**Figure 5.1B**); MB starts to dimerize at 10^{-7} M)[106, 108].

The addition of 3.47 mM SDS increased the PA intensity of pure MB by 492-fold (**Figure 5.2A**), and statistical analysis indicated a strong correlation between the PA intensity and the concentration of SDS (linear regression R^2>0.99) from 0.87 to 3.47 mM (**Figure 5.2B**). However, the PA intensity of MB-SDS solutions decreased significantly as the SDS concentration exceeded the CMC of SDS. The PA intensity at SDS concentrations of 8.7 mM was 54 times lower than at 3.47 mM SDS (near baseline). These changes are likely caused by the aggregation of MB because the increase and reversal of PA intensity was also accompanied by a distinct color change (**Figure 5.2C** inset) indicating a transition between MB monomers and dimers. The peak absorbance of MB blue-shifted from 660 to 610 nm at 3.47 mM SDS and returned to 660 nm when the SDS concentration was above the CMC (**Figure 5.2C**). We hypothesize that the hypsochromic shift and its reversal correspond to the formation and dissociation of electrostatically formed aggregates of MB and SDS rather than H-type dimers formed by ionic MB monomers.

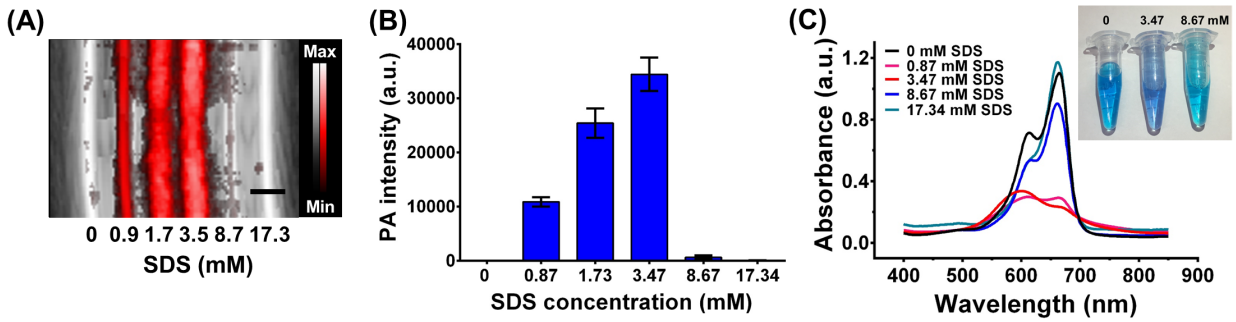

Figure 5. 2 Photoacoustic and spectroscopic changes of MB upon SDS addition. Panel A shows the combined PA/ultrasound image of tubes filled with 0.05 mM MB and increasing SDS concentration from 0.9 to 17.3 mM. The image is a maximum projection intensity of the overlay of ultrasound (black to white) and PA (red to white) signals (scale bar = 2 mm). The intensities were quantified in panel B. Statistical analysis showed a linear response from 0 to 3.47 mM SDS (R^2 > 0.99) with 492-fold increase at 3.47 mM SDS. The PA intensity then decreased 54-fold at 8.67 mM. The trend of PA intensity corresponds closely to the spectral shift shown in panel C. The absorbance peak of pure MB blue shifts from 660 to 610 nm at premicellar concentrations, suggesting the formation of MB-SDS aggregates. The shift reverses to 660 nm at the SDS concentration of 8.67 mM, a micellar concentration. Error bars in panel B denote standard deviation. The inset in panel C shows the color change and reversion of MB solution as SDS concentration approaches and surpasses the CMC.

5.3 MB Forms Aggregates with SDS at Premicellar Concentrations

To verify the presence of aggregates, we used nanoparticle tracking analysis (NTA) to measure the size distribution and concentration of potential aggregates in MB-SDS solutions (**Figure 5.2A**). We found that SDS at 3.47 mM with 0.05 mM MB formed 2,320-times more aggregates (inset of **Figure 5.2A**) than pure MB with an average size of 285.7 ± 5.1 nm (**Supplementary Figure 4.1**). This number decreased 82 times when SDS was increased to 8.67 mM (above the CMC). The decreased concentration could be attributed to the disassociation of MB-SDS clusters to micelles (~1.8 nm[159]) that were smaller than the detection limit of NTA (10 nm). Additionally, the concentration of aggregates was dependent on the concentration of MB. The concentration of aggregates decreased 84-fold when the MB concentration was reduced from 0.05 to 0.00625 mM (**Supplementary Figure 4.2A**). This decrease further demonstrated that MB formed the aggregates with SDS.

More interestingly, the increase of PA intensity was specific to the addition of SDS rather than dimerization of MB. We increased the concentration of MB from 0.05 mM to 2 mM so that it formed mostly dimers (0 mM SDS in **Figure 5.3B**). Here, 1.73 mM SDS decreased the magnitude of absorbance at 610 nm by 1.6 folds (**Figure 5.3B**), but it increased the photoacoustic intensity by 12-fold (**Figure 5.3C**). This decreased absorbance intensity indicates that the MB-SDS ionic pairs in the aggregates have a lower extinction coefficient than self-aggregated MB H-type dimers because the formation of H-type MB dimers increase the MB monomer's absorbance at 610 nm (**Supplementary Figure 4.2B**). The PA intensity decreased to a value slightly higher (1.58 times) than pure MB when the SDS concentration increased above the CMC at 8.67 mM. This indicated disassociation of the MB-SDS aggregates into MB dimers. The aggregation of MB dimers with SDS that had lower absorbance than ionic MB dimers verified that MB formed ionic pairs with SDS in aggregates rather than H-type dimers formed by ionic MB monomers.

5.4 Control Experiment with Alternative Surfactants.

Next, we used alternative surfactants to determine where MB interacts with SDS: the sulfate moiety or the hydrophobic tail. We substituted SDS with CTAB—a molecule similar in structure to SDS but with a cationic ammonium group rather than the anionic sulfate of SDS. The addition of 0.25 mM CTAB decreased the PA intensity of 0.05 mM MB by 3-fold, and the PA intensity remained low when CTAB concentration surpassed its CMC (0.9 mM[160]) to 3 mM (**Figure 5.3D**). The reduced absorbance (**Figure 5.3E**) and PA intensity indicated that CTAB further repulsed the MB monomers suggesting that electrostatic forces govern the interaction between MB and charged surfactants.

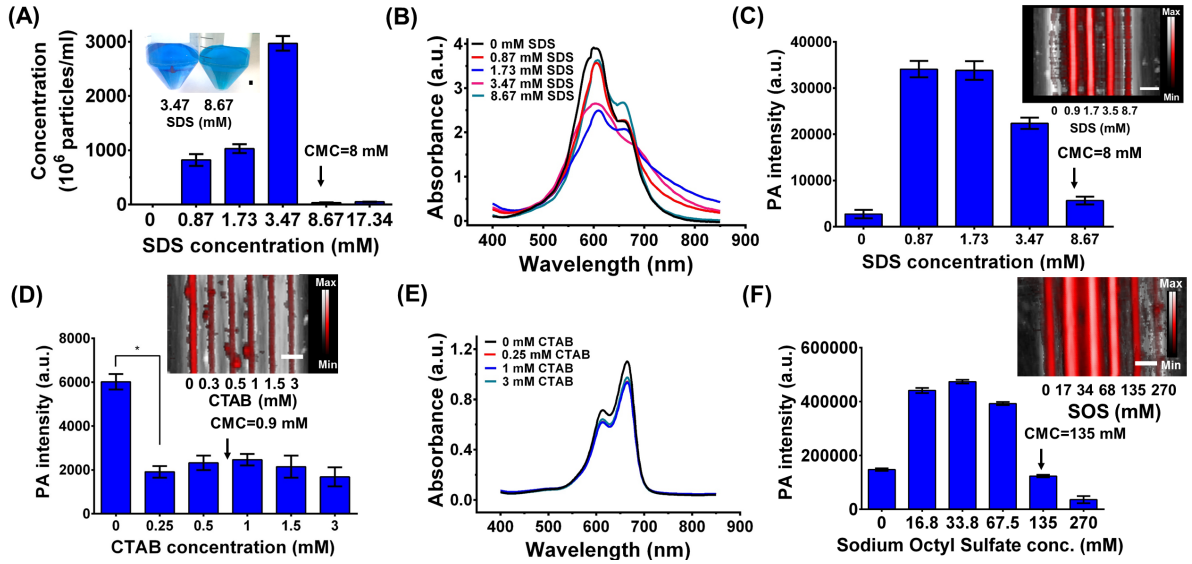

Figure 5. 3 Investigation of MB-SDS aggregates and the binding between MB and SDS using 2 mM MB (dimer-promoting), CTAB, and SOS. Panel A shows that the concentration of MB-SDS aggregates increased from 1.28×10^6 to 2.97×10^9 particles/mL upon the addition of 3.47 mM SDS. The concentration decreased to 3.64×10^7 particles/mL when SDS concentration was further increased to 8.68 mM because the MB-SDS aggregates disassociated to MB-SDS micelles that were too small to be detected. Panel B shows the absorbance spectra of 2 mM MB with increasing SDS concentration from 0.9 to 8.7 mM. The peak absorbance of pure MB (black line) at 610 nm indicates the strong presence of MB dimers. The inset in panel C is the photoacoustic image of samples in panel B and panel C quantifies the PA intensities of the same solutions. Statistical analysis shows a 12-fold increase of MB upon 1.73 mM SDS addition. The PA signal begins to decrease at 3.47 mM SDS and eventually to a value like pure MB at 8.67 mM. Panel D shows the quantified PA intensity with PA/ultrasound image (inset) of 0.05 mM MB with 0, 0.25, 0.50, 1.00, 1.50, and 3.00 mM CTAB, respectively. While additional 0.25 mM CTAB decreased the PA intensity of MB by 3-fold, no hypsochromic shift like the addition of SDS was observed in the absorbance spectra (panel E). Panel F quantifies the PA image (inset) of 0.05 mM MB with increasing SOS from 0 to 270 mM. The PA intensity of MB increased 3.2 times with the addition of 33.8 mM SOS and reversed to a value 0.84 times lower than the pure MB at 135 mM (the CMC of SOS). Error bars and scale bar in panel A, C, D, and F represent standard deviation and 2 mm, respectively.

Next, we studied SOS, which has the same structure to SDS but 4 fewer carbons. SOS increased the PA intensity of 0.05 mM MB by 3.2 times at 33.8 mM, after which the intensity decreased. At the SOS CMC of 135 mM the PA intensity decreased to a value slightly lower (0.84 times) than the baseline of pure MB (**Figure 5.3F**). The PA intensity would be higher at a 135 mM if the MB interacted with SDS at a location between the SDS's head and tail because the MB monomer would be closer to enhance PA intensity. These controls suggest that MB interacts with SDS at the sulfate moiety instead of the hydrophobic tail.

5.5 MB Attaches to SDS after Micellization

At SDS concentrations above the CMC, the reversal of the hypsochromic shift in the absorbance spectra and reduction in PA intensity suggests the disassociation of MB-SDS aggregates, yet the precise form of the resultant MB molecules remained unknown. We investigated this question by adding NaCl to MB-SDS solutions to examine whether the MB became ionic in solution or was bound specifically to the sulfate moiety. NaCl at a high concentration (e.g. 0.8 M) forms MB dimers[161]. In our experiments, it decreased the absorbance at 660 nm (MB+NaCl in **Figure 5.4A**). As a result, the remaining MB monomer dimerized and increased the PA intensity (**Figure 5.4B**). In contrast, additional NaCl in the MB with 8.7 mM SDS did not induce a peak shift or decrease in the absorbance spectrum (MB+SDS+NaCl in **Figure 5.4A**), although the PA intensity was increased by 59%. This indicated that the resulting MB monomers disassociated from the MB-SDS aggregates were specifically bound to the sulfate moiety of SDS rather than free ions in solution.

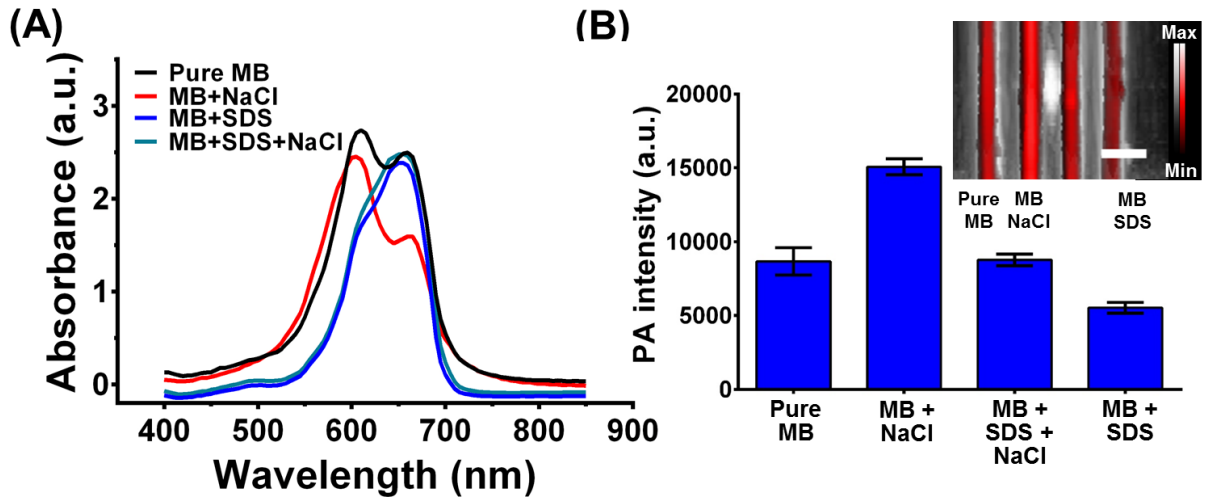

Figure 5. 4 Mechanistic determination of the MB-SDS interaction at micellar concentrations using NaCl. Panel A shows the effect of 0.8 M NaCl in 2 mM MB with and without 8.67 mM SDS. The peak absorbance at 610 nm indicates that pure MB monomers form dimers at 2 mM. The addition of NaCl significantly reduces the monomer peak at 660 nm implying that more dimers form. The peak absorbance of MB red shifts to 660 nm in the presence of 8.67 mM SDS, and the addition of NaCl does not induce a hypsochromic shift. The corresponding PA image of the samples in panel B shows that the additional NaCl increases the PA intensity of MB by 1.7-fold without SDS and 0.59-fold with 8.67 mM SDS. This suggests that MB binds to SDS at micellar concentration. Scale bars and error bars in panels B denote 2 mm and standard deviation, respectively.

Based on the overall observations, we propose a mechanism for the interaction between MB and SDS in **Figures 5.5**. MB forms aggregates or ionic pairs with SDS at premicellar concentrations. The SDS brings MB monomers closer together allowing the formation of MB dimers due to π-π stacking (**Figure 5.5B**). However, when the SDS concentration is increased above the CMC, SDS molecules form micelles and separate individual MB monomers, overcoming the aromatic force between MB monomers. These MB monomers are bound to the sulfate moieties that form the perimeter of SDS micelles (**Figure 5.5C**).

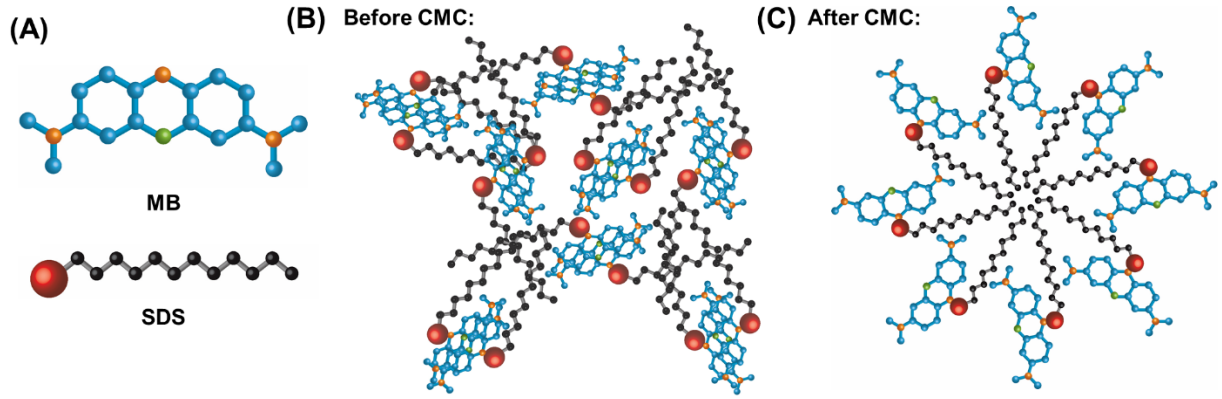

Figure 5. 5 Interaction scheme between MB and SDS at premicellar and micellar concentrations. Panel A shows the chemical structure of MB and SDS. MB is blue, and the SDS has red hydrophilic head and black hydrophobic tail. Panel B illustrates potential forms of MB-SDS aggregates at premicellar concentrations. When SDS forms micelles (panel C), MB dimer disassociates, leaving MB monomers bound to the sulfate moieties of SDS micelles.

5.6 Conclusion

A photoacoustic, spectroscopic, and nanoparticle tracking study was conducted to elucidate the interactions between MB and SDS. At premicellar concentrations, MB forms aggregates with SDS promoting dimerization. At the CMC and above, SDS disassociates the MB aggregates. The resulting MB monomers bind to the sulfate moieties of SDS micelles.

Chapter 5, in full, is a reprint of the material as it appears in *Langmuir*, 2018, 34 (1), pp 359–365. Junxin Wang, Ching-Yu Lin, Colman Moore, Anamik Jhunjhunwala, Jesse V Jokerst. The dissertation author was the primary investigator and author of this paper.

Chapter 6 Copper Sulfide Nanodisks and Nanoprisms for Photoacoustic Ovarian Tumor Imaging

Transvaginal ultrasound is widely used for ovarian cancer screening but has a high false positive rate. Photoacoustic imaging provides additional optical contrast to supplement ultrasound and might be able to improve the accuracy of screening. Here, we report two copper sulfide (CuS) nanoparticles types (nanodisks and triangular nanoprisms) as the photoacoustic contrast agents for imaging ovarian cancer. Both CuS nanoprisms and nanodisks were ~6 nm thick and ~26 nm wide and were coated with poly(ethylene glycol) to make them colloidally stable in phosphate buffered saline (PBS) for at least 2 weeks. The CuS nanodisks and nanoprisms revealed strong localized surface plasmon resonances with peak maxima at 1145 nm and 1098 nm, respectively. Both nanoparticles types had strong and stable photoacoustic intensity with detection limits below 120 pM. The circular CuS nanodisk remained in the circulation of nude mice (n=4) and xenograft 2008 ovarian tumors (n=4) 17.9-fold and 1.8-fold more than the triangular nanoprisms, respectively. Finally, the photoacoustic intensity of the tumors from the mice (n=3) treated with CuS nanodisks was 3.0-fold higher than the baseline. The tumors treated with nanodisks had a characteristic peak at 920 nm in the spectrum to potentially differentiate the tumor from adjacent tissues.

6.1 Introduction

Recent studies have demonstrated the potential of photoacoustic imaging to improve the accuracy of ovarian cancer screening in high risk populations.[162] Ovarian cancer has a poor prognosis with 60% of patients being diagnosed at late stages.[163] Transvaginal ultrasound imaging has been widely used for screening, but its positive-predictive value is only 5.3% suggesting false positives[164]. Thus, several groups have suggested that photoacoustic imaging could improve the value of imaging-based ovarian cancer screening. Zhu *et al.* have been developing photoacoustic imaging to improve the accuracy of ovarian cancer screening via classification algorithms that analyze the difference of photoacoustic spectra, envelopes, and images between benign and malignant ovarian tumors.[14, 165-168] However, *in vivo* photoacoustic imaging studies in ovarian cancer are rare with a clinical sensitivity less than 90%.[166, 169]

Nanoparticle-based photoacoustic contrast agents might further improve the sensitivity and specificity of screening by increasing the tumor signal. Examples include iron/silica/gold core−shell nanoparticles,[170] gold nanorods,[171] and near-infrared dye-labeled magnetic iron oxide nanoparticles.[172] In one example, mice received HER-2/neu targeted magnetic iron oxide nanoparticles had 5-fold higher photoacoustic intensity than mice without injection.[172]

More recently, copper sulfide nanoparticles, nanodisks[173] and nanoprisms[174] were shown to have tunable localized surface plasmon resonances (LSPRs) from 1000 to 1500 nm.[173-175] These wavelengths might facilitate deeper penetration depth (before water absorption increases) or could lead to multiplexed imaging of multiple data channels by expanding the range of usable wavelengths.[176] For example, CuS nanoparticles were imaged at 1064 nm in a rodent brain with intact skull as well as *in vitro* samples under 5 cm of chicken breast tissue.[177] In addition, the geometrics of these nanoparticles might also affect their extravasation in murine tumor models as described previously in comparisons between different nanoparticle shapes[178-181].

For these reasons, we evaluated CuS nanodisks and nanoprisms as photoacoustic contrast agents for ovarian cancer imaging. These materials have nearly identical dimensions,

surface coatings, and surface charges with the exception of their different geometric shapes to test the shape effect of nanoparticle on the extravasation. We then used photoacoustic imaging and inductively coupled plasma mass spectrometry (ICP-MS) to study the photoacoustic properties and extravasation of CuS nanodisks and nanoprisms in xenograft ovarian tumor models. We characterized their photoacoustic intensities, limit of detection, signal stability, and accumulation efficiency in the mice bearing human OV2008 xenograft tumors. The data suggest that the CuS nanodisk are retained longer in the circulation with more accumulation in the tumors.

Results and Discussion

6.2 Synthesis and Characterization of CuS Nanodisks and Nanoprisms

We used a solvent-based method to synthesize the CuS nanodisks and a seed/halide ion-mediated process for the synthesis of CuS nanoprisms (**Figure 6.1A**).[174, 175] The synthesis of CuS nanodisks employed Cu salt and S powder as reactants and oleylamine as a nanocrystal capping agent. The oleylamine activates the S powder precursor by forming oleylammonium hydrosulfide, which reacts with Cu^{2+} ions to precipitate CuS and form the disk-like CuS nanocrystals.[175] Nanoprism synthesis used CuS nanodisks as the seed, where added chloride ions promote the growth of facetted triangular nanoprisms.[174] The chloride ions cooperatively stabilize the low-index CuS surfaces and preferentially enhances the growth in and along a given crystallographic direction during synthesis. By carefully controlling the reaction time and temperature, we synthesized CuS nanodisks and nanoprisms with similar thicknesses and widths.

Figure 6.1B and **6.1C** detail the morphology and size of the CuS nanoparticles. The average thickness of nanodisks and nanoprisms was 6.5 ± 0.7 nm and 6.3 ± 0.8 nm, respectively. TEM measurements indicated that the average diameter of the nanodisks was 25.6 ± 2.5 nm (PDI=0.256, measured by dynamic light scattering (DLS)), and the average edge length of the nanoprism was 26.8 ± 3.3 nm (PDI=0.247). These nanodisks and nanoprisms were colloidally stable without aggregation in chloroform (nanodisk and nanoprism in **Figure 6.1D**), but they precipitated in water because of the hydrophobic oleylamine coating (**Figure 6.1D** inset).

We improved the hydrophilicity by substituting the surface coating with hydrophilic and biocompatible polyethylene glycol (PEG). We incubated the as-made CuS nanoparticles with PEG-thiol (Mw=5000) to form strong Cu-S bonds with the nanoparticles, which replaced the oleylamine. The hydrodynamic radius of the CuS nanodisks and nanoprisms in water increased from 85.3 to 125.4 nm and from 91.9 to 131.7 nm (**Figure 6.1D),** respectively. The water-stable nanoparticles further confirmed the PEGylation on both CuS nanoparticles (**Figure 6.1D** inset). Zeta potential measurements revealed the negative surface charge on these nanoparticles (-10.2 mV for the nanodisk and -10.5 mV for the nanoprism). A time-dependent, hydrodynamic radius measurement of the nanoparticles showed that both CuS nanodisk and nanoprism were stable for at least 2 weeks at room temperature (**Supplementary Figure 5.1**).

We used TGA (**Supplementary Figure 5.2**) and absorbance data (**Supplementary Figure 5.3**) to estimate the number of particles per unit volume. Upon heating (> 400 ^{o}C), 0.172 µL CuS nanodisk colloidal solution resulted in 0.379 mg (bare CuS nanodisk). The molar concentration of the CuS nanodisks can be calculated as following: (1) one nanodisk volume with average diameter of 25.6 nm and thickness of 6.5 nm = $(25.6\ nm/2)^2 \times \pi \times (6.5\ nm)^2 = 3.34 \times 10^3\ nm^3$; (2) weight of one CuS nanodisk = $3.34 \times 10^3\ nm^3 \times 4.76$ g/cm (density of CuS) = 1.59×10^{-17} g; (3) number of CuS nanodisk in the test sample = 3.79×10^{-3} g/1.59×10^{-17} g= 2.38×10^{13}; (4) mole of CuS nanodisk in the test sample = $2.38 \times 10^{13} / 6.02 \times 10^{23}$ (Avogadro's number /mole) = 3.95×10^{-11} mole; (5) concentration of CuS nanodisk in the colloidal solution = 3.95×10^{-11} mole / 0.172×10^{-6} L= 2.30×10^{-7} M. Combined with Beer's law (extinction = molar extinction coefficient x path length x analyte concentration), the molar extinction coefficient can be calculated based on the extinction spectrum of the CuS nanodisk colloidal solution (diluted 200 times relative to the TGA sample). The molar extinction coefficient at 1145 nm = $0.4046 \times 200 / 2 \times 2.30 \times 10^{-7} = 3.52 \times 10^8\ M^{-1}cm^{-1}$, which is ~10 times lower than gold nanorod (2.5 to $5.5 \times 10^9\ M^{-1}cm^{-1}$)[182].

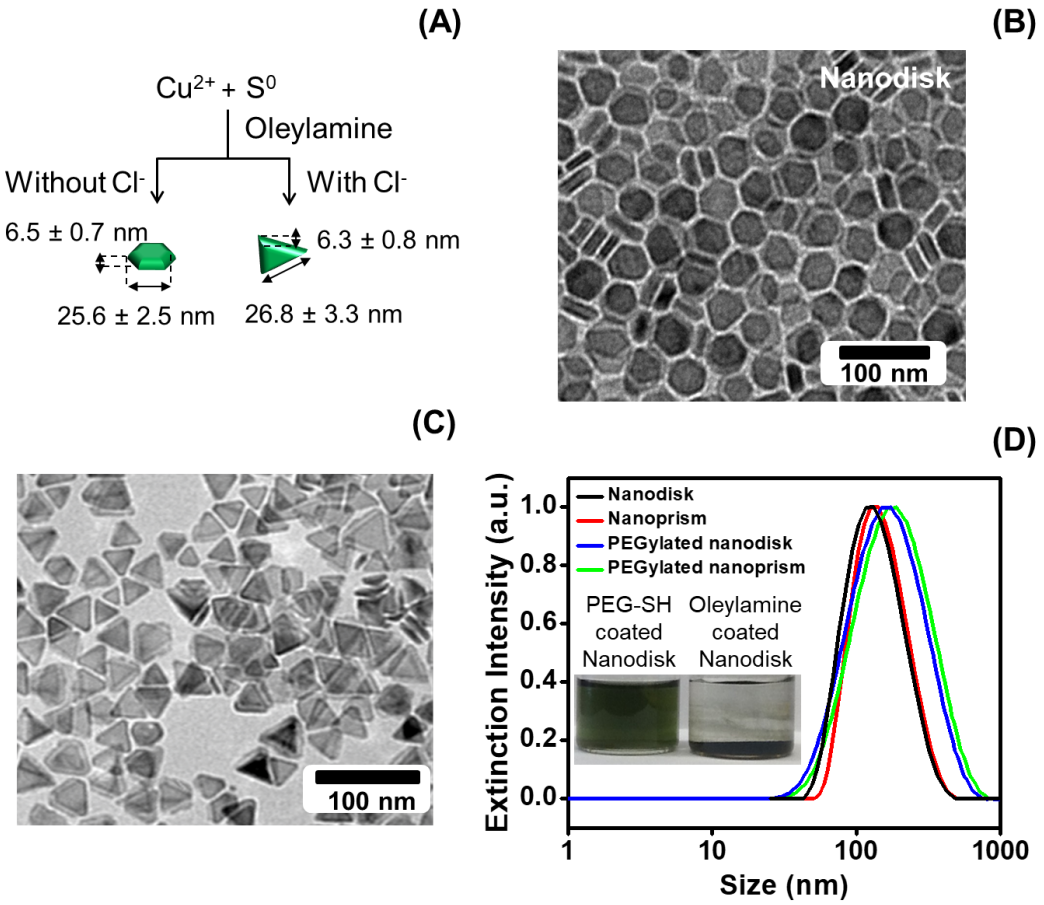

Figure 6. 1 Physical and chemical characterization of CuS nanodisks and nanoprism. Panel A depicts the synthesis of CuS nanodisk and nanoprism via a solvent-based and seed/halide ion-mediated process. Panels B and C are the TEM images of the CuS nanodisks and nanoprisms, respectively. The average diameter and thickness of CuS nanodisk was 25.6 nm and 6.5 nm. The nanoprism was 26.8 wide and 6.3 nm thick. Panel D shows the hydrodynamic radius of the oleyamine-coated nanodisks (85.3 nm) and nanoprisms (91.9 nm) in chloroform. The hydrodynamic radius of the PEGylated nanodisks and nanoprism dissolved in water increased to 125.4 and 131.7 nm respectively. While the oleynamine-coated CuS nanodisks precipitate in water, PEGylation stabilized the nanodisk in water (inset). The size difference between TEM and DLS is caused by the DLS algorithm that is optimized for spherical particles and is a potential error source.

6.3 Photoacoustic Response of CuS Nanodisks and Nanoprisms

The PEGylated CuS nanodisks and nanoprisms had strong optical and photoacoustic absorption at near-infrared wavelengths. The maximum extinction intensity of the nanodisk and nanoprism occurred at 1145 and 1098 nm, respectively (**Figure 6.2A**). The photoacoustic spectra of these two nanoparticles were slightly blue-shifted compared to their extinction spectra. Both types of CuS nanoparticles had maximum photoacoustic intensity at 945 nm, which is inconsistent

with their absorption peaks. Indeed, the absorption and photoacoustic peaks should be identical because photoacoustic signal is based on absorption. The difference seen in **Figure 6.2A** is because the laser on our photoacoustic scanner has a range of 680 to 970 nm; the laser power also decreases at more red-shifted wavelengths (**Supplementary Figure 5.4**). Nevertheless, both CuS nanodisks and nanoprisms had linear photoacoustic enhancement at 945 nm as a function of CuS concentration (R^2>0.97 for nanodisk and R^2>0.91 for nanoprism) (**Figure 6.2B**). The detection limits (three standard deviations above background) of nanodisks and nanoprism were 29 pM and 116 pM, respectively (**Figure 6.2C**). This is similar to values reported previously for gold nanorods.[171] The CuS nanodisks (RSD=0.84%) and nanoprisms (RSD=0.73%) also have stable signal and retain their structures under laser irradiation for 14 minutes—this is in sharp contrast to gold nanorods, which are known to deform at moderate laser fluence (**Supplementary Figure 5.5**).[183]

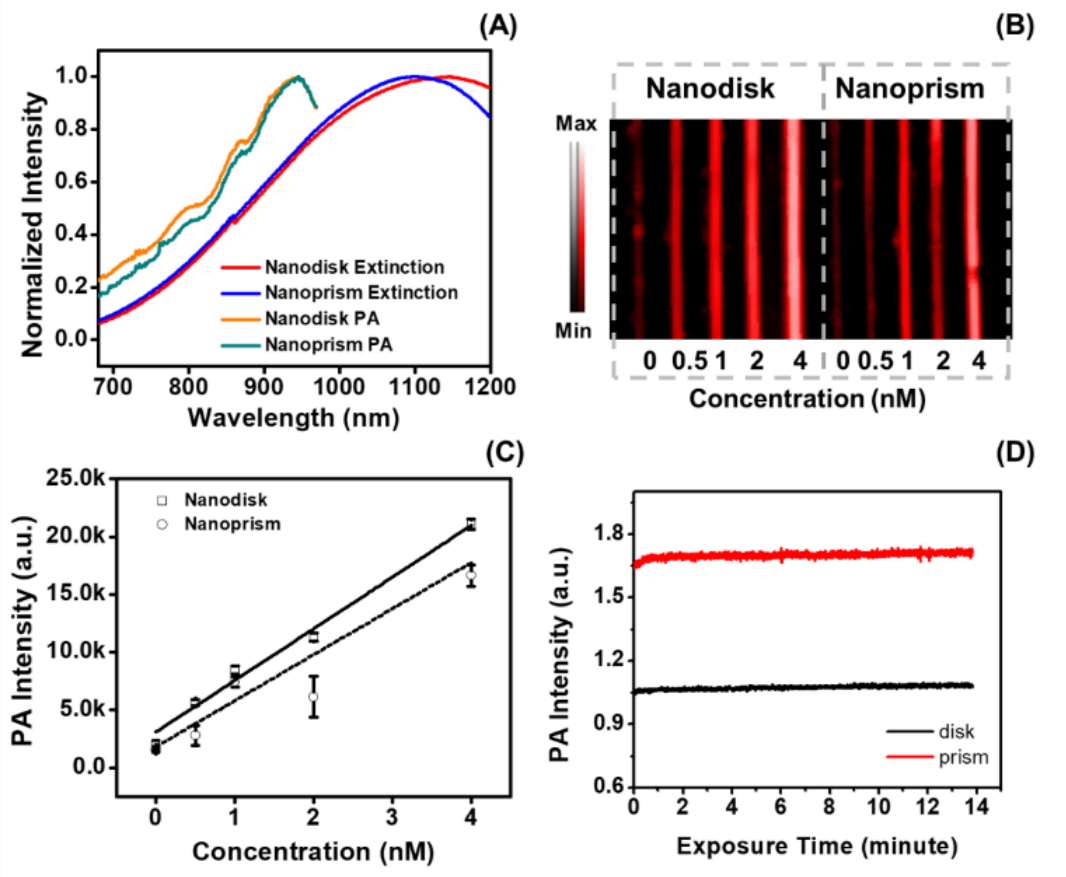

Figure 6. 2 Photoacoustic signal capabilities of CuS nanodisks and nanoprisms. Panel A compares the extinction spectra with the photoacoustic spectra of CuS nanodisks and nanoprisms. The extinction peak of nanodisks and nanoprisms was 1145 and 1098 nm, respectively, and both CuS nanoparticles had maximum photoacoustic output at 945 nm. The derivation of peak intensity between photoacoustic and extinction spectrum is due to the limited range of our laser (680 to 970 nm) and the lower laser energy at further infrared wavelengths. The photoacoustic intensity measured at 945 nm of the two CuS nanoparticles is shown in B. The corresponding intensity analysis shown in C revealed the linear correlation between the photoacoustic intensity and the concentration of the nanodisks (solid line, R^2>0.97) and nanoprism (dashed line, R^2>0.91). Panel D highlights the stability of CuS nanodisk (RSD=0.84%) and nanoprism (RSD=0.73%) over a 14-minute laser irradiation at 940 nm. Error bars in panel C and D represents standard deviation of 8 regions of interest.

6.4 Nanoparticle Accumulation in Ovarian Tumor and the Photoacoustic Imaging

Using the similar physical properties of the two CuS nanoparticles, we next studied the shape effect of the CuS nanoparticles on their accumulation in ovarian tumors. We intravenously injected 200 μL 50 nM CuS nanoparticles (or 5.4 nM in the mouse body assuming the average blood volume of a mouse is 74 mL/kg[184]) in nude mice bearing OV2008 xenograft ovarian tumors. This was a safe dose because we found that the ovarian cancer cells had 95% viability after the incubation with 5 nM nanodisk for 24 hours (**Supplementary Figure 5.6**). Furthermore, this CuS

nanoparticle concentration is 1425 times lower than the lethal dose of CuS nanoparticles (7.7 mM in the mouse body) reported by Feng *et al.*[185]. Other toxicity studies showed that a single dose below 4.2 mM of Cu[186] or 1.2 mM CuS nanoparticles[185] had minor toxicity in mice, even though Cu ions can be toxic at high concentration. This is because CuS nanoparticles have low solubility of free Cu.[186] The literatures suggest that CuS nanoparticles are relatively non-toxic. A detailed toxicity study of the CuS nanodisk and nanoprism was beyond the scope of this study. However, we used PEG-thiol to substitute for the oleylamine capping ligand similar to Guo *et al.* (Ref. 21), and this work suggested good biocompatibility.

The pharmacokinetic study used the Cu concentration in blood and tumor to evaluate tumor uptake and clearance. We first verified the Cu content in the nanodisks and nanoprisms on a per particle basis and found that the difference was 5.5%. The average Cu concentration in the blood from the mice (n=4) treated with nanodisks decreased from 42.5 to 18.6 ID%/g 8 hours after injection (**Figure 6.3A**). The Cu concentration in the mice treated with nanoprisms decreased from 48.8 to 1.0 ID%/g (**Figure 6.3A**). This indicated that the nanodisks had a longer circulation half-life than the nanoprisms.

The Cu concentration in the tumors treated with CuS nanodisks increased to 3.7 ID%/g 8-hour post-injection while the Cu concentration in the tumors treated with nanoprism initially increased to 2.5 ID%/g 4-hour post-injection and then decreased to 2.1 ID%/g 8-hour post-injection (**Figure 6.3B**). The difference of Cu concentration in the tumors suggested that the circular CuS nanodisks had more retention in the 2008 ovarian tumors than the triangular CuS nanoprisms. The longer retention of the nanodisk in the ovarian tumors was likely a result of its long half-life (**Figure 6.3B**). Other possible mechanisms include the strong adhesion of disk-like nanoparticles to the vascular wall and the geometry and size of the pore between the endothelial cells in the ovarian tumor.[178-180] Although the underlying mechanism requires further investigation, this data provides insights in the selection of nanoparticles for ovarian tumor imaging and therapy.

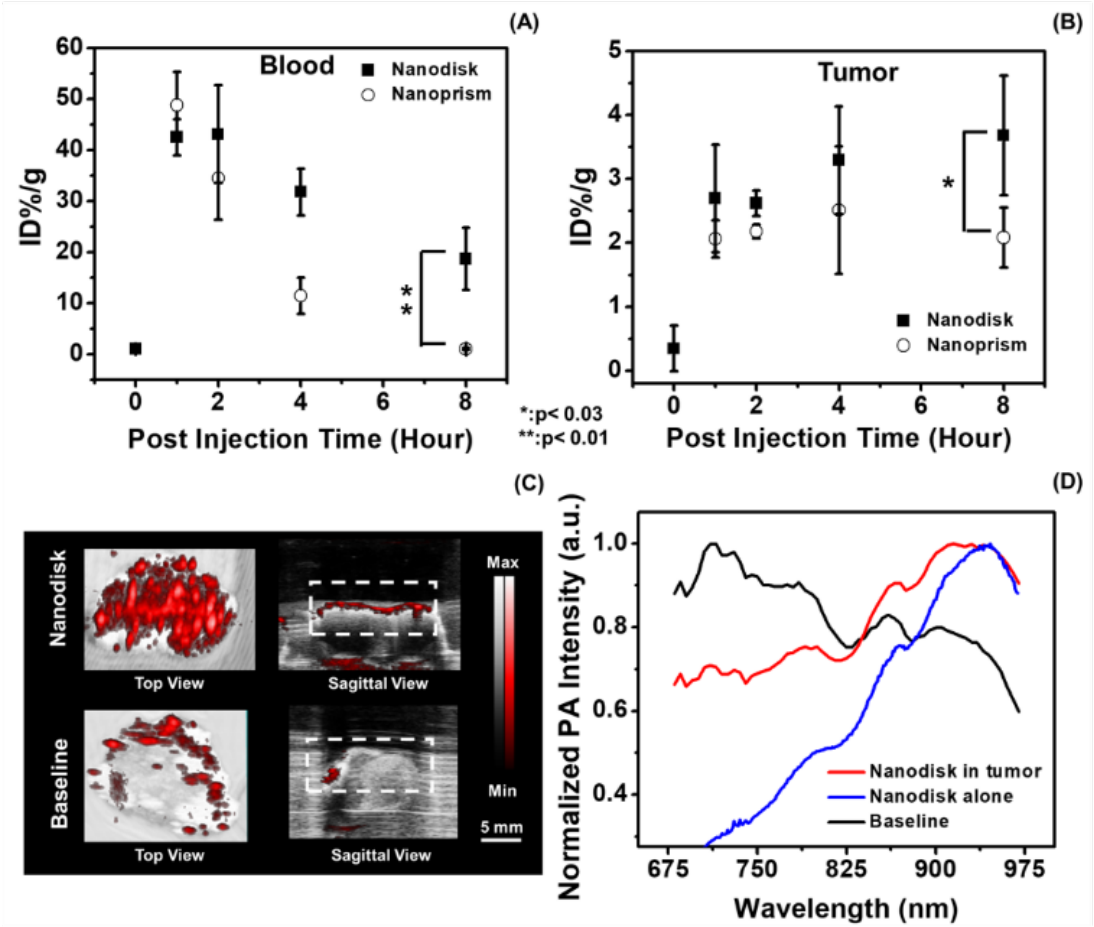

Figure 6. 3 Shape-dependent accumulation of nanoparticles in tumor and photoacoustic ovarian tumor imaging. Panel A and B shows the Cu ion concentration of the blood and tumor samples collected from mice treated with CuS nanodisks and nanoprisms, respectively. Eight hours after the treatment, the mice treated with nanodisk had 17.9-fold and 1.8-fold higher copper concentration in the blood and tumor than the mice treated with nanoprisms. Here the data points at baseline represent the tumor without any nanoparticle treatment. The error bars in panel A and B denote the standard deviation from 4 mice. Panel C showed the photoacoustic images at 920 nm excitation of the tumor samples from the mice treated with CuS nanodisk (Nanodisk) and the mice without treatment (Baseline). The white dash line labels the regions of interest for the photoacoustic spectral analysis (D). The photoacoustic spectral profile of the tumor treated with the nanodisk agrees well with the nanodisk particles alone. The animals treated with CuS nanodisks revealed a maximum photoacoustic signal at ~920 nm while the untreated tumors showed a maximum intensity at ~713 nm.

The tumors from the mice treated with CuS nanodisk (n=3) exhibited a strong photoacoustic intensity with a characteristic photoacoustic spectral profile. The average photoacoustic intensity of the tumors 8 hours post-injection of CuS nanodisks was 3.0-fold ($p<0.01$, n=3) higher than the baseline (i.e. tumor without any treatment) (**Figure 6.3C**). Furthermore, the photoacoustic spectra of the tumors treated with CuS nanodisks had their

maximum intensity at 920.0 ± 7.1 nm (**Figure 6.3D** solid) with a spectral profile close to the nanodisk alone (**Figure 6.2A**). In contrast, the baseline showed the maximum photoacoustic intensity at 713.3±2.4 nm (**Figure 6.3D** dash), which was likely due to hemoglobin.[187] The characteristic spectral peak at 920 nm could increase the contrast of the CuS nanoparticles in normal tissues by avoiding the interference of deoxygenated hemoglobin that has peak photoacoustic intensity at 750 nm.[188] The *in vivo* photoacoustic image in **Supplementary Figure 5.7** showed that the ultrasound signal can discriminate the tumor from adjacent tissues with the characteristic photoacoustic spectral information.

6.5 Conclusion

In summary, we report two CuS nanoparticle contrast agents, nanodisks and nanoprisms, for photoacoustic ovarian tumor imaging. Both CuS nanodisks and nanoprisms had sensitive photoacoustic signal at picomolar range, and the CuS nanodisks accumulate more in the human 2008 ovarian tumor models than the CuS nanoprisms. The photoacoustic image of the tumor treated with CuS nanodisks presented 3.0-fold higher intensity than the baseline and revealed a characteristic photoacoustic spectral peak at 920 nm.

Chapter 6, in full is currently being prepared for submission for publication of the material. Junxin Wang, Su-wen Hsu, Natalia Gonzalez-Pech, Anamik Jhunjhunwala, Fang Chen, Ali Hariri, Vicki Grassian, Andrea Tao, Jesse V. Jokerst. The dissertation author was the primary investigator and author of this paper.

Appendix A: Supplementary Figures and Methods of Chapter 2

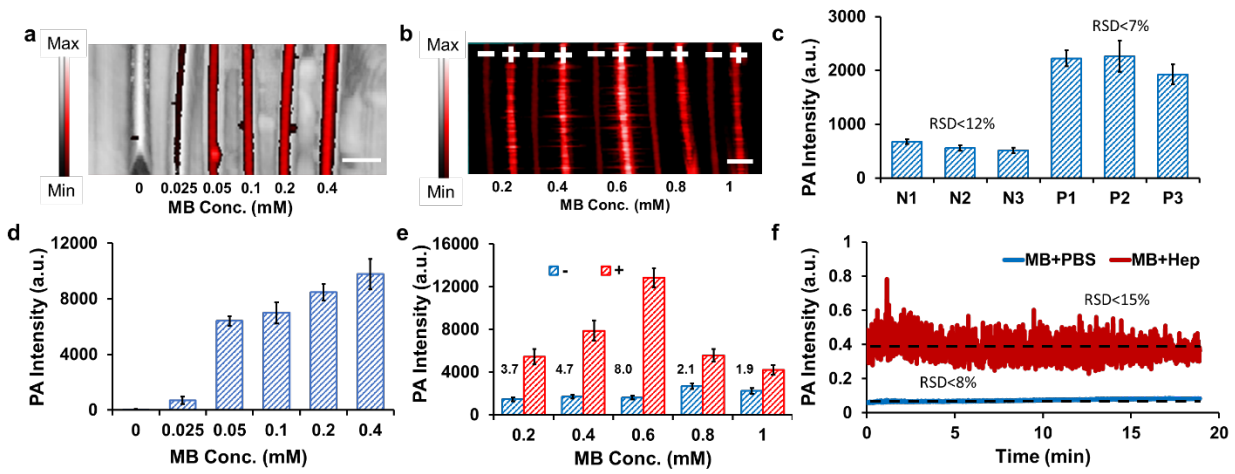

Supplementary Figure 1. 1 Stability and reproducibility of methylene blue/heparin complex. (**a**) Ultrasound (black and white) and photoacoustic (red) image of plastic tubing filled with increasing concentrations of methylene blue. Photoacoustic signal of sample was quantified in (**d**). (**b**) Increasing concentrations of methylene blue were added to PBS and heparin solution (6.4 U/mL) to identify the methylene blue (MB) concentration for optimal contrast. In panels **b** and **e**, negative (-) and positive (+) signal correspond to methylene blue only and methylene blue with heparin, respectively. The data was quantified in (**e**), and the overlaid numbers are the contrast of photoacoustic signal between negative and positive. Panel **c** shows the signal reproducibility of three methylene blue only samples (0 U/mL heparin; N1-N3) and three methylene blue/heparin samples in PBS (6.4 U/mL heparin; P1-P3). Panel **f** shows signal stability after imaging the samples continuously for 19 minutes.

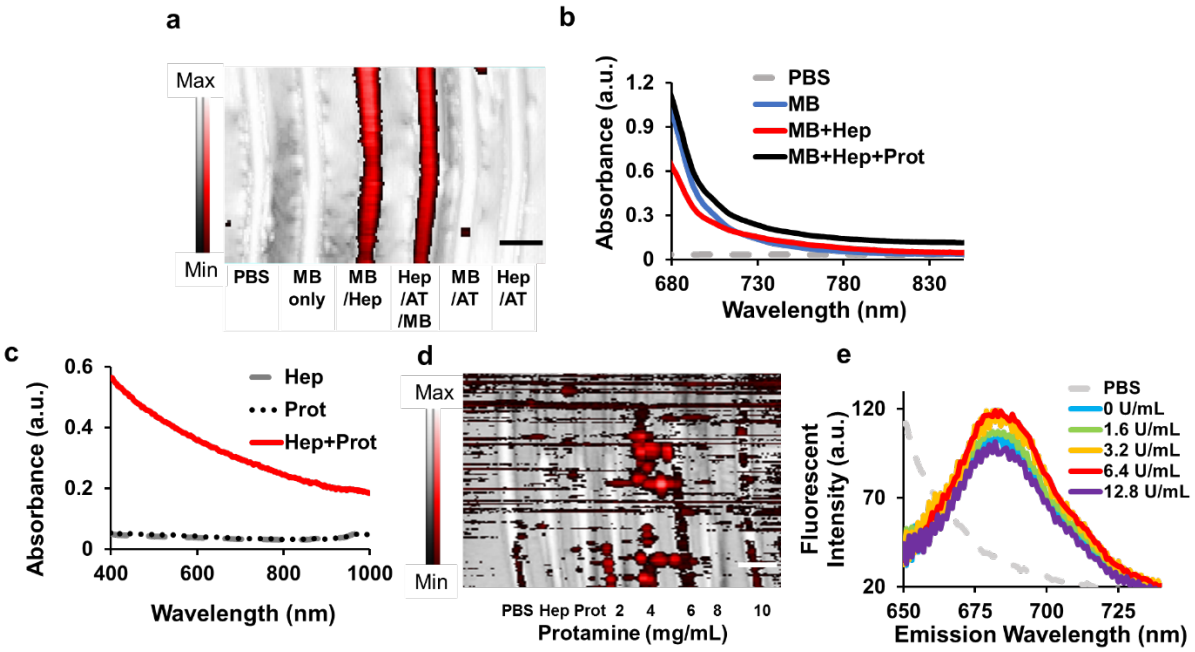

Supplementary Figure 1. 2 Mechanism of the binding between methylene and heparin. (**a**) Overlaid ultrasound and photoacoustic images show that both methylene blue/heparin complex and heparin treated with antithrombin followed by methylene blue have similar photoacoustic signal, which confirms the utility of this detection approach in the presence of antithrombin. Methylene blue with only antithrombin or heparin with only antithrombin have no signal. (**b**) Absorbance of methylene blue in the presence of heparin and protamine shows slightly elevated absorbance for the MB+Hep sample versus MB only above ~720 nm. (**c**) Absorbance of heparin, protamine and heparin/protamine complex shows that the heparin/protamine solution became turbid and had reduced transmission due to scattering, however these species do not produce photoacoustic signal because there is no chromophore (**d**) despite the absorbance in (**c**)**.** Note that in panel (**d)**, the images were collected at a very high gain resulting in significant background. This was to illustrate the lack of signal. Panel (**e**) shows the effect of increasing heparin concentration on methylene blue fluorescence. No increase in fluorescence or quenching is seen. PBS: phosphate buffered saline; MB: methylene blue; Hep: Heparin; AT: antithrombin.

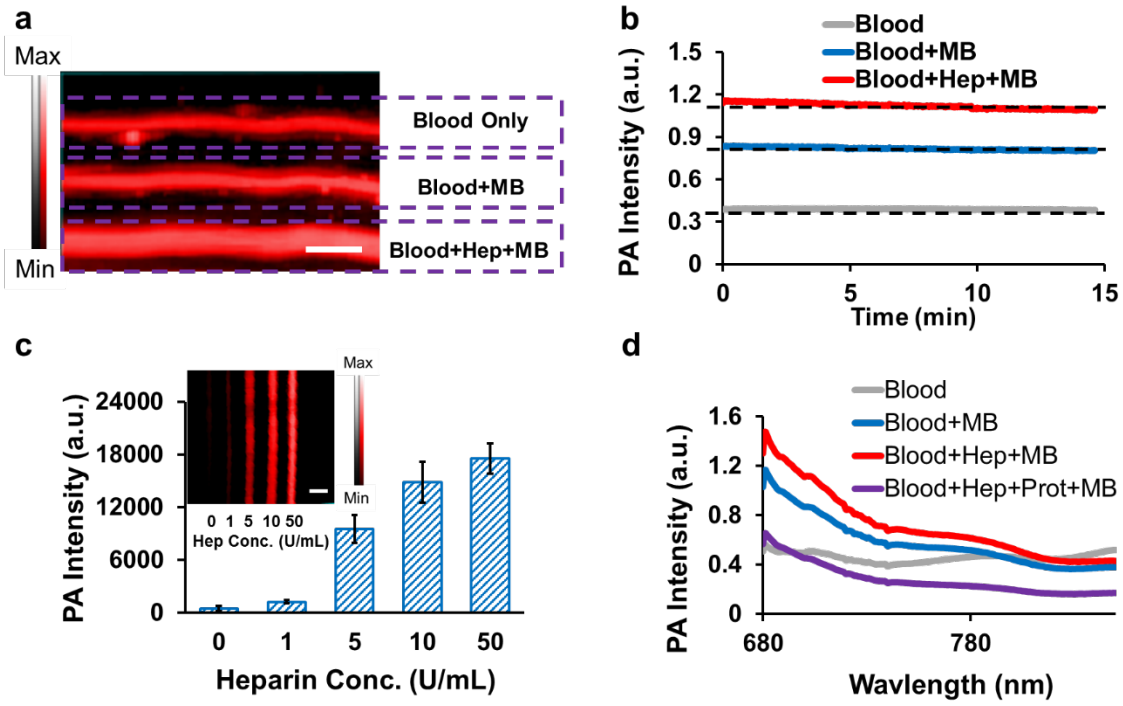

Supplementary Figure 1. 3 Utility of photoacoustic imaging in whole blood. Panel (**a**) contains whole blood, blood with 0.8 mM methylene blue, and blood with methylene blue and 5 U/mL heparin. The data show that endogenous glycosaminoglycans have little impact on signal creation relative to heparin. Panel (**b**) highlights the signal stability of these same blood samples with continuous imaging (<5%). Panel (**c**) shows the photoacoustic image of plastic tubing containing human blood with 0.8 mM methylene blue and increasing concentrations of heparin from 0 to 50 U/mL with 0.8 mM methylene blue. Note that the gain is reduced here to that the background signal is near zero. (**d**) Photoacoustic spectra of human blood as well as blood sequentially treated with methylene blue, heparin, and protamine. Scale bars in a and c are 3 mm.

Material and Methods

Reagents.

Methylene blue (98%) and human antithrombin III were purchased from Fisher. Heparin (sodium injection at 5,000 and 10,000 United States Pharmacopeia (USP) U/mL) was purchased from SAGENT pharmaceuticals. Protamine sulfate salt from salmon (grade I-A) was purchased from Sigma. UltraPure™ agarose was purchased from Invitrogen. Tetraethylorthosilicate (TEOS, >= 90.0%), ammonium hydroxide solution (28.0-30.0% NH_3 basis), and (3-mercaptopropyl)trimethoxy saline (MPTMS, 95%) were purchased from Sigma-Aldrich. Toluene was purchased from ACROS, and 200 proof pure ethanol was purchased from Koptec. PBS tablets were purchased from Fisher Scientific. Laboratory polyethylene tubing (OD: 1.27 mm, ID: 0.85 mm) was purchased from Harvard apparatus. Vacutainer coagulation tubes with 3.2% citrate solution or 75 USP sodium heparin were purchased from Greiner bio-one.

PBS Sample Preparation

One PBS tablet was dissolved per 200 mL deionized water for a 1X solution. Methylene blue was always prepared fresh by dissolving reagent-grade powder in PBS and filtering through 0.22 μm filter; 10 μL of the heparin solutions (0 – 496 U/mL in PBS) was added in 90 μL 0.6 mM methylene blue. The 10 μL of 8 mg/mL protamine was added to 6.4 U/mL to reverse methylene blue and heparin binding for absorbance measurements. To demonstrate photoacoustic reversibility, 10 μL of 1, 2, 3, 4, 5 mg/mL protamine was added in to 100 μL methylene blue/heparin solution containing 5 U heparin. An aliquot of the methylene blue/heparin solution was used for photoacoustic imaging. LMWH solutions were prepared in several dilutions (0, 0.2, 0.4, 0.8, and 1.6 mg/mL) and 20 μL solutions were added into 180 μL 0.4 mM methylene blue.

Human Blood Sample Preparation

Whole human blood was collected in citrate tubes from a healthy donor according to institutional guidelines. Samples (90 μL) were treated with 10 μL heparin (0 – 500 U/mL) followed by 100 μL methylene blue (1.6 mM) and imaged within 4 hours. To determine the correlation

between photoacoustic intensity and blood clotting time, 50 µL of heparin at 0, 0.25, 0.5, 1, 2, and 4 U/mL was added to 450 µL sodium citrate blood, respectively. This sample was repeated three times for error analysis. Citrated platelet-poor plasma was prepared by centrifuging 400 µL citrated blood at 2000 rcf for 15 minutes at 22 ^{o}C twice. The plasma was stored at -80 ^{o}C until aPTT analysis. A separate whole blood aliquot from this same sample was treated with methylene blue and imaged. To neutralize heparin, 0 (PBS), 40, or 80 µg of protamine sulfate was added to the blood collected in a sodium heparin vacutainer. For LWMH studies, concentrations from 0 to 0.16 mg/mL were used and analyzed with aPTT analysis as well as imaging. The blood and buffer samples were placed polyethylene tubing (~ 2 cm long); the ends of the tubing were sealed with heat. These were placed in a 1% agarose phantom for imaging or imaged with a customized phantom.

aPTT assay. Clotting times were determined in duplicate with an ST4 semi-automated mechanical coagulation instrument (Diagnostica Stago, NJ). Here, 30 µl of the aPTT reagent (Diagnostica Stago, NJ) was added to 30 µl of citrated plasma and incubated at 37°C for 5 min. This was followed by 30 µl of 25 mM $CaCl_2$ to initiate clotting. The time was measured in seconds required for blood clot.

Instrumentation. Absorbance measurements used a SpectraMax M5 spectrophotometer. The hydrodynamic radius and zeta potential were measured using dynamic light scattering (DLS) on a Zetasizer-90 instrument from Malvern Instruments (Worcestershire, UK) using 50% PBS in water as the diluent. Scanning electron microscopy (SEM) was performed with a XL30 ultrahigh resolution SEM (FEI Co.).

PA images were scanned using a Vevo 2100 commercial instrument (Visualsonics) equipped with a 21 MHz-centered transducer (LZ250) described previously[189]. The system uses a flashlamp pumped Q-switched Nd:YAG laser with optical parameteric oscillator and second harmonic generator operating at 20 Hz between 680 and 970 nm with a 1 nm step size and a pulse of 4 to 6 ns. The peak energy is 45±5 mJ at 20 Hz at the source. The full field-of-view is 14-

23 mm wide. The acquisition rate is 5 frames per second. The samples were aligned under the transducer at a depth of ~ 10 mm. The laser energy was calibrated and optimized using the build-in energy power meter and software before measurements. Typically, we used 100% laser energy with 10-40 dB gain and 21 MHz frequency. 3D scans were performed to image all part of the tubing at 680-710 nm excitation; photoacoustic spectra were collected from 680 to 850 nm.

SSNP@Agarose Hybrid.

Silica nanoparticles were made by mixing 50 mL ethanol, 5 mL Millipore water, and 2.2 mL ammonium hydroxide in a water bath at 30 °C for 5 minutes with stirring at 300 rpm[190].The stirring speed was increased to 1000 rpm for adding 4.2 mL TEOS in the mixture. Then, the stirring speed was reduced to 500 rpm, and the reaction continued for 2 hours. The product was washed with ethanol and Millipore water twice and dehydrated. To modulate the charge, 200 mg of the SSNPs were incubated with 0.2 mL MPTMS in 40 mL toluene with stirring at 300 rpm in either 110 °C silicone oil bath for 4 hours or at room temperature overnight. The nanoparticles were washed with toluene 3 times followed by pure ethanol for another 3 times. The nanoparticles were dissolved in 50% PBS after 5 minutes of sonication for zeta potential measurements to confirm the surface modification. The modified nanoparticles were incubated with 3.0 – 4.0 mM methylene blue in Millipore water for overnight. The methylene loaded thiol-modified SSNPs (SSNP-SH) were washed 4 times with Millipore water. The supernatants were saved for absorbance measurement to determine the amount of methylene blue loaded on nanoparticles. The amount of free methylene blue was determined by measuring the absorbance of incubation supernatant.

The amount of MB on silica nanoparticle was calculated by measuring the absorbance of the initial methylene blue solution and the supernatant after each wash. The amount of MB on the silica nanoparticle was back calculated based on Beer's law where the molar extinction coefficients were referred to the data published by Oregon Medical Laser Center (http://omlc.org/spectra/mb/mb-water.html). The size of the silica nanoparticle (>500

nanoparticles) was measured via TEM, and the mass of each particle was calculated based on the silica density. The silica nanoparticles were weighted before incubation and therefore the number of nanoparticle could be determined. The amount of MB on each nanoparticle was determined by dividing the total mole of methylene blue coated on the nanoparticles by the nanoparticle number. Then 2% hot agar was added to the nanoparticles with sonication in hot water for 10 minutes. The SSNP/agar were poured in polyethylene molds simulating an 18-gauge intravenous catheter and cooled for demolding.

Real-time reversibility test in blood

The real-time reversibility test was performed using a customized chamber that allows us to inject heparin and protamine in methylene blue/fresh human blood mixture under water as an ultrasound-coupling medium. The chamber was made by a 1.5 mL microcentrifuge tube with three holes drilled through the cap. The holes in the cap served as ports through which tubing could be secured. One port delivered 50 U/mL heparin, and the other delivered 0.5 mg/mL protamine. The third port served as a vent. The chamber was filled with 0.85 mL 1.6 mM methylene blue and 0.85 mL fresh human blood. The chamber was immersed in water and aligned 11 mm below the transducer and imaged. Then, 0.1 mL heparin and 0.1 mL protamine was injected in the chamber 30 and 68 seconds after the imaging started, respectively. The photoacoustic signal was recorded for more than 120 seconds; three data points were excluded as artifacts due to dust in the sample.

Sample Measurements

Tubing filled with sample were organized in parallel and placed 1 cm beneath the transducer. The 2D gain was optimized so that the background noise was negligible. The 3D scans were performed, and the image was processed as a maximum intensity projection. Spectral measurements were performed by measuring the cross-section of the sample tubing with persistence set to 10. A ROI was drawn on each sample area, and the photoacoustic intensity versus excitation wavelength were analyzed. For stability measurements, the sample tubing was continually exposed for about 10 minutes and recorded at 5 Hz.

Data Analysis and Statistical Treatment.

Photoacoustic images were exported as TIFF files and analyzed via ImageJ 1.49v[191]. Images were changed to 8-bit images and analyzed with region of interest (ROI) analysis using either the mean or integrated density function in ImageJ. Eight groups of data were collected using the same ROI for each tubing. Average and standard deviation were calculated using Microsoft excel functions “AVERAGE” and “STDEV”. The p values were calculated using 8 ROIs and Student’s t-test. Pearson’s r values were calculated with GraphPad PRISM. The detection limits were calculated at 3 standard deviations above the mean of the background signal.

Appendix B: Supplementary Figures and Methods of Chapter 3

A

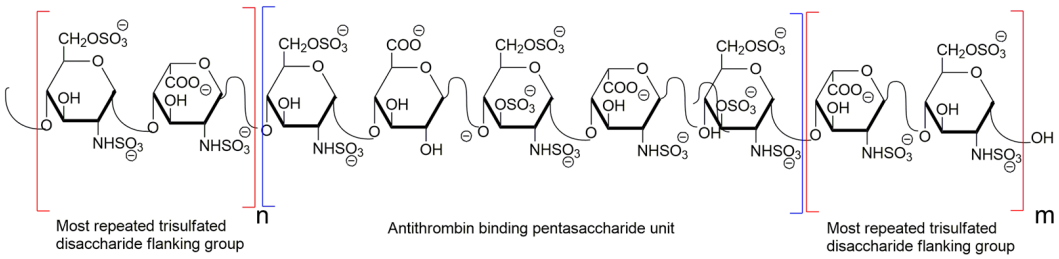

B

Equiv. of heparin	0.2	0.4	0.6	0.8	1.0	1.2	1.4	1.6	1.8
Heparin conc. (mg/mL)	0.09	0.19	0.28	0.38	0.47	0.56	0.66	0.75	0.85

Supplementary Figure 2. 1 Esitmation of heparin:MB binding ratio. Heparin chemical structure and estimated amount of heparin in MB-heparin mixture. Panel A shows the 3 subunits of heparin—an antithrombin binding pentasaccharide site, a flanking disulfated disaccharide, and the dominant repeated bridging trisulfated disaccharide units. Panel B shows the ratio between the estimated number of sulfate groups on heparin and concentration as a function of 0.90 mg/mL MB.

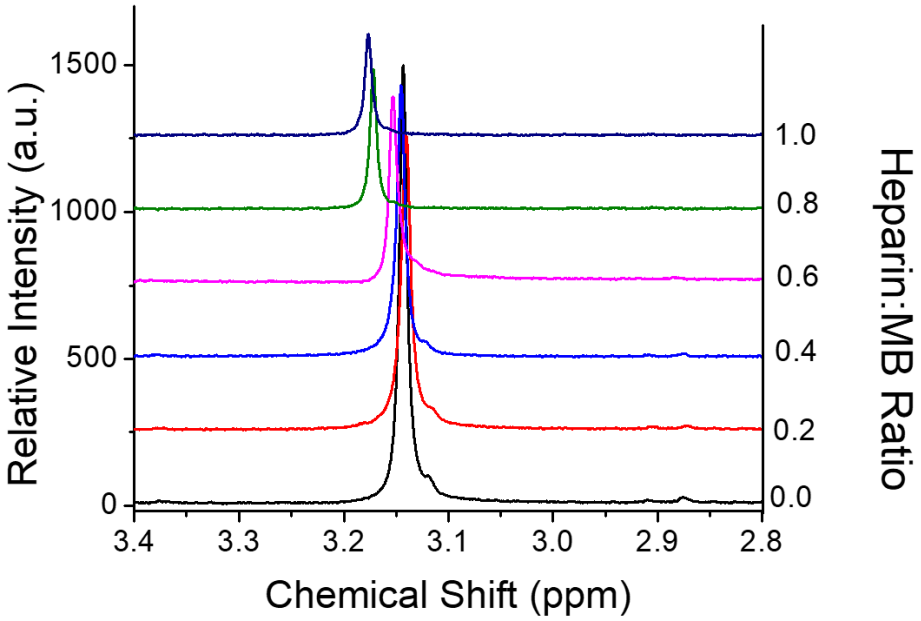

Supplementary Figure 2. 2 NMR spectra of MB as a function of heparin concentration. NMR spectra of the dimethyl amino proton of the 0.9 mg/mL MB with increasing heparin concentration. The NMR intensity decreased 76% when the heparin:MB ratio increased from 0.0 to 1.0.

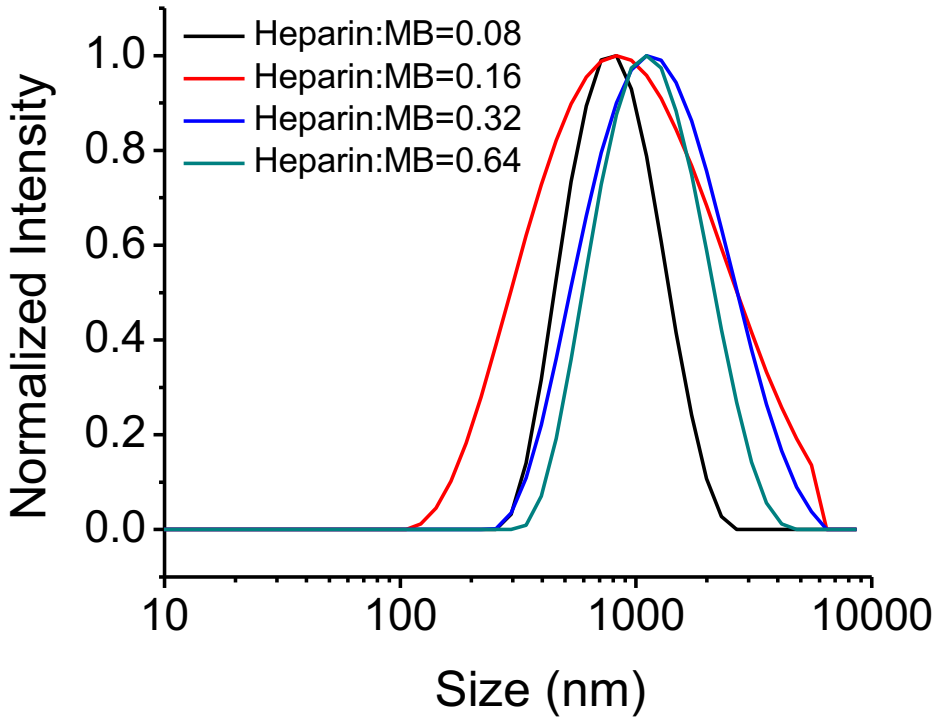

Supplementary Figure 2. 3 Size of MB-heparin aggregates. Size measurement of the MB-heparin aggregates as a function of heparin concentration. Increasing heparin concentration from 0.03125 to 0.25 mg/mL in 0.2 mM MB increased the MB-heparin aggregate size from 870 nm (0.03125 mg/mL) to 1451 nm (0.125 mg/mL) and then decreased the size to 1279 nm (0.25 mg/mL).

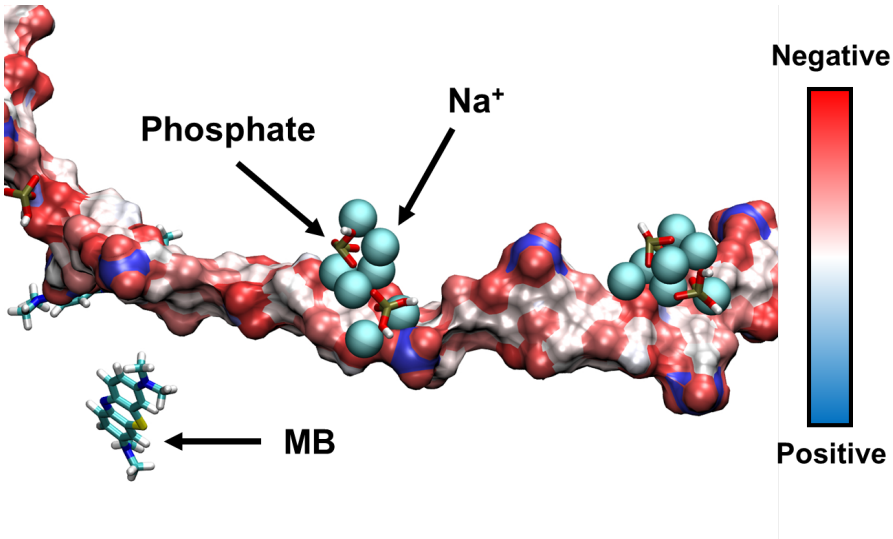

Supplementary Figure 2. 4 PBS effect in MB-heparin binding. This figure depicts the interactions between the binding residues of heparin (shown as a surface, red to blue represents charge from positive to negative) and the PBS solvent system (Na+ ions shown in blue and phosphate ions shown in yellow and red), producing a competition for binding sites between PBS and MB.

Materials and Methods:

Reagents

MB (98%) and PBS tablets were purchased from Fisher. Dissolving one PBS tablet in 200 mL deionized water should results in 0.01 M phosphate buffer, 0.0027 M potassium chloride, 0.137 M NaCl, and pH 7.4 at 25 ^{0}C. Heparin sodium salt from porcine intestinal mucosa (grade I-A, ≥ 180 U/mg) and protamine sulfate salt from salmon were purchased from Sigma. Heparin (sodium injection, 1,000 United States Pharmacopeia (USP) U/mL) was purchased from SAGENT pharmaceuticals. Deuterium oxide (D, 99.9%) was purchased from Cambrige Isotope Laboratories, Inc. Enoxaparin sodium (LMWH) injection was purchased from Winthrop. Laboratory polyethylene tubing (OD: 1.27 mm, ID: 0.85 mm) was purchased from Harvard Apparatus.

Preparation of MB-heparin mixtures

Stock MB solution MB was prepared by dissolving 1.898 mM MB in (M.W., 373.90 g/mol) deuterated water (D_2O) with sonication at 40 °C for 30 minutes. The final MB concentration was 4.8 mM. The molecular weight of the trisulfated disaccharide repeat units, in heparin backbone was 591.4 g/mol.[192] . The final heparin concentration was tuned based on the sulfate equivalence to get a 0, 0.2, 0.4, 0.6, 0.8, 1.0, 1.2, 1.4, 1.6, and 2.0 equivalence of heparin with respect to MB (final concentration of 2.4 mM). This was accomplished by mixing 0.6 ml of 4.8 mM MB solution with 0 to 540 µl of 1.898 mg/ml heparin solution. Additional D_2O was added in to the sample to keep the total volume at 1.2 mL.

To characterize the influence of MB on the aggregate size, 500 µl of 0.2, 0.3, 0.4, and 0.6 mM MB was added into 500 µl of 0.0125 mg/mL heparin solution. The influence of heparin concentration on the MB-heparin aggregate size was measured by mixing 500 µl of 0.4 mM MB with 500 µl of 0.0625, 0.125, 0.25, and 0.5 mg/mL heparin.

To study the effect of PBS, PBS tablet was crushed into powders. MB-heparin sample with 2.4 mM MB and 1X PBS was prepared by mixing 0.6 mL of 1.8 mg/mL (i.e. 4.8 mM) MB

solution with 0.6 mL heparin (0.94 mg/mL for heparin:MB ratio at 1.0 or 1.70 mg/mL for heparin:MB ratio at 1.8) that contains 12 mg PBS powder. In the sample with 2X PBS, the amount of PBS was increased to 24 mg. MB-heparin sample with 0.15 mM MB and 1X PBS was prepared by mixing 0.6 mL 0.1125 mg/mL (i.e. 0.3 mM) MB with 0.6 mL heparin (0.047 mg/mL for heparin:MB ratio at 0.8 and 0.106 mg/mL for heparin:MB ratio at 1.8) that contains 12 mg PBS powder. The influence of NaCl was characterized by dissolving 9.6 (i.e. 137 mM) or 19.2 (i.e. 274 mM) mg NaCl powder in the MB-heparin solution.

NMR Characterization

The NMR spectra of 2.4 mM MB with 0.2, 0.4, 0.6, 0.8, 1.0, 1.4, and 1.8 equivalence of heparin were measured using a Bruker AVA 300 MHz NMR spectrometer to study the aggregation of MB in the presence of heparin. The MB/heparin solutions prepared in D_2O with PBS or/and NaCl as mentioned in the previous paragraph were also characterized to determine the impact of PBS and NaCl on MB-heparin interaction. The number of scans used was kept constant at 32 scans to compare the NMR peak intensity between different mixtures.

Characterization Using Absorbance Spectroscopy

The solutions were mixed by vertexing and transferred into a 4 µl well plates for absorbance measurement. The amount of dye sequestered in the MB-heparin aggregates was estimated by measuring the absorbance of the supernatant of the samples that had been centrifuged at 10000 rpm for 5 minutes. Then the area under the peak between 400-800 nm was used to calculate the relative amounts of MB sequestered in the precipitate formed after addition of heparin. All absorbance spectra were measured by SpectraMax M5 spectrophotometer.

PA characterization

About 17 µl of MB-heparin mixtures used for absorbance and NMR studies were transferred into the polyethylene tubing. The PA image of these tubes were acquired on PA imaging system (Visualsonics) with analysis and parameters described previously[100]. The 3D images acquired were processed using image J software to estimate the pixel intensities[191].

Computational Methodology

The structure of heparin was constructed via GLYCAM Carbohydrate Builder software[193]. Specifically, the four monosaccharide units that were used in this study were YZB, WYS, YuA, and QYS. This pattern was repeated six times to construct the heparin polysaccharide. Each monosaccharide and MB was parameterized using Gaussian HF/6-31G*[194] through the WebMO interface[195]. The surface of heparin was evaluated as a potential binding surface for MB using the VMD software.[196] MB was docked to heparin using AutoDock Vina[197] placing MB within each of the possible binding sites, then simulating only the 14 most favorable docking conformations.

Heparin-MB interactions were characterized *in silico* using molecular dynamics simulations. Simulations were performed on heparin with 0, 1, 4, 7, 10, and 14 MB docked in the presence of either a PBS solvent system or a 0.154 M NaCl solvent system that closely reflected experimental conditions. The simulation of the 0.154 M NaCl and PBS systems were performed in six MB concentrations (0, 1, 4, 7, 10, 14 MBs) for 3 trials per concentration, resulting in 36 systems. Each system was minimized in seven restrained steps to eliminate bad contacts, heated in one step to 300 K, and equilibrated in seven steps, with each step reducing the imposed restraints on the systems. These preparatory operations and the unrestrained simulations were all completed using Amber 16[198] with the *ff14SB*[199] and GAFF force fields[200], while also utilizing additional parameters provided by GLYCAM. All unrestrained simulations were run for a minimum of 100 ns, with a time step of 2 fs, and at constant temperature and pressure of 300 K and 1 atm, respectively. Binding events of MB to heparin were measured using a 9.47 Å distance between the center of mass of MB and the nearest heparin residue. We evaluated the frequency of dimer formation per every 10 ns of simulated time. A dimer that could have π-π interactions was defined as a distance of less than 4.0 Å between the two centers of mass. Visualization and distance analyses were completed using VMD and the *cpptraj* module of Amber, respectively.[201] Free energy analysis was performed on each simulation using the MMPBSA.py[117] module of Amber.

Data Analysis and Statistical Treatment

The average and standard deviation of the integrated density were calculated using Microsoft excel functions “AVERAGE” and “STDEV”. P value of the number of MB dimer formation was calculated via the one-tailed test using Microsoft excel functions “TTest”.

Appendix C: Supplementary Figures and Methods of Chapter 4

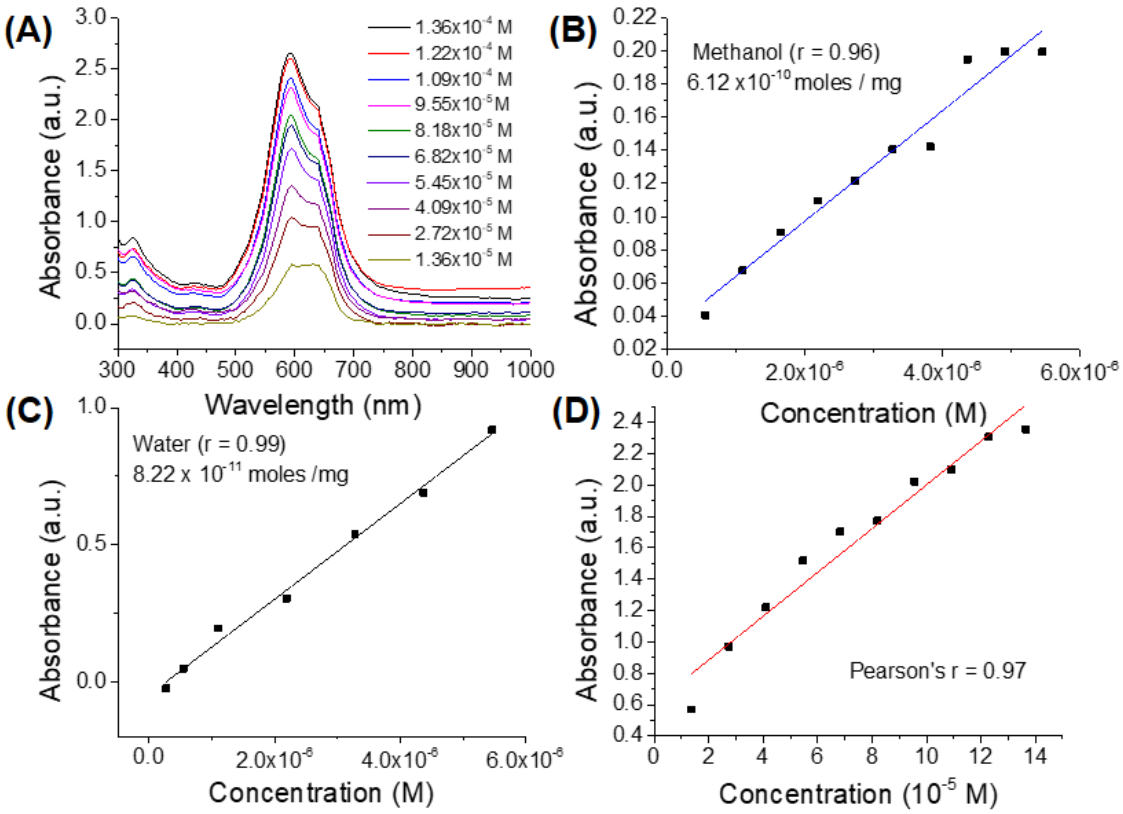

Supplementary Figure 3. 1 Absorbance of Nile blue A. (A) Absorption spectra of Nile blue A at different concentrations shows that the spectral shape of Nile blue A is independent of concentration. (B) A calibration curve for different molarities of Nile blue A in methanol. This calibration curve was used to estimate the total dye loaded on the paper substrate. The total dye loaded was estimated to be 6.12 x 10-10 moles per mg of substrate. (C) Calibration curve of absorbance of Nile blue A at different molar concentrations in water. This calibration curve was used to estimate amount of dye leached out of sensor in PBS medium. (D) Absorbance of Nile blue A at 595 nm is linear with respect to different concentrations with a Pearson's r value of 0.97 data derived from spectra of same solutions presented in (A).

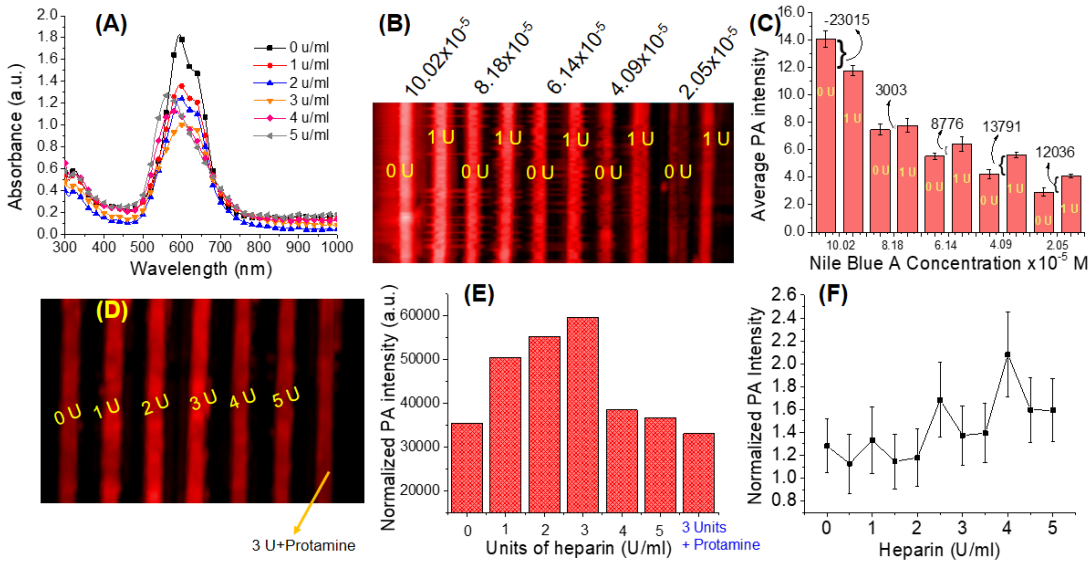

Supplementary Figure 3. 2 Absorbance and PA intensity of Nile blue A with heparin. (A) Absorbance of Nile blue A in aqueous solution (4.09x10-5 M) with different units of heparin. (B) Photoacoustic image of various concentrations of Nile blue A in deionized water with 0 and 1 units of heparin. Panel (C) shows the quantitative result of image in panel (B). Panel (C) clearly shows that highest contrast between 0 and 1 U/ml heparin is achieved at 4.09x10-5M Nile blue A concentration. Panel (D) and (E) are the photoacoustic image and processed data using 4.09x10-5M Nile blue A with different units of heparin. The maximum photoacoustic intensity is observed at 3 U/ml heparin while the maximum PA is reversed upon addition of the known heparin antagonist protamine sulfate at 54 µg/U of heparin. Panel (F) represents the PA response of cellulose sensor with only Nile blue A without PEG.

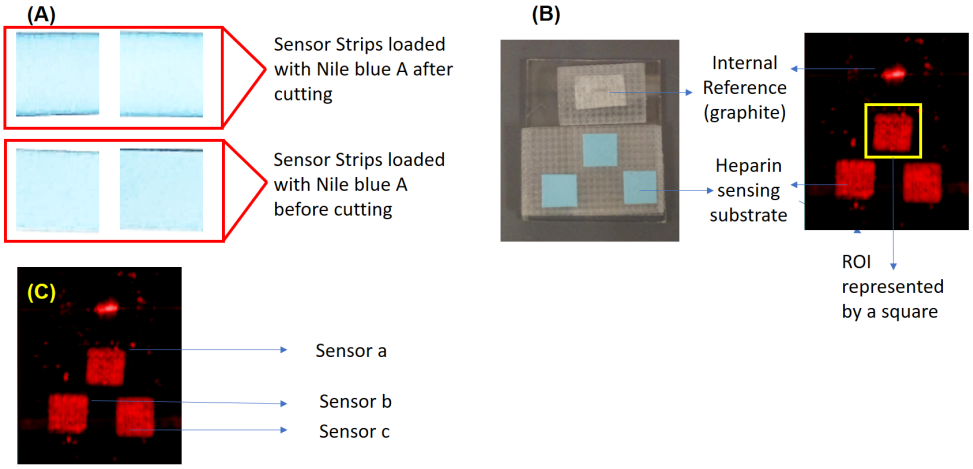

Supplementary Figure 3. 3 Cellulose sensor for photoacoustic measurement. (A) Magnified image of sections of sensor strips treated with Nile blue A solution before and after cutting. The sensor strips treated with dye solution after cutting show high dye accumulation along the sides of sensor strips. Heparin sensors immobilized on a glass plate with internal graphite reference (B) under visible light and the corresponding photoacoustic image. Here, the internal reference including the sensor strips are labeled, and the ROI used to measure the photoacoustic intensity of the sensors is illustrated by the yellow square. (C) The order of labeling is illustrated. The same order of naming is used in the intra-assay and inter-assay sensor comparison.

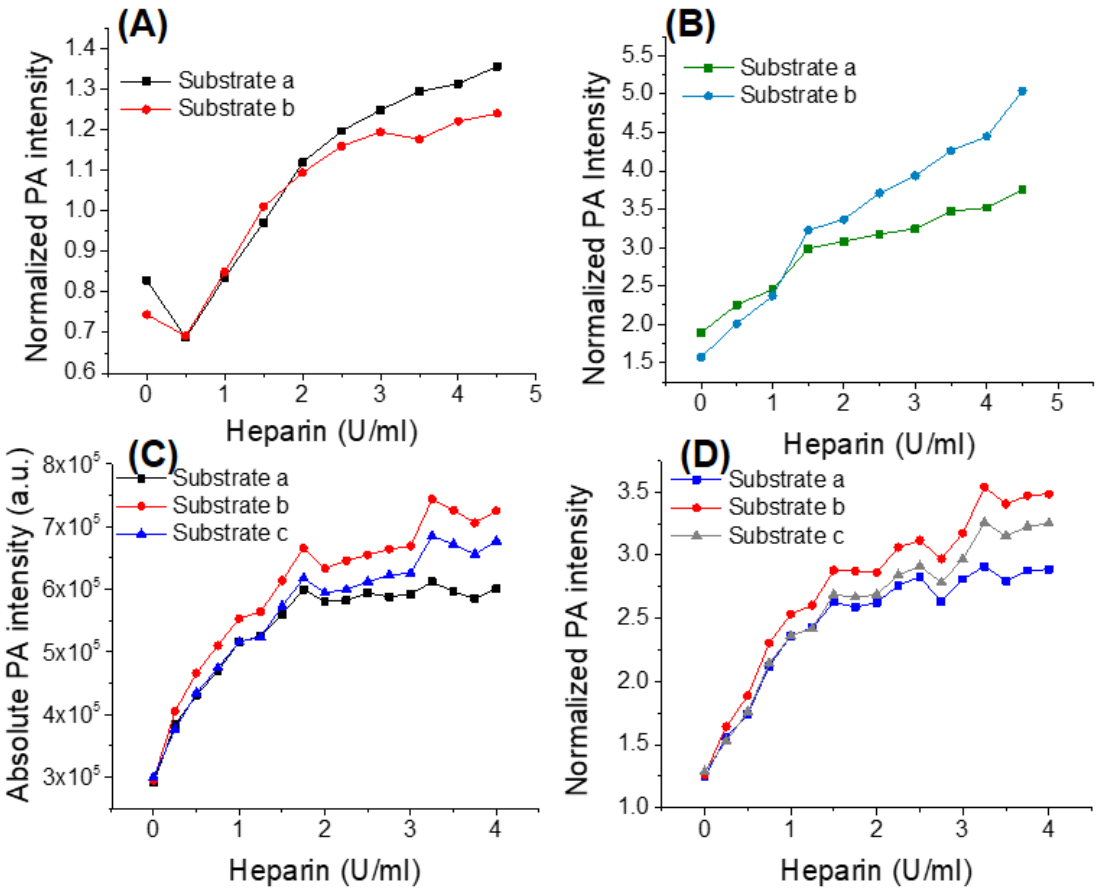

Supplementary Figure 3. 4 PA measurement of cellulose sensor in PBS and diluter plasma. (A) The photoacoustic response of two sensor substrate (before soaking in PBS medium) from two independent experiments to increase the amount of heparin in PBS. The substrate exhibits a photoacoustic response with increasing heparin with a slight drop in signal at 0.5 U/ml heparin. (B) When the cellulose sensors were immersed in PBS medium at room temperature for a minimum of 10 minutes before the study, the decrease was not observed. The initial decrease is likely due to the initial hydration of the substrate with Nile blue A that is insoluble in PBS medium. The wettability of the paper-based sensors has been shown to have a strong correlation to response time[130]. Panel (C) shows the change in absolute PA intensity, and (D) the photoacoustic intensity normalized to the reference graphite area in 50 diluted human plasma. Pooled human plasma was diluted with phosphate buffer to obtain the 50% diluted human plasma.

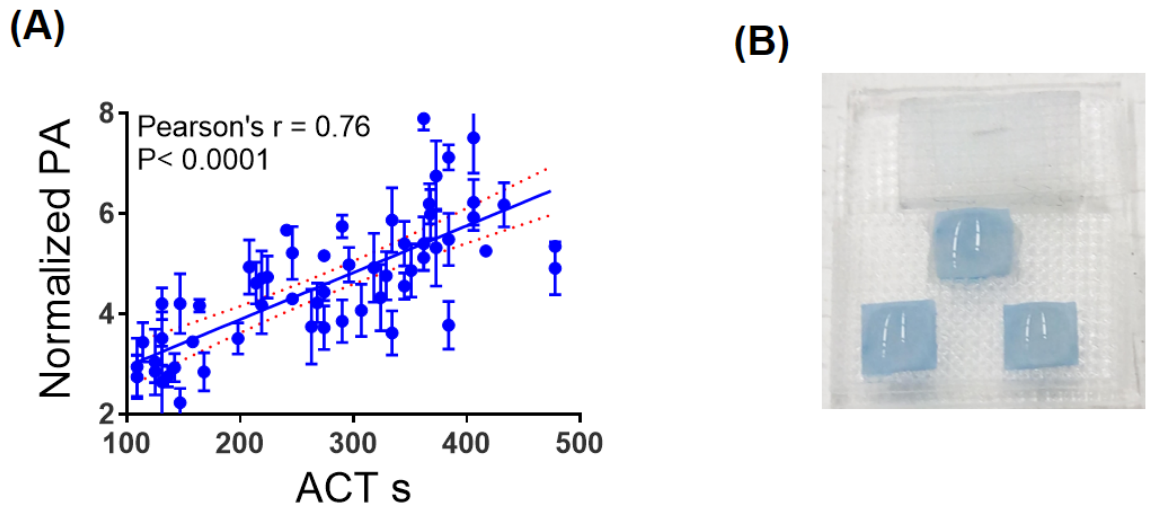

Supplementary Figure 3. 5 Additional data of for the correlation measurement between the PA intensity and the ACT. (A) Figure depicting the photoacoustic response of cellulose sensors as a function of ACT for every clinical sample without binning. (B) Photograph of the clinical sample (plasma) placed on each of the three sensor strips.

Materials and Methods

Chemicals and samples collection

Nile blue A and polyethylene glycol (Mn 7,000-9,000) (Bioultra 8000) were purchased from Sigma Aldrich Inc. and used as received. Methanol and phosphate buffered saline tablets was purchased from Fisher and used without further purification. Whatman No. 2 filter paper circles were purchased from GE Healthcare, U.K. Unfractionated heparin (1000 U/ml) was purchased from McKesson Corporation, USA. Normal pooled human plasma was purchased from Innovative Research Inc., USA. IRB approval was obtained prior to the start of this study for all human specimens. Blood was obtained with consent from healthy donors in 3.2% sodium citrate vacutainers (BD Life Sciences).

Methods used for clinical sample collection and storage

Samples (2-5 ml; 3-10 per patient) were obtained in parallel with the specimens already collected for the ACT—at baseline prior to the procedure, during heparin infusion, for maintenance of anticoagulation, and at the end of the procedure. The ACT measured as part of the clinical procedure was recorded for each specimen along with the timing of each dose of i.v. heparin. The

samples collected during heparin infusion to reach steady-state anticoagulation (> ACT of 470 s) were used for comparison to the photoacoustic technique. Plasma was separated from each sample and stored at -80 °C. Each set of samples was collected at different points, and the amount of heparin infused was recorded. All samples were thawed at 37 °C before analyses and studied within 24 hours of thawing. The photoacoustic gain of the instrument and the reference graphite mark was the same for all clinical specimens.

Data treatment and processing

The imaging data were processed and exported as JPEG images using Vevo LAB software and analyzed using ImageJ [202]. The JPEG image files were first converted to 8-bit greyscale images, and the pixel density was measured using region-of-interest (ROI) analysis. The ROIs covered the entire sensor area, and we exported the integrated pixel density of each ROI. The sensors were named sensor a, sensor b, and sensor c. The ratio of individual integrated pixel intensities of each sensors to the pixel intensity of internal reference graphite mark was plotted against the units of heparin added to the sample to demonstrate inter assay reproducibility. The average of these ratios corresponding to three sensors was plotted against the units of heparin added. The imaging data was analyzed using GraphPad Prism. The limit of detection (LoD) was defined as the concentration producing signal detectable three standard deviations above the mean of the blank in the linear region of the calibration curve (0-2.0 U/ml heparin). A linear fit between 0-2.0 U/ml in each medium was used to find the Pearson's r as a linear correlation coefficient.

Selection of Nile blue A as active component of cellulose based sensors

Constructing this sensor involved choosing a solid substrate and a chemical sensor. Heparin is a polysulfated glycosaminoglycan (**Fig. 3.1A,** main text) that can electrostatically interact with cationic dyes like methylene blue, 1,9-dimethylmethylene blue, and Mallard blue exhibit spectral changes proportional to the amount of heparin [142, 203]. This change in absorption can lead to increased photoacoustic signal. While our previous work used methylene blue with

photoacoustics to measure heparin[100], this work used Nile blue A (**Fig. 4.1B,** main text) because of its solubility features: Nile blue A is highly soluble in deionized water (50 mg/mL) but is insoluble (< 0.00001 mg/ml) in 0.01 M PBS due to ionic strength and pH. This insolubility could non-covalently immobilize Nile blue A onto the cellulose for interactions with heparin [204] (both cellulose and heparin are hydrophilic polysaccharides).

Spectral and photoacoustic properties of Nile blue A in aqueous solution

Nile blue A has a wide absorption band between 450-700 nm and is a suitable candidate for photoacoustic imaging with 680 nm excitation. The wavelength of maximum absorbance of Nile blue A dissolved in deionized water (595 nm) did not change between 1.364 x 10^{-5} and 1.364 x 10^{-4} M (**Supplementary Figure 3.1**). The absorbance at 595 nm was linear with concentration (Pearson's r=0.97; **Fig. 4.1C** and **Supplementary Figure 3.1 C**). A control experiment showed that the maximum signal increase due to heparin between 0 and 1 U/ml heparin was at 4.09x10^{-5} M Nile blue A (**Supplementary Figure 3.2 (C)**). Thus, 4.09 x 10^{-5} M Nile blue A was used was further study (**Supplementary Figure 3.1**).

The absorbance of Nile blue A at 595 nm in water decreased with heparin concentration from 0-3 U/ml. The photoacoustic signal of the same samples sharply increased with a maximum at 3.0 U/ml (see **Supplementary Figure 3.2**). The addition of more heparin beyond 3.0 U/ml resulted in a blue shift, and the corresponding photoacoustic signal sharply decreased. The plateau effect near 3.0 U/ml was similar to methylene blue[100].

Optimization of cellulose based heparin sensors

Cellulose is very attractive as a scaffold for sensor applications due to its low cost, biodegradability, and robustness [205]. Cellulose is a polysaccharide with glucose repeat units; thus, it is hydrophilic and can interact with a hydrophilic analyte dissolved in an aqueous medium [206]. Whatman filter papers are made of pure cellulose and have no background photoacoustic signal. Hence, Nile blue A dye was loaded onto PEG-modified Whatman No. 2 filter paper. A separate set of experiments were performed with 10, 20, 30, and 40 mg/ml PEG loading concentrations.

The best sensitivity was observed with 20 mg/ml of PEG (data not shown). Treatment of cellulose substrates with 20 mg/ml solution PEG resulted in 0.032 mg of PEG per mg of cellulose substrate.

A control experiment used the cellulose substrate loaded with only Nile blue A and no PEG. This showed poor response to heparin in PBS (**Supplementary Figure 3.2F**) and is likely due to poor interactions of the dye with the PBS**.** It was critical to have a uniform distribution of the dye throughout the paper. Hence, we used a full filter paper circle to prepare the heparin sensors and then cut away the edges. This minimized the irregular loading that can occur due to capillary forces on the edges as shown in **Supplementary Figure 3.3E**.

Heparin sensors were characterized for the total dye loaded and the amount of dye lost due to leaching using the calibration curves in **Supplementary Figure 3.1**. The total dye loaded was calculated to be 6.12×10^{-10} moles per mg of cellulose. Similarly, the amount of dye leached out in phosphate buffer was 8.22×10^{-11} moles per mg of cellulose (**Supplementary Figure 3.1**). Thus, 86.6% of the loaded dye is stably sequestered into the substrate.

3.1.7 Preparation of cellulose-based photoacoustic heparin sensors.

Whatman 2 filter paper was used to prepare cellulose-based heparin sensors with a two-step process. The concentrations of PEG and dye were optimized iteratively. Whatman filter paper circles were first treated with 2% w/v of PEG in methanol for 20 seconds and dried under ambient conditions for 5-10 minutes. The PEG-impregnated cellulose substrate was later dipped in a 2.72×10^{-4} M solution of Nile blue A in methanol for 20 seconds dried for 10 minutes under ambient conditions. The Nile blue A-infused sensor was cut into 0.5 x 0.5 cm squares and used for further study. To estimate the amount of PEG loaded into the substrates, about 1 g of cellulose substrate (filter paper) was dipped in methanol solution (20 mg/ml) of PEG and dried for one hour under vacuum. To estimate the amount of dye loaded into the cellulose, a known weight of the cellulose-based sensors was sonicated and mixed with a vortex shaker in methanol. After all of the dye was washed out, the total dye in the methanol wash was estimated using a calibration curve.

Instrumentation

UV-visible absorbance spectra were recorded on a Spectromax M5 spectrophotometer. Photoacoustic images were scanned using Visualsonics Vevo 2100 commercial instrument—a 21 MHz central frequency transducer (LZ250) was attached to a stepper motor to create 3D images. The aPTT measurements were performed on ST4 semi-automated mechanical coagulation instrument (Diagnostica Stago, NJ) according to the manufacturer's instructions. The activated clotting time (ACT) for the clinical blood sample were obtained from i-STAT 1 300-G Analyzer (Abbott Point of Care Inc., IL)

Appendix D: Supplementary Figures and Methods of Chapter 5

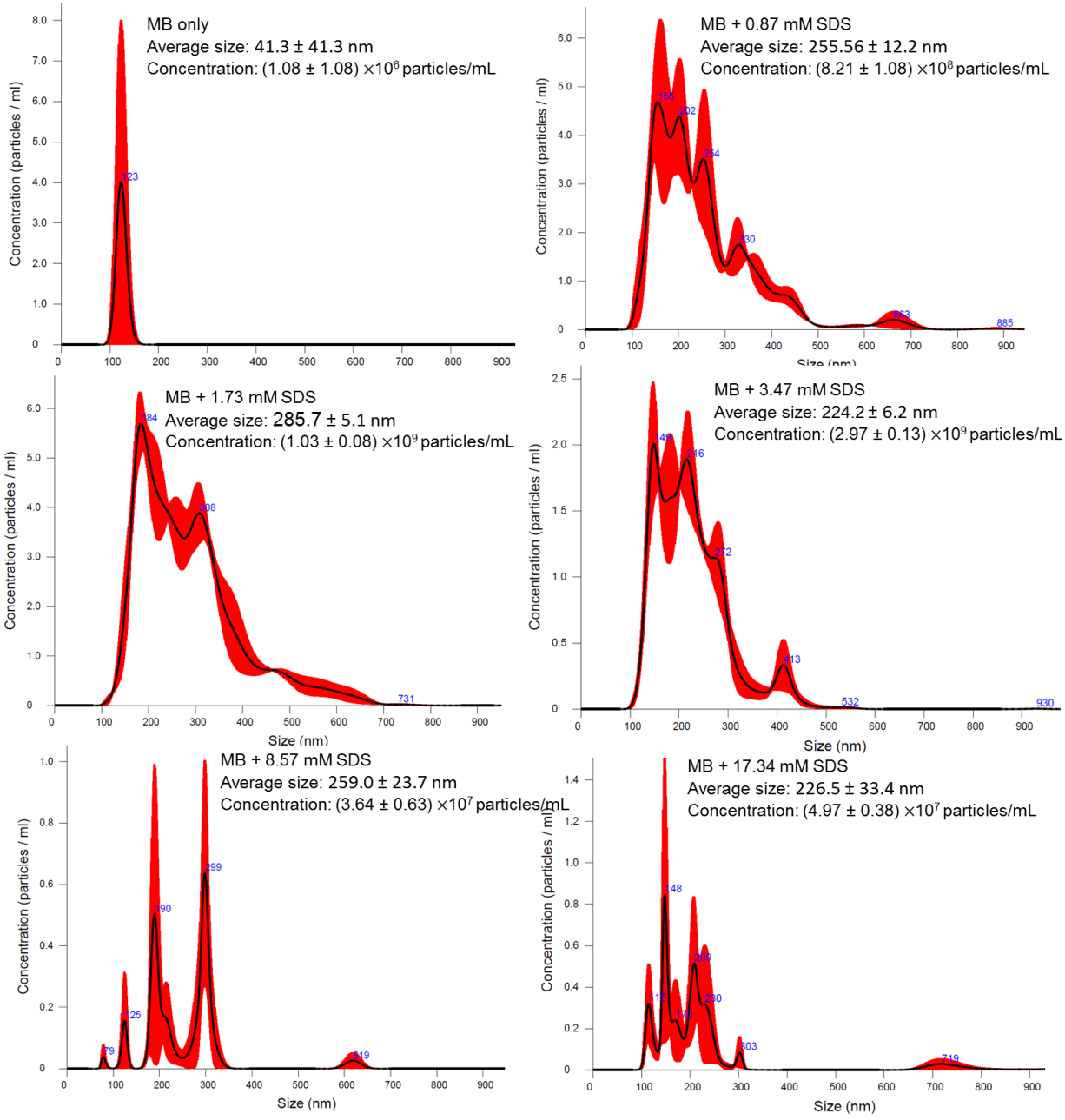

Supplementary Figure 4. 1 Measurement of size distribution and concentration of MB-SDS aggregate. NTA quantifies the size distribution and the concentration of all 0.05 mM MB with increasing SDS concentration from 0.78 to 17.34 mM.

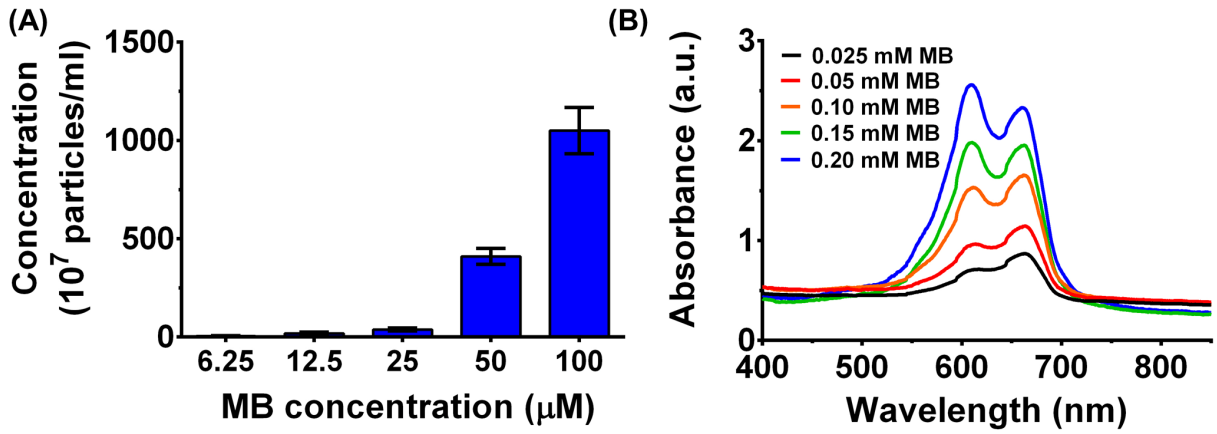

Supplementary Figure 4. 2 MB concentration dependent spectral and aggregation concentration change. NTA in panel A quantifies the concentration of MB-SDS aggregates at the MB concentration from 5.26 to 100 μM. The corresponding aggregate concentration increased from 4.91 ± 1.7 × 107 to 1.05 ± 0.12 × 1010 particles/mL. Panel B is the absorbance spectra of pure MB from 0.025 to 0.2 mM.

Materials and Methods

Reagents

MB (98%) was purchased from Fisher Scientific. SDS was purchased from Calbiochem. CTAB was purchased from Fluka. NaCl (≥99%) and SOS (>95%) were purchased from Sigma Aldrich. Laboratory polyethylene tubing (OD: 1.27 mm, ID: 0.85 mm) was purchased from Harvard Apparatus.

Preparation of Stock Solutions and High Order MB Aggregates

The MB stock solution was initially prepared at 2 M in Millipore water followed by filtration using a 0.22 μm filter. This solution was diluted as needed for each experiment. SDS, CTAB, NaCl, and SOS were prepared in Millipore water at 17.34 mM, 3 mM, 1 M, and 270 mM, respectively. MB dimer and high order aggregates were prepared by adding 25 μL of 2 mM MB in 975 μL of 1 and 3 M sodium sulfate at 40 °C, respectively.

Preparation of MB/SDS Complex

The SDS stock solution was diluted to 17.34, 8.67, 3.47, 1.73, and 0.87 mM. Next, 25 μL of 2 mM MB was added into 975 μL of each diluted SDS solution. For studies on the effect of SDS at high MB concentrations, 900 μL of 2 mM MB was added to 100 μL of 86.7, 34.7, 17.3, and 8.7

mM SDS, respectively. For studies on the effect of MB concentration, 20 µL of 0.125, 0.25, 0.5, 1.0, 2.0 mM MB were added into 180 µL of 3.47 mM SDS, respectively. MB-SDS solutions were maintained in water at final volumes of 1 mL.

Preparation of MB/CTAB and MB/NaCl Solution

CTAB was diluted to 3, 1.5, 1, 0.5, 0.25 mM. The MB/CTAB solution was prepared by adding 25 µL 2 mM MB into 975 µL of each diluted CTAB solution, respectively. To study the effect of NaCl, 2.5 mg of SDS was added to 25 µL of 2 mM MB followed by 975 µL of 0.8 M NaCl. In the control sample, 2.5 mg SDS was added to 25 µL of 2 mM MB followed by 975 µL of Millipore water.

Preparation of MB/SOS

SOS stock solution was diluted to 270, 135, 67.5, 33.75, and 16.8 mM. Next, 25 µL of 2 mM MB was added to 975 µL of each diluted SOS solution.

Absorbance and Photoacoustic Imaging Characterization

Absorbance spectra (400-850 nm) of these samples were characterized with a SpectraMax M5 spectrophotometer. The photoacoustic images of samples were obtained from a Vevo LAZR imaging system (Visualsonics). This photoacoustic imaging system is equipped with a 45±5 mJ tunable laser outlet for excitation and a 21 MHz-centered transducer for ultrasound signal reception. The tunable laser has a pulse of 4 to 6 ns at 20 Hz via a flashlamp pumped Q-switched Nd:YAG laser with an optical parameteric oscillator and second harmonic generator. The laser wavelength could be adjusted between 680 and 970 nm with a 1 nm step size. The ultrasound transducer had a 26-mm wide full field-of-view and acquired signals at 5 frames per second. The samples were prepared in polyethylene tubing fixed in a 3D-printed phantom holder[207] and aligned under the transducer at a depth of 11 mm for maximized laser exposure. The laser energy was optimized using the build-in energy power meter as well as an external power meter prior to measurements.

Nanoparticle Tracking Analysis

The nanoparticle tracking analysis uses MalvernTM Nanosight LM10. The system uses a 532 nm laser to excite the analyte in a liquid chamber. The camera records the scattered light from the analyte and measures the Brownian motion of the species to determine its size distribution and concentration using the Stokes-Einstein relation. The MB/SDS samples were injected into the system three times, and the system recorded 30-second videos of each injection for analysis.

Image processing and Statistical Treatment

Photoacoustic images were saved as TIFF files and quantified using ImageJ (1.48v)[191]. The RGB images were converted to 8-bit images. The photoacoustic intensity of each sample was measured over eight regions of interest (ROI) for statistical analysis. The mean and standard deviation were calculated using GraphPad Prism. Here, $p < 0.05$ was considered significant.

Appendix E: Supplementary Figures and Methods of Chapter 6

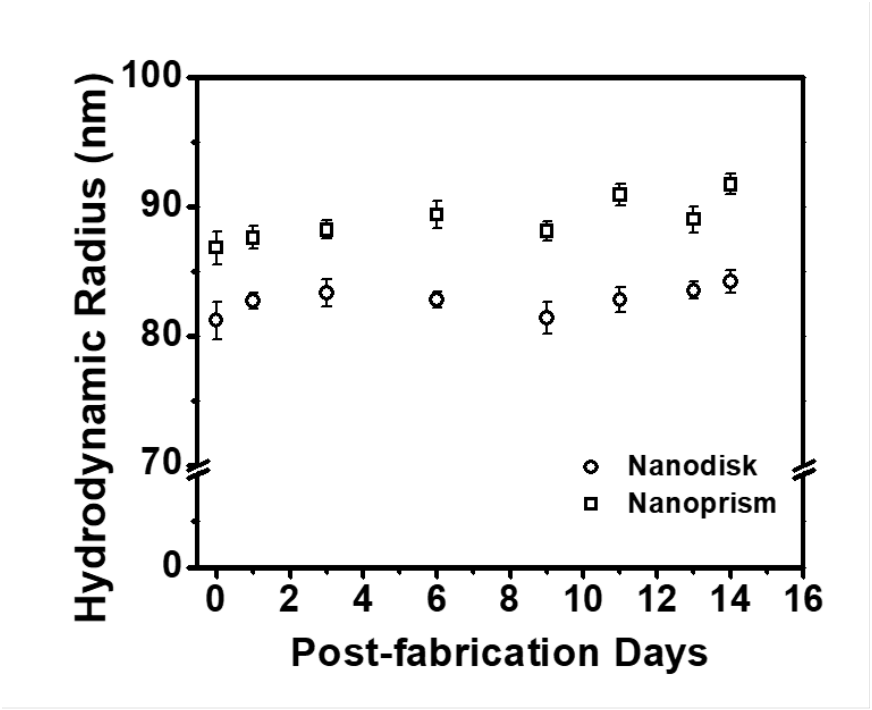

Supplementary Figure 5. 1 Colloidal stability of CuS nanodisk and nanoprism in PBS. PEGylated nanodisks and nanoprisms were stable in phosphate buffered saline (PBS) for at least 2 weeks.

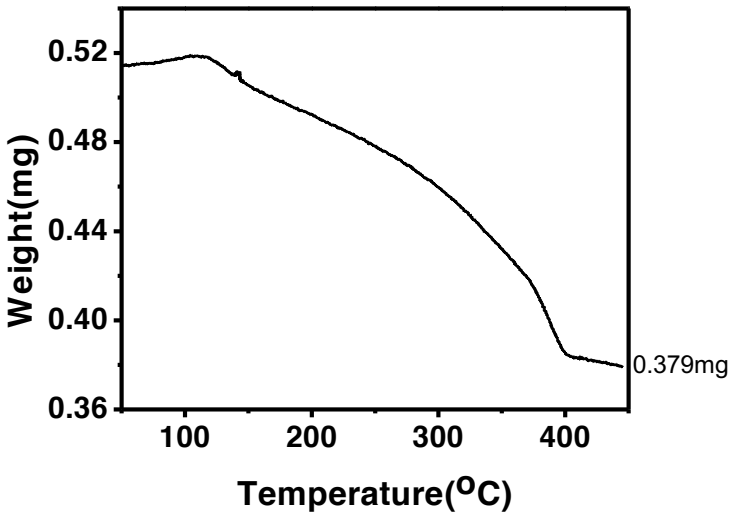

Supplementary Figure 5. 2 Thermal gravimetric analysis (TGA) measurement of CuS nanodisk. The TGA estimated the weight of solid material in the colloidal solution after removal of the ligand and the solvent. The weight of the CuS nanoparticle sample decreased from 0.513 to 0.379 mg when the evaporation temperature increased to 400°C.

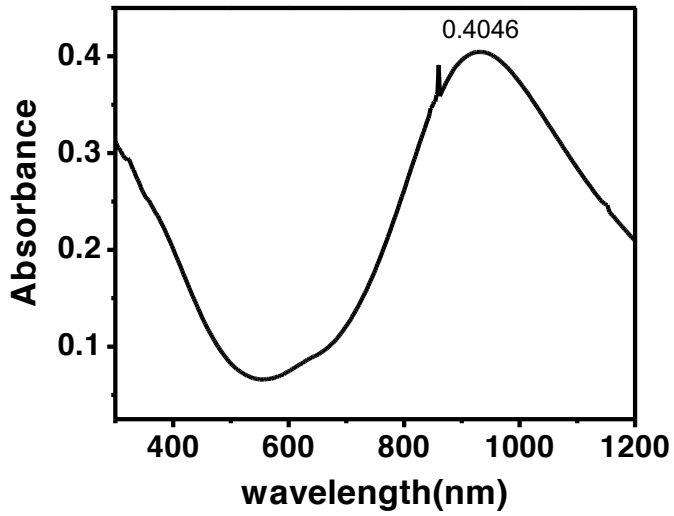

Supplementary Figure 5. 3 Extinction spectrum of CuS nanodisk colloidal solution. The peak absorbance intensity of the 200 times diluted TGA sample occurred was 0.4046.

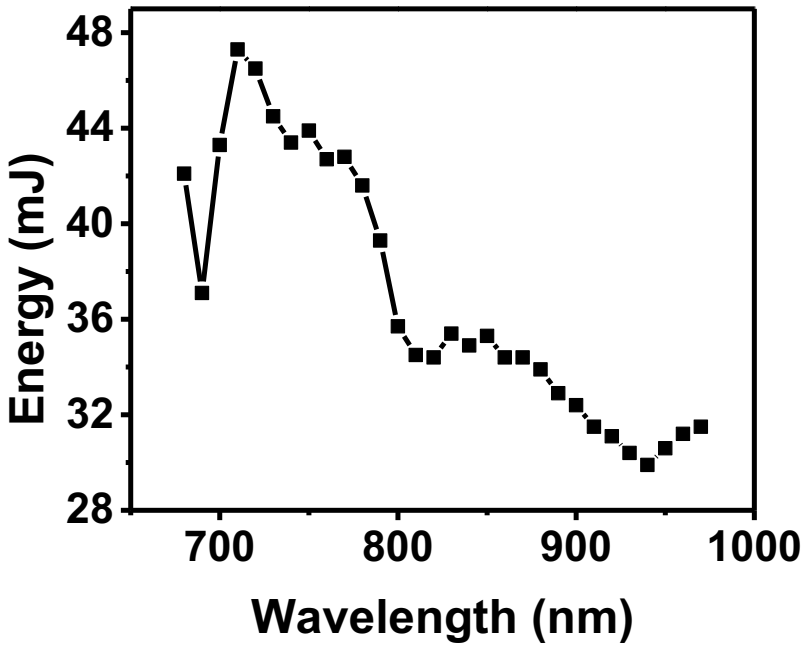

Supplementary Figure 5. 4 Laser output energy as a function of wavelength. The energy of the laser decreases from 47.3 mJ at 710 nm to 31.5 mJ at 970 nm.

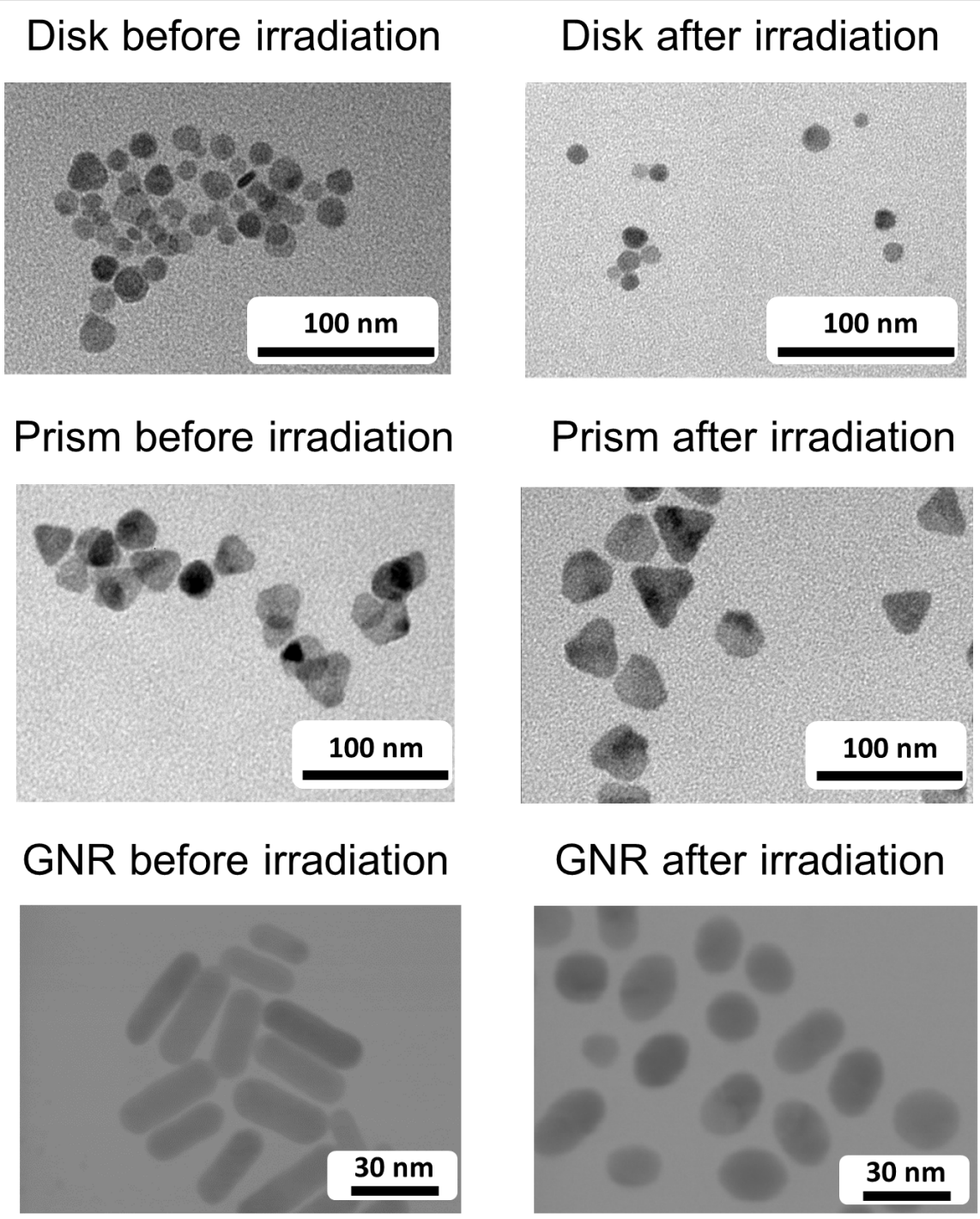

Supplementary Figure 5. 5 Structural stability characterization of gold nanorod, CuS nanodisk, and CuS nanoprism after laser irradiation. The structure of CuS nanodisk and nanoprism remained intact after being irradiated at 940 nm for 14 minutes, while the laser irradiation at 710 nm caused structural deformation on gold nanorod (GNR).

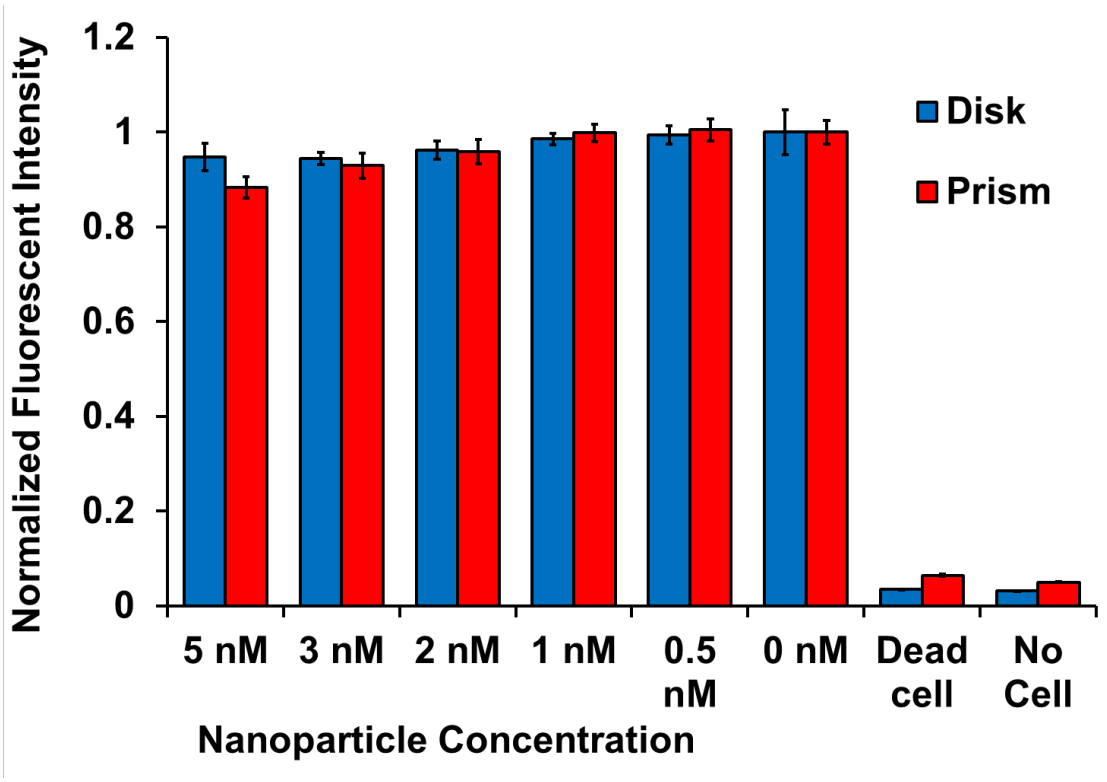

Supplementary Figure 5. 6 Cytotoxicity test of CuS nanodisk and nanoprism. The fluorescent intensity indicated that the viability of the OV2008 cancer cell was higher than 95% and 88% after incubating with 5 nM nanodisk and nanoprism for 24 hours, respectively. “Dead cell” and “No cell” indicate cells treated with 10% CTAB and an empty well, respectively.

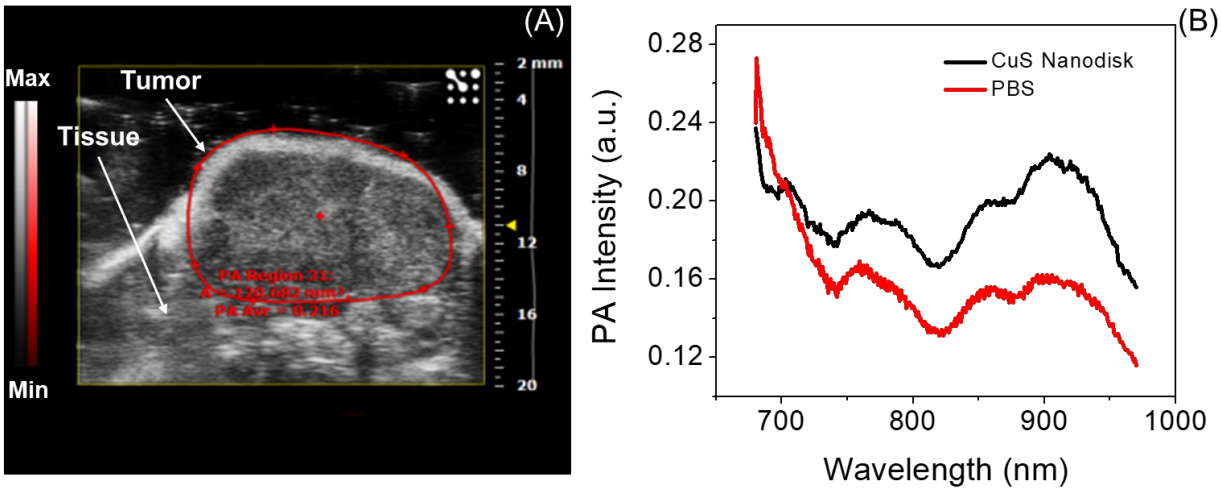

Supplementary Figure 5. 7 *in vivo* photoacoustic characterization of a subcutaneous ovarian tumor from a mouse that was intravenously treated with CuS and PBS. Panel A is the ultrasound image of an ovarian tumor in mouse showing the tumor and surrounding tissue based on differences in acoustic impedance. This same animal was intravenously injected with 200 µL of 50 nM CuS. The photoacoustic spectrum of the region of interest shows a characteristic peak at 920 nm, which is not present in the spectrum of the control tumor from the mouse treated with PBS.

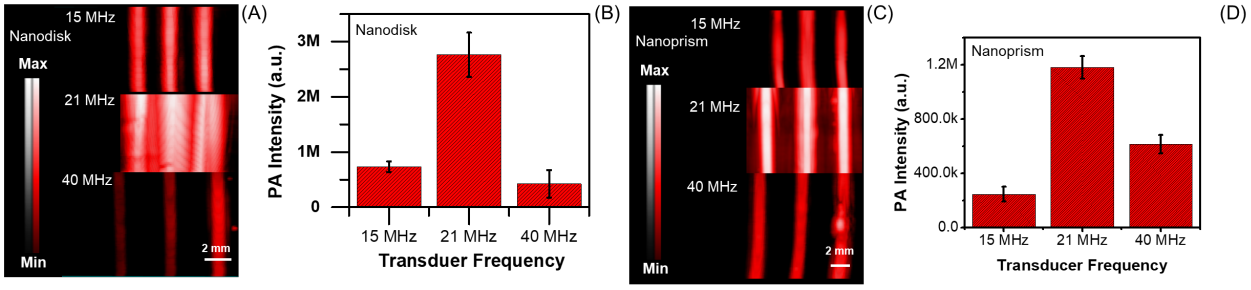

Supplementary Figure 5. 8 Photoacoustic intensity of CuS nanodisks and nanoprisms with transducers of different center frequencies. Panel A is the photoacoustic images of three replicate CuS nanodisk samples acquired by LZ201 (center frequency=15 MHz), LZ250 (center frequency=21 MHz), and LZ550 (center frequency=40 MHz). The quantitative analysis of the photoacoustic intensity is shown in panel B. The photoacoustic image and data analysis of CuS nanpoprism acquired under the same experimental conditions are shown in panel C and panel D, respectively.

Material and Methods:

Chemicals

Copper nitrate ($Cu(NO_3)_2 \cdot 2.5H_2O$) and chloroform were purchased from Fisher. Copper(II) chloride (97%), oleylamine (70%), 1-octadecene(90%), sulfur powder (99.99%), and copper ICP standard were purchased from Sigma-Aldrich. Ethanol (200 proof) was purchased form Goldshield Chemical. Poly(ethylene glycol) methyl ether thiol (PEG-thiol, Mw=5000) was purchased from Laysan Bio. Dulbecco's modified eagle medium (DMEM), fetal bovine serum, antibiotic-antimycotic (100X), and AlamarBlue® assay were purchased from Thermo Fisher Scientific. The internal standard for ICP was purchased from Inorganic Ventures. The nitric acid (70%) and hydrochloric acid (36.5-38%) was purchased from Fisher Scientific and J.T. Baker, respectively. Laboratory polyethylene tubing (OD: 1.27 mm, ID: 0.85 mm) was purchased from Harvard Apparatus, and 0.2 μm polyethersulfone syringe filters (Puradisc 25AS) were purchased from Whatman.

CuS nanodisks by solvent-based synthesis

The nanodisks were prepared as previously described[174, 175] with minor adjustments. A 0.4 M copper nitrate solution was prepared by dissolving 0.0928 g copper nitrate (0.4 mmol) in 4 mL mixture solvent of oleylamine/1-octadecene (volume ratio of 1:3). Then, 0.0096 g (0.3 mmol) sulfur powder was added to the dark blue copper nitrate solution with stirring for 5 minutes. Next,

the solution was placed in an oil bath at 180^{o}C, and the solution color turned dark green/blue. The solution was cooled to room temperature to purify the nanodisks. Here, 4 mL ethanol was added to the as-made nanodisk solution, and the solution was centrifuged at 3000 rpm for 5 minutes to remove free oleylamine and 1-octadecene. The pellet was resuspended in chloroform and centrifuged at 7500 rpm for 7.5 minutes to remove any byproducts.

Shape focusing of triangular nanoprisms by seed-mediated growth

The seeds were prepared by adding 0.2 mmol copper (II) chloride and 0.3 mmol sulfur powder in a mixed solvent of 1 mL oleylamine and 3 mL 1-octadecene at 140 ^{o}C for 45 minutes. Next, 10% CuS seed solution (after purification to remove free oleylamine and byproducts) dispersed in 1-octadecene was added to the growth solution prepared by dissolving 0.05 mmol copper (II) chloride and 0.075 mmol sulfur powder in a mixed solvent (i.e. 0.25 mL oleylamine with 3.75 mL1-octadecene). The seed/growth mixed solution was placed in a 120°C oil bath for 75 minutes. After the bright-blue solution turned dark green-blue, the solution was cooled to room temperature. Then, 4 mL ethanol was added into the solution, and the solution was centrifuged at 3000 rpm for 5 minutes to remove the free oleylamine and 1-octadecene. The pellet was resuspended in chloroform and centrifuged at 7500 rpm for 7.5 minutes to remove any byproducts. These CuS nanoparticles were used as “new seeds”, and the synthesis process was repeated until the CuS nanocrystal grew to be the triangular nanoprism.

Surface modification of CuS nanodisks/nanoprisms

4 mL of oleylamine coated CuS nanodisks (or nanoprisms) in colloidal solution (in chloroform) was mixed with 1 mL 0.2 mM poly(ethylene glycol) methyl ether thiol (PEG-thiol, MW=5000) in a mixed solvent of chloroform/ethanol (volume ratio=1:1) and incubated at room temperature for 24 hours. The PEGylated nanodisks (or nanoprisms) were collected by centrifugation at 14,800 rpm for 45-60 minutes. The precipitation was resuspended in DI water and centrifuged at 14,800 rpm for 45-60 minutes to remove the free PEG-thiol twice; finally, the PEGylated nanodisks (or nanoprisms) were eventually dispersed in DI water or PBS solution.

Size measurement using transmission electron microscopy (TEM), atomic force microscopy (AFM), and dynamic light scattering (DLS)

The as-synthesized nanodisk and nanoprism were dispersed in chloroform and were incompatible with the carbon support film on commercial TEM grids. Therefore, we deposited the nanodisk or nanoprism solution onto air-water interface to evaporate the chloroform before transferring the nanoparticles to a TEM grid. The PEG-thiol coated nanodisks and nanoprisms dispersed in PBS solution were directly dripped onto the TEM grids. The TEM grids were kept in a vacutainer for at least 30 minutes to evaporate the water prior to TEM (JEOL 1200 EX II). The thickness of nanodisk was measured by TEM due to particle assemble by face-to-face interaction into larger nanostructure. The thickness of nanoprisms was measure by AFM.

The PEGylated nanodisks/nanoprisms were dissolved in deionized water for DLS (Malvern, Nano-ZS) measurements. Stability characterization used the same PEGylated nanodisks and nanoprisms and measured them every 2-3 days for 14 days.

CuS Thermogravimetric Analysis.

The molar extinction coefficient of the CuS nanocrystal in the CuS colloidal solution was calculated via the results from thermal gravimetric analysis (TGA, Perkin-Elmer TGA7) and the extinction spectrum of the CuS colloidal solution. 0.172 μL CuS nanodisk dispersed in chloroform was heated to 400 ℃ under a nitrogen atmosphere resulting in bare CuS nanodisks. The concentration of the particle was calculated based on the resulted mass, density of CuS, size of the particles (i.e. width and thickness), and the absorbance of the sample at 1145 nm.

Absorbance and Photoacoustic Imaging Characterization

The absorbance spectra (700-1200 nm) of the nanodisks and nanoprisms dispersed in chloroform were collected with a PerkinElmer Lambda 1050 spectrophotometer. The photoacoustic intensity and spectra of these samples were obtained via a Vevo LAZR imaging system (Visualsonics). The photoacoustic imaging system consists of a 21 MHz-centered transducer (bandwidth: 13-24 MHz) and a flashlamp pumped Q-switched Nd:YAG laser with an

optical parametric oscillator and second harmonic generator. The system generates laser pulses (4-6 ns, 20Hz, 45±5 mJ, tunable wavelength 680-970 nm) and acquires acoustic waves induced by thermal expansion. The nanodisks/nanoprisms samples were injected in the polyethylene tubing fixed in a customized holder[207] and placed horizontally 10 mm under the transducer for maximized laser exposure. The photoacoustic images were acquired using the LZ250 transducer (21 MHz, bandwidth: 13-24 MHz) because it provided higher photoacoustic signal of the CuS nanoparticles than LZ201 (15 MHz, bandwidth: 9-18 MHz) and LZ550 (40 MHz, bandwidth: 32-55 MHz) (**Supplementary Figure 5.8**). The full field-of-view of the photoacoustic images is 26 x 15 mm. The CuS nanodisk and nanoprism-treated ovarian tumors were imbedded in 1 wt.% agarose gel phantoms in a petri dish. For *in vivo* imaging confirmation, the mouse was imaged after the intravenous injection of 200 µL of 50 nM CuS nanodisk or PBS. The photoacoustic images were reconstructed using a maximum intensity projection, and the photoacoustic signal of the tumor volume was quantified using ImageJ [191].

Cell Culture and Cytotoxicity Studies

Human OV 2008 human ovarian cancer cells were acquired from ATCC and cultured in DMEM medium that contained 5% antibiotic-antimycotic and 10% fetal bovine serum. The cells were passaged 3 times prior to cytotoxicity test or tumor implantation. We seeded the cells in a 96 well plate at 10,000 cells per well and analyzed the wells in replicates (n=8). 100 µL nanodisk or nanoprism (5, 3, 2, 1, 0.5 nM) dissolved in cell culture medium, pure cell culture medium (0 nM), or 10% CTAB (dead cells, positive control) was incubated with the cells for 24 hours. After removing the medium and washing the cells with PBS for 3 times, the cells were treated with the alamarBlue® reagent (10% in cell culture medium) for 4 hours. The cell viability was determined by fluorescent measurement at 550 nm excitation and 580 nm emission.

Animal Studies

All animal work was conducted in accordance with the administrative panel of Animal Care Program of the University of California San Diego. The 6-week old female nude mice were

randomly divided into 8 experimental groups. To implant the tumors in the mice, 5-10 million human 2008 ovarian cells mixed with 100 µL growth factor reduced Matrigel were subcutaneously injected into the hind limb of a mouse. When the tumor grew to ~1.0 cm long, 200 µL of 20 nM CuS nanodisk or nanoprism prepared in PBS was injected into the tail vein of a mouse. The groups were studied at 1, 2, 4, or 8 hours (n = 4 mice per group). The total number of mice for the CuS nanodisk and nanoprism treatment groups was 32 (4 groups x 4 animals/group x 2 nanoparticle types). After incubation for 1, 2, 4, or 8 hours, 0.5-1 mL blood was collected via cardiac puncture, and the tumor was excised for ICP-MS analysis and photoacoustic imaging. Three sets of blood and tumor samples from mice without any treatment were used as the negative control to determine baseline concentrations. The photoacoustic spectrum was normalized via dividing each intensity value by the maximum intensity value of the spectrum.

Measurement of Copper Concentration in Blood and Tumor

The copper concentrations in blood and tumors were measured by ICP-MS (iCAP RQ ICP-MS, Thermo Fisher Scientific, Waltham, MA, USA). All samples were weighed and added to Teflon vessels. The samples were spiked with the internal standard solution and then digested in 10 mL of *aqua regia* using a MARS 6 microwave digestion system (CEM Corporation, Matthews, NC). The program used included the following: (1) 45-minute ramp to 150 ^{o}C, (2) 45-minute hold, (3) 30-minute cooling ramp to 50 ^{o}C, (4) 45-minute ramp to 195 ^{o}C, (5) 45 minutes of hold, and (6) a 25-minute cooling ramp to 30 ^{o}C. After the digestion was complete, all the samples were transferred into volumetric flask (25 mL) and allowed to degas under the fume hood for 30 minutes and then diluted to 25 mL using milliQ water. The digested samples were filtered with 0.2 µm polyethersulfone syringe filters. A final 1:10 dilution was carried out with 2% nitric acid. ICP-MS analysis was carried out for Cu using copper standard solutions (0, 1, 2, 5, 10, 20, 50, 100 ppb). All samples were analyzed in triplicate.

Data Analysis and Statistical Treatment.

The average and standard deviation of the integrated density were calculated using Microsoft excel functions “AVERAGE” and “STDEV”. The p-value was calculated via the two-tailed test using the Microsoft excel function, “TTEST”.

References

1. Bell, A. G., The production of sound by radiant energy. *Science* **1881,** *2* (48), 242-253.

2. Beard, P., Biomedical photoacoustic imaging. *Interface focus* **2011,** *1* (4), 602-631.

3. Xu, M.; Wang, L. V., Photoacoustic imaging in biomedicine. *Review of scientific instruments* **2006,** *77* (4), 041101.

4. Oraevsky, A.; Karabutov, A., Biomedical photonics handbook. *Optoacoustic Tomography", CRC Press, Boca Raton-London-New York-Washington, DC* **2003,** *34*, 31-34.

5. Wang, L. V.; Hu, S., Photoacoustic Tomography: In Vivo Imaging from Organelles to Organs. *Science* **2012,** *335* (6075), 1458-1462.

6. Li, L.; Zhu, L.; Ma, C.; Lin, L.; Yao, J.; Wang, L.; Maslov, K.; Zhang, R.; Chen, W.; Shi, J., Single-impulse panoramic photoacoustic computed tomography of small-animal whole-body dynamics at high spatiotemporal resolution. *Nature biomedical engineering* **2017,** *1* (5), 0071.

7. Deán-Ben, X. L.; Fehm, T. F.; Ford, S. J.; Gottschalk, S.; Razansky, D., Spiral volumetric optoacoustic tomography visualizes multi-scale dynamics in mice. *Light: Science &Amp; Applications* **2017,** *6*, e16247.

8. Lin, L.; Hu, P.; Shi, J.; Appleton, C. M.; Maslov, K.; Li, L.; Zhang, R.; Wang, L. V., Single-breath-hold photoacoustic computed tomography of the breast. *Nature communications* **2018,** *9* (1), 2352.

9. Sehgal, C. M.; Greenleaf, J. F., Scattering of ultrasound by tissues. *Ultrasonic Imaging* **1984,** *6* (1), 60-80.

10. Yao, J.; Wang, L. V., Photoacoustic Microscopy. *Laser & photonics reviews* **2013,** *7*(5), 758-778.

11. Zhang, C.; Maslov, K.; Wang, L. V., Subwavelength-resolution label-free photoacoustic microscopy of optical absorption in vivo. *Opt. Lett.* **2010,** *35* (19), 3195-3197.

12. Yao, D.-K.; Maslov, K.; Shung, K. K.; Zhou, Q.; Wang, L. V., In vivo label-free photoacoustic microscopy of cell nuclei by excitation of DNA and RNA. *Opt. Lett.* **2010,** *35* (24), 4139-4141.

13. Jiao, S.; Jiang, M.; Hu, J.; Fawzi, A.; Zhou, Q.; Shung, K. K.; Puliafito, C. A.; Zhang, H. F., Photoacoustic ophthalmoscopy for in vivo retinal imaging. *Opt. Express* **2010,** *18* (4), 3967-3972.

14. Salehi, H. S.; Kumavor, P. D.; Li, H.; Alqasemi, U.; Wang, T.; Xu, C.; Zhu, Q., Design of optimal light delivery system for co-registered transvaginal ultrasound and photoacoustic imaging of ovarian tissue. *Photoacoustics* **2015,** *3* (3), 114-122.

15. Wang, B.; Su, J. L.; Karpiouk, A. B.; Sokolov, K. V.; Smalling, R. W.; Emelianov, S. Y., Intravascular Photoacoustic Imaging. *IEEE journal of quantum electronics* **2010,** *16* (3), 588-599.

16. Jansen, K.; van Soest, G.; van der Steen, A. F. W., Intravascular Photoacoustic Imaging: A New Tool for Vulnerable Plaque Identification. *Ultrasound in Medicine & Biology* **2014,** *40* (6), 1037-1048.

17. Galanzha, E. I.; Zharov, V. P., Photoacoustic flow cytometry. *Methods* **2012,** *57* (3), 280-296.

18. Nedosekin, D. A.; Fahmi, T.; Nima, Z. A.; Nolan, J.; Cai, C.; Sarimollaoglu, M.; Dervishi, E.; Basnakian, A.; Biris, A. S.; Zharov, V. P., Photoacoustic flow cytometry for nanomaterial research. *Photoacoustics* **2017,** *6*, 16-25.

19. Brunker, J.; Beard, P., Pulsed photoacoustic Doppler flowmetry using time-domain cross-correlation: Accuracy, resolution and scalability. *The Journal of the Acoustical Society of America* **2012,** *132* (3), 1780-1791.

20. Brunker, J.; Beard, P., *Pulsed photoacoustic Doppler flowmetry using a cross correlation method*. SPIE: **2010**; Vol. 7564.

21. Yao, J.; Ke, H.; Tai, S.; Zhou, Y.; Wang, L. V., Absolute photoacoustic thermometry in deep tissue. *Opt. Lett.* **2013,** *38* (24), 5228-5231.

22. Hu, S.; Maslov, K.; Wang, L. V., Second-generation optical-resolution photoacoustic microscopy with improved sensitivity and speed. *Opt. Lett.* **2011,** *36* (7), 1134-1136.

23. Jansen, K.; van der Steen, A. F. W.; van Beusekom, H. M. M.; Oosterhuis, J. W.; van Soest, G., Intravascular photoacoustic imaging of human coronary atherosclerosis. *Opt. Lett.* **2011,** *36* (5), 597-599.

24. He, Y.; Wang, L.; Shi, J.; Yao, J.; Li, L.; Zhang, R.; Huang, C.-H.; Zou, J.; Wang, L. V., In vivo label-free photoacoustic flow cytography and on-the-spot laser killing of single circulating melanoma cells. *Scientific reports* **2016,** *6*, 39616.

25. Alkilany, A. M.; Murphy, C. J., Toxicity and cellular uptake of gold nanoparticles: what we have learned so far? *Journal of nanoparticle research : an interdisciplinary forum for nanoscale science and technology* **2010,** *12* (7), 2313-2333.

26. Li, W.; Chen, X., Gold nanoparticles for photoacoustic imaging. *Nanomedicine (London, England)* **2015,** *10* (2), 299-320.

27. Huang, X.; El-Sayed, M. A., Gold nanoparticles: Optical properties and implementations in cancer diagnosis and photothermal therapy. *Journal of Advanced Research* **2010,** *1* (1), 13-28.

28. Bayer, C. L.; Chen, Y.-S.; Kim, S.; Mallidi, S.; Sokolov, K.; Emelianov, S., Multiplex photoacoustic molecular imaging using targeted silica-coated gold nanorods. *Biomed. Opt. Express* **2011,** *2* (7), 1828-1835.

29. Cheng, L.; Liu, J.; Gu, X.; Gong, H.; Shi, X.; Liu, T.; Wang, C.; Wang, X.; Liu, G.; Xing, H.; Bu, W.; Sun, B.; Liu, Z., PEGylated WS2 Nanosheets as a Multifunctional Theranostic Agent for in vivo Dual-Modal CT/Photoacoustic Imaging Guided Photothermal Therapy. *Adv Mater* **2014,** *26* (12), 1886-1893.

30. Xie, L.; Wang, G.; Zhou, H.; Zhang, F.; Guo, Z.; Liu, C.; Zhang, X.; Zhu, L., Functional long circulating single walled carbon nanotubes for fluorescent/photoacoustic imaging-guided enhanced phototherapy. *Biomaterials* **2016,** *103*, 219-228.

31. De La Zerda, A.; Zavaleta, C.; Keren, S.; Vaithilingam, S.; Bodapati, S.; Liu, Z.; Levi, J.; Smith, B. R.; Ma, T.-J.; Oralkan, O., Carbon nanotubes as photoacoustic molecular imaging agents in living mice. *Nature nanotechnology* **2008,** *3* (9), 557.

32. Fu, Q.; Zhu, R.; Song, J.; Yang, H.; Chen, X., Photoacoustic Imaging: Contrast Agents and Their Biomedical Applications. *Adv Mater* **2019,** *31* (6), 1805875.

33. Erpelding, T. N.; Kim, C.; Pramanik, M.; Jankovic, L.; Maslov, K.; Guo, Z.; Margenthaler, J. A.; Pashley, M. D.; Wang, L. V., Sentinel lymph nodes in the rat: noninvasive photoacoustic and US imaging with a clinical US system. *Radiology* **2010,** *256* (1), 102-110.

34. Schirmer, R. H.; Adler, H.; Pickhardt, M.; Mandelkow, E., "Lest we forget you — methylene blue …". *Neurobiology of Aging* **2011,** *32* (12), 2325-e7.

35. Peter, C.; Hongwan, D.; Küpfer, A.; Lauterburg, B., Pharmacokinetics and organ distribution of intravenous and oral methylene blue. *European journal of clinical pharmacology* **2000,** *56* (3), 247-250.

36. Yin, C.; Wen, G.; Liu, C.; Yang, B.; Lin, S.; Huang, J.; Zhao, P.; Wong, S. H. D.; Zhang, K.; Chen, X.; Li, G.; Jiang, X.; Huang, J.; Pu, K.; Wang, L.; Bian, L., Organic Semiconducting Polymer Nanoparticles for Photoacoustic Labeling and Tracking of Stem Cells in the Second Near-Infrared Window. *ACS nano* **2018,** *12* (12), 12201-12211.

37. Lyu, Y.; Zeng, J.; Jiang, Y.; Zhen, X.; Wang, T.; Qiu, S.; Lou, X.; Gao, M.; Pu, K., Enhancing Both Biodegradability and Efficacy of Semiconducting Polymer Nanoparticles for Photoacoustic Imaging and Photothermal Therapy. *ACS nano* **2018,** *12* (2), 1801-1810.

38. Hirsh, J.; Anand, S. S.; Halperin, J. L.; Fuster, V.; American Heart, A., Guide to anticoagulant therapy: Heparin : a statement for healthcare professionals from the American Heart Association. *Circulation* **2001,** *103* (24), 2994-3018.

39. Monagle, P.; Chan, A. K.; Goldenberg, N. A.; Ichord, R. N.; Journeycake, J. M.; Nowak-Gottl, U.; Vesely, S. K.; American College of Chest, P., Antithrombotic therapy in neonates and children: Antithrombotic Therapy and Prevention of Thrombosis, 9th ed: American College of Chest Physicians Evidence-Based Clinical Practice Guidelines. *Chest* **2012,** *141* (2 Suppl), e737S-801S.

40. Newall, F.; Johnston, L.; Ignjatovic, V.; Monagle, P., Unfractionated heparin therapy in infants and children. *Pediatrics* **2009,** *123* (3), e510-8.

41. Cook, S.; Walker, A.; Hügli, O.; Togni, M.; Meier, B., Percutaneous coronary interventions in Europe. *Clinical Research in Cardiology* **2007,** *96* (6), 375-382.

42. Ţintoiu, I. C.; Underwood, M. J.; Cook, S. P.; Kitabata, H.; Abbas, A., *Coronary Graft Failure: State of the Art*. Springer: **2016**.

43. Pasquali, S. K.; Li, J. S.; Burstein, D. S.; Sheng, S.; O'Brien, S. M.; Jacobs, M. L.; Jaquiss, R. D.; Peterson, E. D.; Gaynor, J. W.; Jacobs, J. P., Association of center volume with mortality and complications in pediatric heart surgery. *Pediatrics* **2012,** *129* (2), e370-6.

44. Maslach-Hubbard, A.; Bratton, S. L., Extracorporeal membrane oxygenation for pediatric respiratory failure: History, development and current status. *World journal of critical care medicine* **2013,** *2* (4), 29-39.

45. Goldenberg, N. A., Pediatric Thrombotic Disorders. **2015**.

46. Buchanan, M. R.; Ofosu, F. A.; Brister, S. J., *ThrombinIts Key Role in Thrombogenesis-Implications for Its Inhibition*. CRC Press: **1994**.

47. Rosenberg, R. D., Role of heparin and heparinlike molecules in thrombosis and atherosclerosis. *Federation proceedings* **1985,** *44* (2), 404-9.

48. Wahr, J. A.; Shore, A. D.; Harris, L. H.; Rogers, P.; Panesar, S.; Matthew, L.; Pronovost, P. J.; Cleary, K.; Pham, J. C., Comparison of intensive care unit medication errors reported to the United States' MedMarx and the United Kingdom's National Reporting and Learning System: a cross-sectional study. *American journal of medical quality : the official journal of the American College of Medical Quality* **2014,** *29* (1), 61-9.

49. Grissinger, M. C.; Hicks, R. W.; Keroack, M. A.; Marella, W. M.; Vaida, A. J., Harmful medication errors involving unfractionated and low-molecular-weight heparin in three patient safety reporting programs. *Joint Commission journal on quality and patient safety / Joint Commission Resources* **2010,** *36* (5), 195-202.

50. Kaushal, R.; Bates, D. W.; Landrigan, C.; McKenna, K. J.; Clapp, M. D.; Federico, F.; Goldmann, D. A., Medication errors and adverse drug events in pediatric inpatients. *Jama* **2001,** *285* (16), 2114-20.

51. Arimura, J.; Poole, R. L.; Jeng, M.; Rhine, W.; Sharek, P., Neonatal heparin overdose-a multidisciplinary team approach to medication error prevention. *The journal of pediatric pharmacology and therapeutics : JPPT : the official journal of PPAG* **2008,** *13* (2), 96-8.

52. Raschke, R. A.; Reilly, B. M.; Guidry, J. R.; Fontana, J. R.; Srinivas, S., The weight-based heparin dosing nomogram compared with a "standard care" nomogram. A randomized controlled trial. *Annals of internal medicine* **1993,** *119* (9), 874-81.

53. Key, N.; Makris, M.; O'Shaughnessy, D.; Lillicrap, D., *Practical hemostasis and thrombosis*. Wiley Online Library: **2009**.

54. Liveris, A.; Bello, R. A.; Friedmann, P.; Duffy, M. A.; Manwani, D.; Killinger, J. S.; Rodriquez, D.; Weinstein, S., Anti-Factor Xa Assay Is a Superior Correlate of Heparin Dose Than Activated Partial Thromboplastin Time or Activated Clotting Time in Pediatric Extracorporeal Membrane Oxygenation*. *Pediatric Critical Care Medicine* **2014,** *15* (2), e72-e79.

55. Lang, T.; von Depka, M., Diagnostische Möglichkeiten und Grenzen der Thrombelastometrie/-graphie. *Hämostaseologie* **2006,** *26* (5), 20-29.

56. Nichols, J. H.; Christenson, R. H.; Clarke, W.; Gronowski, A.; Hammett-Stabler, C. A.; Jacobs, E.; Kazmierczak, S.; Lewandrowski, K.; Price, C.; Sacks, D. B., Executive summary. The National Academy of Clinical Biochemistry Laboratory Medicine Practice Guideline: evidence-based practice for point-of-care testing. *Clinica chimica acta* **2007,** *379* (1), 14-28.

57. Gertler, R.; Wiesner, G.; Tassani-Prell, P.; Braun, S.-L.; Martin, K., Are the point-of-care diagnostics MULTIPLATE and ROTEM valid in the setting of high concentrations of heparin and its reversal with protamine? *Journal of cardiothoracic and vascular anesthesia* **2011,** *25* (6), 981-986.

58. Zhang, H. F.; Maslov, K.; Sivaramakrishnan, M.; Stoica, G.; Wang, L. H. V., Imaging of hemoglobin oxygen saturation variations in single vessels in vivo using photoacoustic microscopy. *Applied Physics Letters* **2007,** *90* (5).

59. Zhang, H. F.; Maslov, K.; Stoica, G.; Wang, L. V., Functional photoacoustic microscopy for high-resolution and noninvasive in vivo imaging. *Nature biotechnology* **2006,** *24* (7), 848-51.

60. Luke, G. P.; Yeager, D.; Emelianov, S. Y., Biomedical applications of photoacoustic imaging with exogenous contrast agents. *Annals of biomedical engineering* **2012,** *40* (2), 422-37.

61. Huynh, E.; Lovell, J. F.; Helfield, B. L.; Jeon, M.; Kim, C.; Goertz, D. E.; Wilson, B. C.; Zheng, G., Porphyrin Shell Microbubbles with Intrinsic Ultrasound and Photoacoustic Properties. *Journal of the American Chemical Society* **2012,** *134* (40), 16464-16467.

62. Song, K. H.; Stein, E. W.; Margenthaler, J. A.; Wang, L. V., Noninvasive photoacoustic identification of sentinel lymph nodes containing methylene blue in vivo in a rat model. *J. Biomed. Opt.* **2008,** *13* (5), 054033-054033-6.

63. Erpelding, T. N.; Kim, C.; Pramanik, M.; Jankovic, L.; Maslov, K.; Guo, Z.; Margenthaler, J. A.; Pashley, M. D.; Wang, L. V., Sentinel lymph nodes in the rat: noninvasive photoacoustic and US imaging with a clinical US system 1. *Radiology* **2010,** *256* (1), 102-110.

64. Lovell, J. F.; Jin, C. S.; Huynh, E.; Jin, H.; Kim, C.; Rubinstein, J. L.; Chan, W. C. W.; Cao, W.; Wang, L. V.; Zheng, G., Porphysome nanovesicles generated by porphyrin bilayers for use as multimodal biophotonic contrast agents. *Nat Mater* **2011,** *10* (4), 324-332.

65. Zerda, A. d. l.; Liu, Z.; Bodapati, S.; Teed, R.; Vaithilingam, S.; Khuri-Yakub, B. T.; Chen, X.; Dai, H.; Gambhir, S. S., Ultrahigh Sensitivity Carbon Nanotube Agents for Photoacoustic Molecular Imaging in Living Mice. *Nano Letters* **2010,** *10* (6), 2168-2172.

66. Pu, K.; Shuhendler, A. J.; Jokerst, J. V.; Mei, J.; Gambhir, S. S.; Bao, Z.; Rao, J., Semiconducting polymer nanoparticles as photoacoustic molecular imaging probes in living mice. *Nature nanotechnology* **2014,** *9* (3), 233-239.

67. Weber, J.; Beard, P. C.; Bohndiek, S. E., Contrast agents for molecular photoacoustic imaging. *Nat Meth* **2016,** *13* (8), 639-650.

68. Cash, K. J.; Li, C.; Xia, J.; Wang, L. V.; Clark, H. A., Optical Drug Monitoring: Photoacoustic Imaging of Nanosensors to Monitor Therapeutic Lithium in Vivo. *ACS nano* **2015,** *9* (2), 1692-1698.

69. Juratli, M. A.; Menyaev, Y. A.; Sarimollaoglu, M.; Siegel, E. R.; Nedosekin, D. A.; Suen, J. Y.; Melerzanov, A. V.; Juratli, T. A.; Galanzha, E. I.; Zharov, V. P., Real-Time Label-Free Embolus Detection Using In Vivo Photoacoustic Flow Cytometry. *PloS one* **2016,** *11* (5), e0156269.

70. Zhong, Z.; Anslyn, E. V., A Colorimetric Sensing Ensemble for Heparin. *Journal of the American Chemical Society* **2002,** *124* (31), 9014-9015.

71. Cao, R.; Li, B., A simple and sensitive method for visual detection of heparin using positively-charged gold nanoparticles as colorimetric probes. *Chemical communications* **2011,** *47* (10), 2865-7.

72. Fu, X.; Chen, L.; Li, J.; Lin, M.; You, H.; Wang, W., Label-free colorimetric sensor for ultrasensitive detection of heparin based on color quenching of gold nanorods by graphene oxide. *Biosensors & bioelectronics* **2012,** *34* (1), 227-31.

73. Cai, L.; Zhan, R.; Pu, K.-Y.; Qi, X.; Zhang, H.; Huang, W.; Liu, B., Butterfly-Shaped Conjugated Oligoelectrolyte/Graphene Oxide Integrated Assay for Light-Up Visual Detection of Heparin. *Analytical Chemistry* **2011,** *83* (20), 7849-7855.

74. Fu, X.; Chen, L.; Li, J., Ultrasensitive colorimetric detection of heparin based on self-assembly of gold nanoparticles on graphene oxide. *The Analyst* **2012,** *137* (16), 3653-3658.

75. Simmons, R.; Thevarajah, S.; Brennan, M. B.; Christos, P.; Osborne, M., Methylene blue dye as an alternative to isosulfan blue dye for sentinel lymph node localization. *Annals of Surgical Oncology* **2003,** *10* (3), 242-247.

76. Butch, A. W., Dilution protocols for detection of hook effects/prozone phenomenon. *Clinical chemistry* **2000,** *46* (10), 1719-1720.

77. Lowary, L. R.; Smith, F. A.; Coyne, E.; Dunham, N. W., Comparative neutralization of lung- and mucosal-derived heparin by protamine sulfate using in vitro and in vivo methods. *Journal of pharmaceutical sciences* **1971,** *60* (4), 638-640.

78. Luo, H. Q.; Liu, S. P.; Liu, Z. F.; Liu, Q.; Li, N. B., Resonance Rayleigh scattering spectra for studying the interaction of heparin with some basic phenothiazine dyes and their analytical applications. *Analytica Chimica Acta* **2001,** *449* (1–2), 261-270.

79. Chen, Y.-S.; Frey, W.; Kim, S.; Kruizinga, P.; Homan, K.; Emelianov, S., Silica-Coated Gold Nanorods as Photoacoustic Signal Nanoamplifiers. *Nano Letters* **2011,** *11* (2), 348-354.

80. Kuhle, S.; Eulmesekian, P.; Kavanagh, B.; Massicotte, P.; Vegh, P.; Lau, A.; Mitchell, L. G., Lack of correlation between heparin dose and standard clinical monitoring tests in treatment with unfractionated heparin in critically III children. *Haematologica* **2007,** *92* (4), 554-557.

81. Boneu, B.; de Moerloose, P., *How and when to monitor a patient treated with low molecular weight heparin*, Seminars in thrombosis and hemostasis, **2001**, *27* (5), 519-522.

82. Barrowcliffe, T. W., LOW MOLECULAR WEIGHT HEPARIN(S). *British Journal of Haematology* **1995,** *90* (1), 1-7.

83. Gould, M. K.; Dembitzer, A. D.; Doyle, R. L.; Hastie, T. J.; Garber, A. M., Low-molecular-weight heparins compared with unfractionated heparin for treatment of acute deep venous thrombosis. A meta-analysis of randomized, controlled trials. *Annals of internal medicine* **1999,** *130* (10), 800-9.

84. Randomised controlled trial of subcutaneous calcium-heparin in acute myocardial infarction. The SCATI (Studio sulla Calciparina nell'Angina e nella Trombosi Ventricolare nell'Infarto) Group. *Lancet* **1989,** *2* (8656), 182-6.

85. Narins, C. R.; Hillegass, W. B.; Nelson, C. L.; Tcheng, J. E.; Harrington, R. A.; Phillips, H. R.; Stack, R. S.; Califf, R. M., Relation Between Activated Clotting Time During Angioplasty and Abrupt Closure. *Circulation* **1996,** *93* (4), 667-671.

86. Wright, S. J.; Murray, W. B.; Hampton, W. A.; Hargovan, H., Calculating the protamine-heparin reversal ratio: A pilot study investigating a new method. *Journal of Cardiothoracic and Vascular Anesthesia* **1993,** *7* (4), 416-421.

87. Baird, C. W.; Zurakowski, D.; Robinson, B.; Gandhi, S.; Burdis-Koch, L.; Tamblyn, J.; Munoz, R.; Fortich, K.; Pigula, F. A., Anticoagulation and Pediatric Extracorporeal Membrane Oxygenation: Impact of Activated Clotting Time and Heparin Dose on Survival. *The Annals of thoracic surgery* **2007,** *83* (3), 912-920.

88. Kikura, M.; Lee, M. K.; Levy, J. H., Heparin neutralization with methylene blue, hexadimethrine, or vancomycin after cardiopulmonary bypass. *Anesthesia and analgesia* **1996,** *83* (2), 223-7.

89. Seyfer, A. E.; Seaber, A. V.; Dombrose, F. A.; Urbaniak, J. R., Coagulation changes in elective surgery and trauma. *Annals of Surgery* **1981,** *193* (2), 210-213.

90. Acosta-Avalos, D.; Jedlicka, L. D. L.; Costa, M. S.; Barja, P. R.; da Silva, E. C., Photoacoustic Spectroscopy of Candida albicans Treated with Methylene Blue. *International Journal of Thermophysics* **2012,** *33* (10), 1864-1869.

91. Tang, W.; Xu, H.; Kopelman, R.; Philbert, M. A., Photodynamic Characterization and In Vitro Application of Methylene Blue-containing Nanoparticle Platforms. *Photochemistry and photobiology* **2005,** *81* (2), 242-249.

92. He, X.; Wu, X.; Wang, K.; Shi, B.; Hai, L., Methylene blue-encapsulated phosphonate-terminated silica nanoparticles for simultaneous in vivo imaging and photodynamic therapy. *Biomaterials* **2009,** *30* (29), 5601-5609.

93. Tardivo, J. P.; Del Giglio, A.; de Oliveira, C. S.; Gabrielli, D. S.; Junqueira, H. C.; Tada, D. B.; Severino, D.; de Fátima Turchiello, R.; Baptista, M. S., Methylene blue in photodynamic therapy: From basic mechanisms to clinical applications. *Photodiagnosis and Photodynamic Therapy* **2005,** *2* (3), 175-191.

94. Hariri, A.; Lemaster, J.; Wang, J.; Jeevarathinam, A. S.; Chao, D. L.; Jokerst, J. V., The characterization of an economic and portable LED-based photoacoustic imaging system to facilitate molecular imaging. *Photoacoustics* **2018,** *9*, 10-20.

95. Wang, J.; Lin, C.-Y.; Moore, C.; Jhunjhunwala, A.; Jokerst, J. V., Switchable Photoacoustic Intensity of Methylene Blue via Sodium Dodecyl Sulfate Micellization. *Langmuir* **2018,** *34* (1), 359-365.

96. Clifton, J. I.; Leikin, J. B., Methylene Blue. *American Journal of Therapeutics* **2003,** *10* (4), 289-291.

97. Schirmer, R. H.; Coulibaly, B.; Stich, A.; Scheiwein, M.; Merkle, H.; Eubel, J.; Becker, K.; Becher, H.; Müller, O.; Zich, T.; Schiek, W.; Kouyaté, B., Methylene blue as an antimalarial agent. *Redox Report* **2003,** *8* (5), 272-275.

98. Tan, L.; Yao, S.; Xie, Q., Electrochemical determination of heparin using methylene blue probe and study on competition of Ba2+ with methylene blue for binding heparin. *Talanta* **2007,** *71* (2), 827-832.

99. Němcová, I.; Rychlovský, P.; Havelcová, M.; Brabcová, M., Determination of heparin using flow injection analysis with spectrophotometric detection. *Analytica Chimica Acta* **1999,** *401* (1), 223-228.

100. Wang, J.; Chen, F.; Arconada-Alvarez, S. J.; Hartanto, J.; Yap, L.-P.; Park, R.; Wang, F.; Vorobyova, I.; Dagliyan, G.; Conti, P. S.; Jokerst, J. V., A Nanoscale Tool for Photoacoustic-Based Measurements of Clotting Time and Therapeutic Drug Monitoring of Heparin. *Nano Letters* **2016,** *16* (10), 6265-6271.

101. Jin, L.; Abrahams, J. P.; Skinner, R.; Petitou, M.; Pike, R. N.; Carrell, R. W., The anticoagulant activation of antithrombin by heparin. *Proceedings of the National Academy of Sciences* **1997,** *94* (26), 14683-14688.

102. Jiao, Q.; Liu, Q., Characterization of the interaction between methylene blue and glycosaminoglycans. *Spectrochimica Acta Part A: Molecular and Biomolecular Spectroscopy* **1999,** *55* (7), 1667-1673.

103. Cox, B.; Laufer, J.; Beard, P. In *The challenges for quantitative photoacoustic imaging*, Proc. SPIE, 2009; p 717713.

104. Gupta, S.; Chatni, M. R.; Rao, A. L. N.; Vullev, V. I.; Wang, L. V.; Anvari, B., Virus-mimicking nano-constructs as a contrast agent for near infrared photoacoustic imaging. *Nanoscale* **2013,** *5* (5), 1772-1776.

105. Kim, T.; Lemaster, J. E.; Chen, F.; Li, J.; Jokerst, J. V., Photoacoustic Imaging of Human Mesenchymal Stem Cells Labeled with Prussian Blue–Poly(l-lysine) Nanocomplexes. *ACS nano* **2017,** *11* (9), 9022-9032.

106. Rabinowitch, E.; Epstein, L. F., Polymerization of dyestuffs in solution. thionine and methylene blue1. *Journal of the American Chemical Society* **1941,** *63* (1), 69-78.

107. Liu, Q.; Jiao, Q., Mechanism of methylene blue action and interference in the heparin assay. *Spectroscopy letters* **1998,** *31* (5), 913-924.

108. Braswell, E., Evidence for trimerization in aqueous solutions of methylene blue. *The Journal of Physical Chemistry* **1968,** *72* (7), 2477-2483.

109. Severino, D.; Junqueira, H. C.; Gugliotti, M.; Gabrielli, D. S.; Baptista, M. S., Influence of negatively charged interfaces on the ground and excited state properties of methylene blue. *Photochemistry and photobiology* **2003,** *77* (5), 459-468.

110. Morgounova, E.; Shao, Q.; Hackel, B. J.; Thomas, D. D.; Ashkenazi, S., Photoacoustic lifetime contrast between methylene blue monomers and self-quenched dimers as a model for dual-labeled activatable probes. *Journal of biomedical optics* **2013,** *18* (5), 056004-056004.

111. Casu, B.; Naggi, A.; Torri, G., Re-visiting the structure of heparin. *Carbohydrate Research* **2015,** *403*, 60-68.

112. Sueishi, Y.; Inazumi, N.; Hanaya, T., Effects of pressure on inclusion complexation of methylene blue with water-soluble p-sulfonatocalix [n] arenes. *Journal of physical organic chemistry* **2005,** *18* (5), 448-455.

113. Moreno-Villoslada, I.; Torres, C.; González, F.; Shibue, T.; Nishide, H., Binding of methylene blue to polyelectrolytes containing sulfonate groups. *Macromolecular Chemistry and Physics* **2009,** *210* (13-14), 1167-1175.

114. Micheau, J.; Zakharova, G.; Chibisov, A., Reversible aggregation, precipitation and re-dissolution of rhodamine 6G in aqueous sodium dodecyl sulfate. *Physical Chemistry Chemical Physics* **2004,** *6* (9), 2420-2425.

115. Chen, Y.-S.; Yoon, S. J.; Frey, W.; Dockery, M.; Emelianov, S., Dynamic contrast-enhanced photoacoustic imaging using photothermal stimuli-responsive composite nanomodulators. *Nature communications* **2017,** *8*.

116. McGaughey, G. B.; Gagné, M.; Rappé, A. K., π-Stacking interactions alive and well in proteins. *Journal of Biological Chemistry* **1998,** *273* (25), 15458-15463.

117. Miller III, B. R.; McGee Jr, T. D.; Swails, J. M.; Homeyer, N.; Gohlke, H.; Roitberg, A. E., MMPBSA. py: an efficient program for end-state free energy calculations. *Journal of chemical theory and computation* **2012,** *8* (9), 3314-3321.

118. Pu, K.; Shuhendler, A. J.; Jokerst, J. V.; Mei, J.; Gambhir, S. S.; Bao, Z.; Rao, J., Semiconducting polymer nanoparticles as photoacoustic molecular imaging probes in living mice. *Nature Nanotechnology* **2014,** *9*, 233.

119. Pu, K.; Zhen, X.; Zhang, J.; Huang, J.; Xie, C.; Miao, Q., Macrotheranostic Probe with Disease-activated Near-infrared Fluorescence, Photoacoustic and Photothermal Signals for Imaging-guided Therapy. *Angew Chem Int Ed Engl* **2018**.

120. Qin, X.; Chen, H.; Yang, H.; Wu, H.; Zhao, X.; Wang, H.; Chour, T.; Neofytou, E.; Ding, D.; Daldrup-Link, H.; Heilshorn Sarah, C.; Li, K.; Wu Joseph, C., Photoacoustic Imaging of Embryonic Stem Cell-Derived Cardiomyocytes in Living Hearts with Ultrasensitive Semiconducting Polymer Nanoparticles. *Advanced Functional Materials* **2017,** *28* (1), 1704939.

121. Sun, I.-C.; Emelianov, S. In *Dual-imaging contrast agent for ultrasound and photoacoustic imaging: gas-generating plasmonic-core nanoconstruct (Conference Presentation)*, SPIE BiOS, SPIE: **2018**.

122. Stylogiannis, A.; Prade, L.; Buehler, A.; Aguirre, J.; Sergiadis, G.; Ntziachristos, V., Continuous wave laser diodes enable fast optoacoustic imaging. *Photoacoustics* **2018,** *9*, 31-38.

123. Johannes, R.; Héctor, E.; Sven, G.; Gali, S.; Michael, Z.; Georg, W.; Vasilis, N.; Daniel, R., Dual-wavelength hybrid optoacoustic-ultrasound biomicroscopy for functional imaging of large-scale cerebral vascular networks. *Journal of biophotonics* **2018**, 11(9), p.e201800057.

124. Wong, T. T. W.; Zhang, R.; Zhang, C.; Hsu, H.-C.; Maslov, K. I.; Wang, L.; Shi, J.; Chen, R.; Shung, K. K.; Zhou, Q.; Wang, L. V., Label-free automated three-dimensional imaging of whole organs by microtomy-assisted photoacoustic microscopy. *Nature Communications* **2017,** *8* (1), 1386.

125. Martinez, A. W.; Phillips, S. T.; Whitesides, G. M.; Carrilho, E., Diagnostics for the Developing World: Microfluidic Paper-Based Analytical Devices. *Anal. Chem. (Washington, DC, U. S.)* **2010,** *82* (1), 3-10.

126. Chaiyo, S.; Mehmeti, E.; Siangproh, W.; Hoang, T. L.; Nguyen, H. P.; Chailapakul, O.; Kalcher, K., Non-enzymatic electrochemical detection of glucose with a disposable paper-based sensor using a cobalt phthalocyanine–ionic liquid–graphene composite. *Biosensors and Bioelectronics* **2018,** *102*, 113-120.

127. Chen, F.; Ma, M.; Wang, J.; Wang, F.; Chern, S. X.; Zhao, E. R.; Jhunjhunwala, A.; Darmadi, S.; Chen, H.; Jokerst, J. V., Exosome-like silica nanoparticles: a novel ultrasound contrast agent for stem cell imaging. *Nanoscale* **2017,** *9* (1), 402-411.

128. Zemp, R. J.; Bitton, R.; Shung, K. K.; Li, M.-L.; Stoica, G.; Wang, L. V., Photoacoustic imaging of the microvasculature with a high-frequency ultrasound array transducer. *Journal of biomedical optics* **2007,** *12* (1), 010501.

129. Wang, J.; Jeevarathinam, A. S.; Humphries, K.; Jhunjhunwala, A.; Chen, F.; Hariri, A.; Miller, B. R.; Jokerst, J. V., A Mechanistic Investigation of Methylene Blue and Heparin Interactions and Their Photoacoustic Enhancement. *Bioconjugate Chemistry* **2018**.

130. Tian, J.; Jarujamrus, P.; Li, L.; Li, M.; Shen, W., Strategy To Enhance the Wettability of Bioacive Paper-Based Sensors. *ACS Applied Materials & Interfaces* **2012,** *4* (12), 6573-6578.

131. You, J.-G.; Liu, Y.-W.; Lu, C.-Y.; Tseng, W.-L.; Yu, C.-J., Colorimetric assay of heparin in plasma based on the inhibition of oxidase-like activity of citrate-capped platinum nanoparticles. *Biosensors and Bioelectronics* **2017,** *92*, 442-448.

132. Amemiya, S.; Kim, Y.; Ishimatsu, R.; Kabagambe, B., Electrochemical heparin sensing at liquid/liquid interfaces and polymeric membranes. *Anal. Bioanal. Chem.* **2011,** *399* (2), 571-579.

133. Zhang, H. F.; Maslov, K.; Sivaramakrishnan, M.; Stoica, G.; Wang, L. V., Imaging of hemoglobin oxygen saturation variations in single vessels in vivo using photoacoustic microscopy. *Appl. Phys. Lett.* **2007,** *90* (5), 053901/1-053901/3.

134. Küçükkılınç, T.; Özer, İ., Multi-site inhibition of human plasma cholinesterase by cationic phenoxazine and phenothiazine dyes. *Archives of biochemistry and biophysics* **2007,** *461* (2), 294-298.

135. Strohm, Eric M.; Berndl, E. S. L.; Kolios, Michael C., Probing Red Blood Cell Morphology Using High-Frequency Photoacoustics. *Biophysical Journal* **2013,** *105* (1), 59-67.

136. Gatti, G.; Casu, B.; Hamer, G. K.; Perlin, A. S., Studies on the Conformation of Heparin by 1H and 13C NMR Spectroscopy. *Macromolecules* **1979,** *12* (5), 1001-1007.

137. Muñoz, E. M.; Linhardt, R. J., Heparin-binding domains in vascular biology. *Arteriosclerosis, thrombosis, and vascular biology* **2004,** *24* (9), 1549-1557.

138. Alesci, S.; Borggrefe, M.; Dempfle, C.-E., Effect of freezing method and storage at −20 °C and −70 °C on prothrombin time, aPTT and plasma fibrinogen levels. *Thrombosis Research* **2009,** *124* (1), 121-126.

139. Perry, D. J.; Fitzmaurice, D. A.; Kitchen, S.; Mackie, I. J.; Mallett, S., Point-of-care testing in haemostasis. *British Journal of Haematology* **2010,** *150* (5), 501-514.

140. Baglin, T.; Barrowcliffe, T. W.; Cohen, A.; Greaves, M., Guidelines on the use and monitoring of heparin. *Br. J. Haematol.* **2006,** *133* (1), 19-34.

141. Buee, L.; Boyle, N. J.; Zhang, L.; Delacourte, A.; Fillit, H. M., Optimization of an alcian blue dot-blot assay for the detection of glycosaminoglycans and proteoglycans. *Analytical Biochemistry* **1991,** *195* (2), 238-242.

142. Bromfield, S. M.; Barnard, A.; Posocco, P.; Fermeglia, M.; Pricl, S.; Smith, D. K., Mallard Blue: A High-Affinity Selective Heparin Sensor That Operates in Highly Competitive Media. *J. Am. Chem. Soc.* **2013,** *135* (8), 2911-2914.

143. Templeton, D. M., The basis and applicability of the dimethylmethylene blue binding assay for sulfated glycosaminoglycans. *Connect. Tissue Res.* **1988,** *17* (1), 23-32.

144. Mehta, P. K.; Lee, H.; Lee, K.-H., Highly sensitive ratiometric detection of heparin and its oversulfated chondroitin sulfate contaminant by fluorescent peptidyl probe. *Biosensors and Bioelectronics* **2017,** *91*, 545-552.

145. Lehman, C. M.; Frank, E. L., Laboratory Monitoring of Heparin Therapy: Partial Thromboplastin Time or Anti-Xa Assay? *Laboratory Medicine* **2009,** *40* (1), 47-51.

146. Vera-Aguilera, J.; Yousef, H.; Beltran-Melgarejo, D.; Teng, T. H.; Jan, R.; Mok, M.; Vera-Aguilera, C.; Moreno-Aguilera, E., Clinical Scenarios for Discordant Anti-Xa. *Advances in Hematology* **2016,** *2016*, 4054806.

147. Maxwell, L. G.; Goodwin, S. R.; Mancuso, T. J.; Baum, V. C.; Zuckerberg, A. L.; Morgan, P. G.; Motoyama, E. K.; Davis, P. J.; Sullivan, K. J., CHAPTER 36 - Systemic Disorders. In *Smith's Anesthesia for Infants and Children (Eighth Edition)*, Mosby: Philadelphia, **2011**, 1098-1182.

148. Murray, D. J.; Brosnahan, W. J.; Pennell, B.; Kapalanski, D.; Weiler, J. M.; Olson, J., Heparin detection by the activated coagulation time: A comparison of the sensitivity of coagulation tests and heparin assays. *Journal of Cardiothoracic and Vascular Anesthesia* **1997,** *11* (1), 24-28.

149. Garcia, M. E. D.; Sanz-Medel, A., Dye-surfactant interactions: a review. *Talanta* **1986,** *33* (3), 255-264.

150. Carroll, M. K.; Unger, M. A.; Leach, A. M.; Morris, M. J.; Ingersoll, C. M.; Bright, F. V., Interactions between Methylene Blue and Sodium Dodecyl Sulfate in Aqueous Solution Studied by Molecular Spectroscopy. *Appl. Spectrosc.* **1999,** *53* (7), 780-784.

151. Sarkar, M.; Poddar, S., Studies on the Interaction of Surfactants with Cationic Dye by Absorption Spectroscopy. *Journal of Colloid and Interface Science* **2000,** *221* (2), 181-185.

152. Ruprecht, J.; Baumgaertel, H., The influence of the electronic structure on the dimerization of phenthiazonium cations in aqueous solution. *Berichte der Bunsengesellschaft für physikalische Chemie* **1984,** *88* (2), 145-150.

153. Neumann, M. G.; Gehlen, M. H., The interaction of cationic dyes with anionic surfactants in the premicellar region. *Journal of Colloid and Interface Science* **1990,** *135* (1), 209-217.

154. Dean, J. C.; Oblinsky, D. G.; Rafiq, S.; Scholes, G. D., Methylene Blue Exciton States Steer Nonradiative Relaxation: Ultrafast Spectroscopy of Methylene Blue Dimer. *The Journal of Physical Chemistry B* **2016,** *120* (3), 440-454.

155. Kasha, M.; Rawls, H.; Ashraf El-Bayoumi, M., The exciton model in molecular spectroscopy. *Pure and Applied Chemistry* **1965,** *11* (3-4), 371-392.

156. Kasha, M., Energy Transfer Mechanisms and the Molecular Exciton Model for Molecular Aggregates. *Radiat Res* **1963,** *20*, 55-70.

157. Jockusch, S.; Turro, N. J.; Tomalia, D. A., Aggregation of Methylene Blue Adsorbed on Starburst Dendrimers. *Macromolecules* **1995,** *28* (22), 7416-7418.

158. Moroi, Y.; Motomura, K.; Matuura, R., The critical micelle concentration of sodium dodecyl sulfate-bivalent metal dodecyl sulfate mixtures in aqueous solutions. *Journal of Colloid and Interface Science* **1974,** *46* (1), 111-117.

159. Duplâtre, G.; Ferreira Marques, M. F.; da Graça Miguel, M., Size of Sodium Dodecyl Sulfate Micelles in Aqueous Solutions as Studied by Positron Annihilation Lifetime Spectroscopy. *The Journal of Physical Chemistry* **1996,** *100* (41), 16608-16612.

160. Li, N.; Liu, S.; Luo, H., A new method for the determination of the first and second CMC in CTAB solution by resonance Rayleigh scattering technology. *Analytical letters* **2002,** *35* (7), 1229-1238.

161. Severino, D.; Junqueira, H. C.; Gugliotti, M.; Gabrielli, D. S.; Baptista, M. S., Influence of Negatively Charged Interfaces on the Ground and Excited State Properties of Methylene Blue. *Photochemistry and photobiology* **2003,** *77* (5), 459-468.

162. Jacobs, I. J.; Menon, U.; Ryan, A.; Gentry-Maharaj, A.; Burnell, M.; Kalsi, J. K.; Amso, N. N.; Apostolidou, S.; Benjamin, E.; Cruickshank, D., Ovarian cancer screening and mortality in the UK Collaborative Trial of Ovarian Cancer Screening (UKCTOCS): a randomised controlled trial. *The Lancet* **2016,** *387* (10022), 945-956.

163. Howlader N, N. A., Krapcho M, Miller D, Bishop K, Kosary CL, Yu M, Ruhl J, Tatalovich Z, Mariotto A, Lewis DR, Chen HS, Feuer EJ, Cronin KA (eds), SEER Cancer Statistics Review, 1975-2014. *National Cancer Institute, Bethesda, MD based on November* **2016** *SEER data submission, posted to the SEER web site*.

164. Menon, U.; Gentry-Maharaj, A.; Hallett, R.; Ryan, A.; Burnell, M.; Sharma, A.; Lewis, S.; Davies, S.; Philpott, S.; Lopes, A.; Godfrey, K.; Oram, D.; Herod, J.; Williamson, K.; Seif, M. W.; Scott, I.; Mould, T.; Woolas, R.; Murdoch, J.; Dobbs, S.; Amso, N. N.; Leeson, S.; Cruickshank, D.; McGuire, A.; Campbell, S.; Fallowfield, L.; Singh, N.; Dawnay, A.; Skates, S. J.; Parmar, M.; Jacobs, I., Sensitivity and specificity of multimodal and ultrasound screening for ovarian cancer, and stage distribution of detected cancers: results of the prevalence screen of the UK Collaborative Trial of Ovarian Cancer Screening (UKCTOCS). *The Lancet Oncology* **2009,** *10* (4), 327-340.

165. Li, H.; Kumavor, P.; Alqasemi, U. S.; Zhu, Q. In *Utilizing spatial and spectral features of photoacoustic imaging for ovarian cancer detection and diagnosis*, SPIE: **2015**; p 12.

166. Salehi, H. S.; Li, H.; Merkulov, A.; Kumavor, P. D.; Vavadi, H.; Sanders, M.; Kueck, A.; Brewer, M. A.; Zhu, Q. In *Coregistered photoacoustic and ultrasound imaging and classification of ovarian cancer: ex vivo and in vivo studies*, SPIE: **2016**; p 11.

167. Aguirre, A.; Ardeshirpour, Y.; Sanders, M. M.; Brewer, M.; Zhu, Q., Potential Role of Coregistered Photoacoustic and Ultrasound Imaging in Ovarian Cancer Detection and Characterization. *Translational Oncology* **2011,** *4* (1), 29-37.

168. Salehi, H. S.; Wang, T.; Kumavor, P. D.; Li, H.; Zhu, Q., Design of miniaturized illumination for transvaginal co-registered photoacoustic and ultrasound imaging. *Biomed. Opt. Express* **2014,** *5* (9), 3074-3079.

169. Nandy, S.; Mostafa, A.; Hagemann, I. S.; Powell, M. A.; Amidi, E.; Robinson, K.; Mutch, D. G.; Siegel, C.; Zhu, Q., Evaluation of Ovarian Cancer: Initial Application of Coregistered Photoacoustic Tomography and US. *Radiology* **2018***,* 289(3), 740-747.

170. Monaco, I.; Arena, F.; Biffi, S.; Locatelli, E.; Bortot, B.; La Cava, F.; Marini, G. M.; Severini, G. M.; Terreno, E.; Comes Franchini, M., Synthesis of Lipophilic Core–Shell Fe3O4@SiO2@Au Nanoparticles and Polymeric Entrapment into Nanomicelles: A Novel Nanosystem for in Vivo Active Targeting and Magnetic Resonance–Photoacoustic Dual Imaging. *Bioconjugate chemistry* **2017,** *28* (5), 1382-1390.

171. Jokerst, J. V.; Cole, A. J.; Van de Sompel, D.; Gambhir, S. S., Gold Nanorods for Ovarian Cancer Detection with Photoacoustic Imaging and Resection Guidance via Raman Imaging in Living Mice. *ACS nano* **2012,** *6* (11), 10366-10377.

172. Xi, L.; Satpathy, M.; Zhao, Q.; Qian, W.; Yang, L.; Jiang, H., HER-2/neu targeted delivery of a nanoprobe enables dual photoacoustic and fluorescence tomography of ovarian cancer. *Nanomedicine: Nanotechnology, Biology and Medicine* **2014,** *10* (3), 669-677.

173. Hsu, S.-W.; On, K.; Tao, A. R., Localized Surface Plasmon Resonances of Anisotropic Semiconductor Nanocrystals. *Journal of the American Chemical Society* **2011,** *133* (47), 19072-19075.

174. Hsu, S.-W.; Ngo, C.; Bryks, W.; Tao, A. R., Shape Focusing During the Anisotropic Growth of CuS Triangular Nanoprisms. *Chemistry of Materials* **2015,** *27* (14), 4957-4963.

175. Hsu, S.-W.; Ngo, C.; Tao, A. R., Tunable and Directional Plasmonic Coupling within Semiconductor Nanodisk Assemblies. *Nano Letters* **2014,** *14* (5), 2372-2380.

176. Kobat, D.; Durst, M. E.; Nishimura, N.; Wong, A. W.; Schaffer, C. B.; Xu, C., Deep tissue multiphoton microscopy using longer wavelength excitation. *Opt. Express* **2009,** *17* (16), 13354-13364.

177. Ku, G.; Zhou, M.; Song, S.; Huang, Q.; Hazle, J.; Li, C., Copper Sulfide Nanoparticles As a New Class of Photoacoustic Contrast Agent for Deep Tissue Imaging at 1064 nm. *ACS nano* **2012,** *6* (8), 7489-7496.

178. Smith, B. R.; Kempen, P.; Bouley, D.; Xu, A.; Liu, Z.; Melosh, N.; Dai, H.; Sinclair, R.; Gambhir, S. S., Shape matters: intravital microscopy reveals surprising geometrical dependence for nanoparticles in tumor models of extravasation. *Nano letters* **2012,** *12* (7), 3369-3377.

179. Chauhan, V. P.; Popović, Z.; Chen, O.; Cui, J.; Fukumura, D.; Bawendi, M. G.; Jain, R. K., Fluorescent nanorods and nanospheres for real-time in vivo probing of nanoparticle shape-dependent tumor penetration. *Angewandte Chemie International Edition* **2011,** *50* (48), 11417-11420.

180. Adriani, G.; de Tullio, M. D.; Ferrari, M.; Hussain, F.; Pascazio, G.; Liu, X.; Decuzzi, P., The preferential targeting of the diseased microvasculature by disk-like particles. *Biomaterials* **2012,** *33* (22), 5504-5513.

181. Toy, R.; Peiris, P. M.; Ghaghada, K. B.; Karathanasis, E., Shaping cancer nanomedicine: the effect of particle shape on the in vivo journey of nanoparticles. *Nanomedicine* **2014,** *9* (1), 121-134.

182. Orendorff, C. J.; Murphy, C. J., Quantitation of Metal Content in the Silver-Assisted Growth of Gold Nanorods. *The Journal of Physical Chemistry B* **2006,** *110* (9), 3990-3994.

183. Link, S.; Burda, C.; Nikoobakht, B.; El-Sayed, M. A., Laser-Induced Shape Changes of Colloidal Gold Nanorods Using Femtosecond and Nanosecond Laser Pulses. *The Journal of Physical Chemistry B* **2000,** *104* (26), 6152-6163.

184. Rahavendran, S. V.; Vekich, S.; Skor, H.; Batugo, M.; Nguyen, L.; Shetty, B.; Shen, Z., Discovery pharmacokinetic studies in mice using serial microsampling, dried blood spots and microbore LC–MS/MS. *Bioanalysis* **2012,** *4* (9), 1077-1095.

185. Feng, W.; Nie, W.; Cheng, Y.; Zhou, X.; Chen, L.; Qiu, K.; Chen, Z.; Zhu, M.; He, C., In vitro and in vivo toxicity studies of copper sulfide nanoplates for potential photothermal applications. *Nanomedicine: Nanotechnology, Biology and Medicine* **2015,** *11* (4), 901-912.

186. Guo, L.; Panderi, I.; Yan, D. D.; Szulak, K.; Li, Y.; Chen, Y.-T.; Ma, H.; Niesen, D. B.; Seeram, N.; Ahmed, A.; Yan, B.; Pantazatos, D.; Lu, W., A Comparative Study of Hollow Copper Sulfide Nanoparticles and Hollow Gold Nanospheres on Degradability and Toxicity. *ACS nano* **2013,** *7* (10), 8780-8793.

187. Wilson, R. H.; Nadeau, K. P.; Jaworski, F. B.; Tromberg, B. J.; Durkin, A. J., *Review of short-wave infrared spectroscopy and imaging methods for biological tissue characterization*, SPIE: **2015**, 20(3), p.030901.

188. Rajian, J. R.; Carson, P. L.; Wang, X., Quantitative photoacoustic measurement of tissue optical absorption spectrum aided by an optical contrast agent. *Opt. Express* **2009,** *17* (6), 4879-4889.

189. Jokerst, J. V.; Thangaraj, M.; Kempen, P. J.; Sinclair, R.; Gambhir, S. S., Photoacoustic Imaging of Mesenchymal Stem Cells in Living Mice via Silica-Coated Gold Nanorods. *ACS Nano* **2012,** *6* (7), 5920-5930.

190. Stöber, W.; Fink, A.; Bohn, E., Controlled growth of monodisperse silica spheres in the micron size range. *Journal of Colloid and Interface Science* **1968,** *26* (1), 62-69.

191. Abràmoff, M. D.; Magalhães, P. J.; Ram, S. J., Image processing with ImageJ. *Biophotonics international* **2004,** *11* (7), 36-42.

192. Shriver, Z.; Capila, I.; Venkataraman, G.; Sasisekharan, R., Heparin and Heparan Sulfate: Analyzing Structure and Microheterogeneity. *Handbook of experimental pharmacology* **2012,** (207), 159-176.

193. Woods, R., glycam Web. *Complex Carbohydrate Research Center. Athens, GA: University of Georgia* **2005**.

194. M. J. Frisch, G. W. T., H. B. Schlegel, G. E. Scuseria, M. A. Robb, J. R. Cheeseman, G. Scalmani, V. Barone, G. A. Petersson, H. Nakatsuji, X. Li, M. Caricato, A. V. Marenich, J. Bloino, B. G. Janesko, R. Gomperts, B. Mennucci, H. P. Hratchian, J. V. Ortiz, A. F. Izmaylov, J. L. Sonnenberg, D. Williams-Young, F. Ding, F. Lipparini, F. Egidi, J. Goings, B. Peng, A. Petrone, T. Henderson, D. Ranasinghe, V. G. Zakrzewski, J. Gao, N. Rega, G. Zheng, W. Liang, M. Hada, M. Ehara, K. Toyota, R. Fukuda, J. Hasegawa, M. Ishida, T. Nakajima, Y. Honda, O. Kitao, H. Nakai, T. Vreven, K. Throssell, J. A. Montgomery, Jr., J. E. Peralta, F. Ogliaro, M. J. Bearpark, J. J. Heyd, E. N. Brothers, K. N. Kudin, V. N. Staroverov, T. A. Keith, R. Kobayashi, J. Normand, K. Raghavachari, A. P. Rendell, J. C. Burant, S. S. Iyengar, J. Tomasi, M. Cossi, J. M. Millam, M. Klene, C. Adamo, R. Cammi, J. W. Ochterski, R. L. Martin, K. Morokuma, O. Farkas, J. B. Foresman, and D. J. Fox, Gaussian 16, Revision B.01. **2016**.

195. Polik, W. F. a. S., J. R. , WebMO Enterprise 14.0.006e. *WebMO LLC: Holland, MI,* **2011**.

196. Humphrey, W.; Dalke, A.; Schulten, K., VMD: visual molecular dynamics. *Journal of molecular graphics* **1996,** *14* (1), 33-38.

197. Trott, O.; Olson, A. J., AutoDock Vina: improving the speed and accuracy of docking with a new scoring function, efficient optimization, and multithreading. *Journal of computational chemistry* **2010,** *31* (2), 455-461.

198. D.A. Case, D. S. C., T.E. Cheatham, III, T.A. Darden, R.E. Duke, T.J. Giese, H. Gohlke, A.W. Goetz, D. Greene, N. Homeyer, S. Izadi, A. Kovalenko, T.S. Lee, S. LeGrand, P. Li, C. Lin, J. Liu, T. Luchko, R. Luo, D. Mermelstein, K.M. Merz, G. Monard, H. Nguyen, I. Omelyan, A. Onufriev, F. Pan, R. Qi, D.R. Roe, A. Roitberg, C. Sagui, C.L. Simmerling, W.M. Botello-Smith, J. Swails, R.C. Walker, J. Wang, R.M. Wolf, X. Wu, L. Xiao, D.M. York and P.A. Kollman, AMBER 2017. *University of California, San Francisco* **2017**.

199. Maier, J. A.; Martinez, C.; Kasavajhala, K.; Wickstrom, L.; Hauser, K. E.; Simmerling, C., ff14SB: Improving the Accuracy of Protein Side Chain and Backbone Parameters from ff99SB. *Journal of Chemical Theory and Computation* **2015,** *11* (8), 3696-3713.

200. Wang, J.; Wolf, R. M.; Caldwell, J. W.; Kollman, P. A.; Case, D. A., Development and testing of a general amber force field. *Journal of computational chemistry* **2004,** *25* (9), 1157-1174.

201. Roe, D. R.; Cheatham III, T. E., PTRAJ and CPPTRAJ: software for processing and analysis of molecular dynamics trajectory data. *Journal of chemical theory and computation* **2013,** *9* (7), 3084-3095.

202. Schneider, C. A.; Rasband, W. S.; Eliceiri, K. W., NIH Image to ImageJ: 25 years of Image Analysis. *Nature methods* **2012,** *9* (7), 671-675.

203. Vonk, L. A.; Saris, D. B. F.; van, D. S. F. J.; Liv, N.; Klumperman, J.; Coffer, P. J.; Lorenowicz, M. J.; van, D. S. F. J.; Coffer, P. J.; Lorenowicz, M. J.; Saris, D. B. F.; Saris, D. B. F., Mesenchymal Stromal/stem Cell-derived Extracellular Vesicles Promote Human Cartilage Regeneration In Vitro. *Theranostics* **2018,** *8* (4), 906-920.

204. Xu, H.; Liu, S.-p.; Luo, H.-q., Determination of heparin by resonance Rayleigh scattering method with Nile blue sulfate. *Fenxi Shiyanshi* **2007,** *26* (9), 66-69.

205. Lopez-Marzo, A. M.; Merkoci, A., Paper-based sensors and assays: A success of the engineering design and the convergence of knowledge areas. *Lab Chip* **2016,** *16* (17), 3150-3176.

206. Holme, K. R.; Perlin, A. S., Chitosan N-sulfate. A water-soluble polyelectrolyte. *Carbohydrate Research* **1997,** *302* (1), 7-12.

207. Arconada-Alvarez, S. J.; Lemaster, J. E.; Wang, J.; Jokerst, J. V., The development and characterization of a novel yet simple 3D printed tool to facilitate phantom imaging of photoacoustic contrast agents. *Photoacoustics* **2017,** *5*, 17-24.